Nonlinear Transport and Disorder Effects in Nodal Line Semimetals

Inaugural-Dissertation

zur

Erlangung des Doktorgrades

der Mathematisch-Naturwissenschaftlichen Fakultät

der Universität zu Köln

vorgelegt von

Thomas Bömerich

aus

Frechen

Köln, angenommen im Jahr 2025

Abstract

Symmetries manifest themselves everywhere in nature with invariance under symmetry transformations influencing the properties of many systems. They are also directly connected to conservation laws which often are cornerstones of physical theories. In solids, the Bloch theorem takes advantage of crystalline translation symmetry, giving rise to the band structure of electrons. Of particular interest are so-called "Dirac materials", for which in the last years a whole zoo of examples have been found and researched. Such systems have low-energy excitations that behave like massless, relativistic particles described by a Dirac equation. These materials therefore connect symmetries, topology, and linear electron dispersions.

In this thesis we will mainly work on one example of such materials where the band structure has a nodal line consisting of linear crossings along a ring in momentum space. The main goal will be to investigate different transport properties beyond the linear response to the external fields. Here, symmetries will play a major role as certain responses can only be finite if particular symmetries are absent.

At the start of this thesis we review some of the above mentioned Dirac systems with a focus on the role of symmetries. Afterwards we develop the tools to calculate transport properties of solids both semi-classically as well as from a fully quantum mechanical approach. In both cases, disorder will play an important role.

The main results of this thesis will be on models describing 3d crystals of zirconium pentatelluride ($ZrTe_5$). We will discuss four different transport phenomena in this material: Firstly, we will show how a nonreciprocal response can be created due to the spin texture of the Fermi surface. In this case the resistance will depend on the direction of the applied current which is only possible if inversion symmetry is broken. Secondly, we discuss the current-voltage relation at large magnetic fields which will deviate strongly from the linear Ohm's law. We will see that such an enhancement of nonohmic effects can be achieved in a nodal line system when all electrons sit in the same quasi-1d band. For both of these phenomena it will be necessary to consider inhomogeneous electron distributions due to charged impurities. Next, we consider unconventional Hall effects where the applied current and magnetic field are parallel to each other. Here, broken symmetries will result in a tilted Fermi surface enabling the parallel-field Hall response. Lastly, we will investigate nonlocal transport beyond the effects caused by contact geometries. As a possible mechanism we explore the coupling of charge to additional degrees of freedom.

Contents

Introduction

Solid state materials are full of fascinating physical phenomena both experimentally and theoretically. From crystal growth, measurements and understanding of the underlying mechanisms, condensed matter research has touching points with many other fields of science such as chemistry, engineering, and mathematics. A three-dimensional solid, like a piece of copper, contains about 10^{23} electrons which are all quantum particles interacting with each other (and the ions which form the lattice structure). In its full complexity this problem is impossible to solve even numerically. However, physicists have put great effort into developing approximations and effective models which nicely describe the physics of solid-state systems in specific limits. One central result is the Bloch theorem which states that the wavefunctions in a periodic lattice are given by plane waves multiplied with a space-dependent, periodic function [1]. This result enables us to describe electrons in a periodic lattice by their band structure which has proven highly successful in describing the properties of a solid.

In most conventional metals the electrons can be described by a quadratic dispersion of energy as a function of crystal momentum. In these systems relativistic effects like spin-orbit coupling are usually quite small and the non-relativistic Schrödinger equation provides a sufficient description. Since about 20 years, the band structure of graphene has attracted a huge amount of attention [2]. For these two-dimensional sheets of carbon atoms, two bands touch at isolated points in momentum space. The dispersion close to these band touchings is linear. Therefore, the particles behave like massless Dirac fermions with a band velocity about two orders of magnitude smaller than the speed of light. Subsequently, many more materials with such relativistic low-energy excitations have been found, leading to a whole class of materials known as “Dirac materials”. Symmetries play an important role in these systems as they protect the band crossings from being gapped out. If the chemical potential is located right at the energy of the band crossing, the system is in a semi-metallic state. Such a phase can be distinguished from a regular metal by the temperature dependence of the resistivity due to the different dimensions of the Fermi surface. Because of the Berry phase around the linear band crossings, topology plays an important role in Dirac systems. A prominent consequence is the chiral anomaly in Weyl semimetals which is related to negative magnetoresistance [3].

There are many more such exotic transport phenomena in systems with Dirac-like dispersions. Going beyond linear response to the external fields opens up many more possible transport effects. The existence of such nonlinear responses can lead to deep insights into the symmetries and underlying quantum nature of a system. In this thesis, we will focus on so-called nodal line semimetals where multiple band crossings form a

closed curve in momentum space [4]. Motivated by the material $ZrTe_5$ many parts of this thesis are closely connected to experimental work. This nicely provides a direct application for the theoretical tools which we will develop. On the other hand, correctly describing an experiment can substantially increase the complexity of the required theory. In our work, disorder will play a major part in explaining the size of different nonlinear transport properties.

The first chapter of this thesis will give a more detailed introduction into the different types of Dirac materials with a focus on three-dimensional systems. Here, the role of symmetries and the consequences of symmetry-breaking will be discussed. Afterwards, we develop the theoretical machinery to compute transport properties with a large focus on the semi-classical Boltzmann equation. In chapter 3 we will present the material $ZrTe_5$ in more detail and set up a low-energy Hamiltonian from a symmetry analysis. Using quantum oscillations, we extract the parameters of our model in the experimental regime. The main results will be discussed in chapters 4, 5, 6 and 7. These four projects all deal with different transport effects going beyond the conventional Ohm's law. In each of these chapters we will introduce some further techniques used to understand the specific project. At the end, we will summarize our findings and give an outlook on future research directions.

1 Band crossings in quantum materials

1.1 The Dirac equation

In an attempt to combine special relativity and quantum mechanics, Paul Dirac derived an equation that describes spin-$\frac{1}{2}$ particles and predicted the existence of anti-matter [5, 6]. To obtain an equation which is linear in the time derivative, just like the Schrödinger equation for non-relativistic particles, it is necessary to consider a 4×4 matrix equation. In $(3+1)$ space-time dimensions this equation takes the form

$$(i\hbar\gamma^\mu\partial_\mu - m\mathbb{1}_4)\,\boldsymbol{\psi} = 0, \tag{1.1}$$

where the summation goes over $\mu = 0, 1, 2, 3$ and $\partial_\mu = (\frac{1}{c}\partial_t, \partial_x, \partial_y, \partial_z)$ is the 4-gradient. The gamma matrices γ^μ are 4×4 matrices that obey the anti-commutation relations $\{\gamma^\mu, \gamma^\nu\} = 2\eta^{\mu\nu}\mathbb{1}_4$ with the Minkowski metric $\eta^{\mu\nu}$. A simple choice of gamma matrices can be written in terms of the Pauli matrices σ_i:

$$\gamma_0 = \begin{pmatrix} \mathbb{1}_2 & 0 \\ 0 & -\mathbb{1}_2 \end{pmatrix}, \qquad \gamma_i = \begin{pmatrix} 0 & \sigma_i \\ -\sigma_i & 0 \end{pmatrix}, \tag{1.2}$$

with

$$\sigma_x = \begin{pmatrix} 0 & 1 \\ 1 & 0 \end{pmatrix}, \qquad \sigma_y = \begin{pmatrix} 0 & -i \\ i & 0 \end{pmatrix}, \qquad \sigma_z = \begin{pmatrix} 1 & 0 \\ 0 & -1 \end{pmatrix}. \tag{1.3}$$

As the Dirac equation (1.1) only contains products of covariant and contravariant objects it is Lorentz invariant and thus compatible with special relativity. Because we are dealing with a matrix equation, the wavefunction $\boldsymbol{\psi}$ is a 4-component spinor which will acquire a phase of -1 after a rotation by 360° as is expected for spin-$\frac{1}{2}$ particles such as the electron.

Let us now consider solutions for free particles moving along the z-direction with momentum p_z. The energy eigenvalues are given by $\epsilon = \pm\sqrt{\hbar^2 p_z^2 + m^2c^4}$ which is the relativistic energy-momentum relation. There will be four eigenstates of which two will have positive energy and describe the particles, e.g. electrons, while the other two have negative energy and describe anti-matter. In the case of an electron we would have the positron as its anti-particle. For each type of particle we have a spin-up and a spin-down state. In the case of massless particles we see that the dispersion is linear in the momentum $\epsilon \sim \hbar p_z$ and the spectrum is gapless. We will see that this scenario can be realized in condensed matter systems if symmetries force the effective mass to be zero.

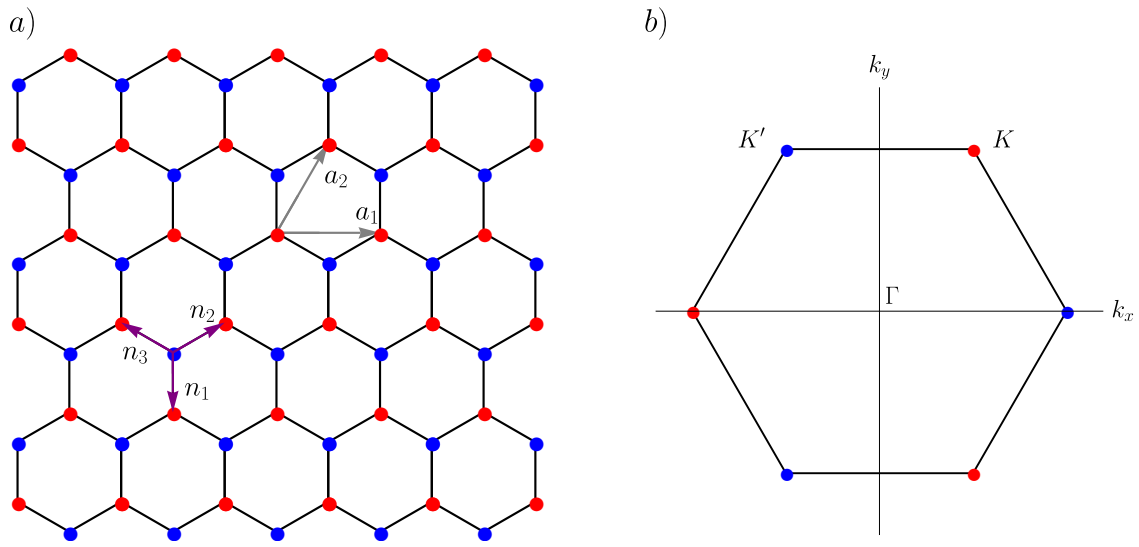

Figure 1.1: a) Lattice structure of graphene. The two sublattices are marked in red and blue. The lattice vectors of the A sublattice are a_1, a_2. Each site has three nearest-neighbors indicated by the vectors n_i. b) First Brillouin zone of the honeycomb lattice. The two bands of the graphene dispersion cross at the corners of the BZ indicated by K, K'.

1.2 Graphene

The most prominent condensed matter system that hosts particles which are described by the Dirac equation would be graphene [2, 7]. It consists of a single two-dimensional layer of carbon atoms which form a hexagonal lattice. In the theory of Bravais lattices graphene is a triangular lattice with two atoms in the unit cell as can be seen in Fig. 1.1. Thus, we are dealing with two sublattices which will be labeled A and B in the following. Many other 2d materials with the same lattice structure like silicene or germanene share a similar dispersion [8, 9]. The difference between these materials is the size of spin-orbit coupling which ,in general, is larger for heavier elements. These additional interactions can lead to the opening of gaps in the band structure.

1.2.1 Tight-binding model

To describe the band structure of graphene we set up a tight-binding model for the free electrons sitting in half-filled p_z-orbitals [7]. The overlap of these orbitals is maximal for the nearest neighbors and rotation symmetric. Thus, we start from a hopping Hamiltonian where particles can jump to one of the three neighboring sites with the same hopping amplitude t for all directions:

$$H_{tb} = t \sum_m \sum_{i=1,2,3} \left(c_B^\dagger(\boldsymbol{R}_m + \boldsymbol{n}_i) c_A(\boldsymbol{R}_m) + c_A^\dagger(\boldsymbol{R}_m) c_B(\boldsymbol{R}_m + \boldsymbol{n}_i) \right). \tag{1.4}$$

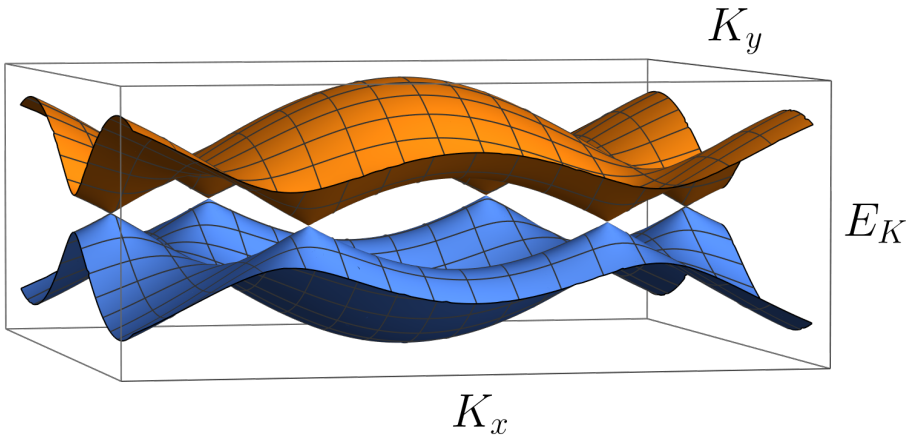

Figure 1.2: Band structure of the tight-binding model for graphene as a function of momentum. The two bands touch at the corners of the Brillouin zone. Near these points, the excitations behave like massless Dirac fermions.

Here, $c^\dagger_{A/B}$ and $c_{A/B}$ are the creation and annihilation operators for sublattice A, B. The lattice sites of sublattice A are given by $\boldsymbol{R}_m = m_1\boldsymbol{a}_1 + m_2\boldsymbol{a}_2$ with $m_1, m_2 \in \mathbb{Z}$ and the lattice vectors $\boldsymbol{a}_1 = a(1,0)$ and $\boldsymbol{a}_2 = \frac{a}{2}(1,\sqrt{3})$ (see Fig. 1.1). Each site on lattice A has three neighbors located at $\boldsymbol{n}_1 = a(0,-\frac{1}{\sqrt{3}}), \boldsymbol{n}_2 = a(-\frac{1}{2},\frac{1}{2\sqrt{3}}), \boldsymbol{n}_3 = a(\frac{1}{2},\frac{1}{2\sqrt{3}})$ relative to its position. To solve this Hamiltonian, we perform a Fourier transformation and work in momentum space. Here, the sum over all lattice sites becomes a sum over all momenta in the first Brillouin zone (BZ) which for the honeycomb lattice is a hexagon as shown in Fig. 1.1 b). The operators for the sublattices at each momentum will now be called $a_{\boldsymbol{k}}$ and $b_{\boldsymbol{k}}$. We can write the Hamiltonian in matrix form and obtain

$$H_{tb} = t \sum_{\boldsymbol{k}\in \mathrm{BZ}} \begin{pmatrix} a^\dagger_{\boldsymbol{k}} & b^\dagger_{\boldsymbol{k}} \end{pmatrix} \begin{pmatrix} 0 & \sum\limits_{i=1,2,3} e^{-i\boldsymbol{n}_i\boldsymbol{k}} \\ \sum\limits_{i=1,2,3} e^{i\boldsymbol{n}_i\boldsymbol{k}} & 0 \end{pmatrix} \begin{pmatrix} a_{\boldsymbol{k}} \\ b_{\boldsymbol{k}} \end{pmatrix}. \tag{1.5}$$

The eigenvalues of this Hamiltonian are then given by $\epsilon_{\boldsymbol{k}} = \pm|d_{\boldsymbol{k}}|$ with $d_{\boldsymbol{k}} = \sum\limits_{i=1,2,3} e^{i\boldsymbol{n}_i\boldsymbol{k}}$. As we deal with a lattice containing two atoms per unit cell we obtain two bands. There are two electrons per unit cell and therefore all negative energy states are filled while the states with positive energy are empty. Thus, the chemical potential sits at $\mu = 0$. At the K and K' points we have $\epsilon_{\boldsymbol{k}} = 0$ and both bands touch, see Fig. 1.2. Even though there are six edges of the BZ, only two band touching points are unique as we can go from one corner of the BZ to another via a reciprocal lattice vector. To get further insight into the low-energy physics of our model we choose one of these crossing points, e.g. $\boldsymbol{k}_0 = (\frac{4\pi}{3a}, 0)$, and perform a Taylor expansion for small momenta around this point with $\boldsymbol{k} = \boldsymbol{k}_0 + \boldsymbol{q}$. Introducing the valley degree of freedom $\tau = \pm 1$ which differentiates between the K and K' points the resulting Hamiltonian takes the form

$$H_{\boldsymbol{k}_0+\boldsymbol{q}} \approx \hbar v \sum_{\boldsymbol{q}} \begin{pmatrix} a^\dagger_{\boldsymbol{q},\tau\boldsymbol{K}} & b^\dagger_{\boldsymbol{q},\tau\boldsymbol{K}} \end{pmatrix} \begin{pmatrix} 0 & q_x - i\tau q_y \\ q_x + i\tau q_y & 0 \end{pmatrix} \begin{pmatrix} a_{\boldsymbol{q},\tau\boldsymbol{K}} \\ b_{\boldsymbol{q},\tau\boldsymbol{K}} \end{pmatrix}, \tag{1.6}$$

with the effective velocity of electrons being $v = \frac{\sqrt{3}at}{2\hbar} \approx 10^6$ m/s. Diagonalizing this Hamiltonian gives us a linear dispersion $\epsilon_{\boldsymbol{q}} = \pm\hbar v\sqrt{q_x^2 + q_y^2}$ similar to that of massless Dirac fermions. It is important to note that the two Dirac points are connected at higher energies via the dispersion as can be seen in Fig. 1.2. Thus, describing graphene as two copies of the 2d Dirac equation is only valid for small energy excitations. A natural cutoff is set by the lattice constant a where small momenta obey $|\boldsymbol{q}| \ll 1/a$. We can write down the full low-energy Hamiltonian as

$$H_{\text{Dirac}} = \hbar v \sum_{\boldsymbol{q}} \begin{pmatrix} c^\dagger_{\boldsymbol{q},\boldsymbol{K}} & c^\dagger_{\boldsymbol{q},\boldsymbol{K}'} \end{pmatrix} \begin{pmatrix} \boldsymbol{\sigma}\cdot\boldsymbol{q} & 0 \\ 0 & (\boldsymbol{\sigma}\cdot\boldsymbol{q})^* \end{pmatrix} \begin{pmatrix} c_{\boldsymbol{q},\boldsymbol{K}} \\ c_{\boldsymbol{q},\boldsymbol{K}'} \end{pmatrix}, \tag{1.7}$$

where $c_{\boldsymbol{q},\boldsymbol{K}} = (a_{\boldsymbol{q},\boldsymbol{K}} \quad b_{\boldsymbol{q},\boldsymbol{K}})$ is the spinor containing creation operators for both sublattices near the K point. σ_i are Pauli matrices which refer to the pseudo-spin emerging in this expansion. We want to emphasize that this is not the physical spin of the electrons as we started from a spin-less model. Taking the electron spin into account would add an additional two-fold degeneracy. As we are dealing with the 2d version of the Dirac equation only two Pauli matrices are present in the Hamiltonian. In the next section we will see how σ_z will change the spectrum and properties of our model.

1.2.2 Breaking symmetries and opening a gap

There are two important symmetries which guarantee that we have gapless Dirac fermions at the corners of the BZ. These are inversion symmetry $\mathcal{I}$ and time-reversal $\mathcal{T}$.

Under inversion symmetry one sublattice gets mapped onto the other and same for the two valleys as we have $\boldsymbol{k} \to -\boldsymbol{k}$. We can write this transformation as a symmetry operator $\mathcal{I} = \tau_x \otimes \sigma_x$. As the labeling of sublattices was only an arbitrary choice made by us and inversion of the graphene lattice just maps carbon atoms onto each other we expect the Hamiltonian to also have inversion symmetry. Indeed, one can check that $\mathcal{I}H_{\text{Dirac}}(-\boldsymbol{q})\mathcal{I}^{-1} = H_{\text{Dirac}}(\boldsymbol{q})$ and thus the symmetry is obeyed.

In the case of time-reversal we have to include complex conjugation K_c to the symmetry operator which also maps $\boldsymbol{k} \to -\boldsymbol{k}$. The pseudo-spin remains unaffected and we can write $\mathcal{T} = (\tau_x \otimes \mathbb{1})\, K_c$. Again, we find that this is a symmetry of the Hamiltonian $\mathcal{T}H_{\text{Dirac}}(-\boldsymbol{q})\mathcal{T}^{-1} = H_{\text{Dirac}}(\boldsymbol{q})$.

To close this section on graphene and 2d Dirac fermions we want to see what happens when we break one of these symmetries. While adding additional terms proportional to σ_x or σ_y only shift the position of the Dirac points inside the BZ, the term $\mathbb{1} \otimes \sigma_z$ opens up a gap around $\epsilon = 0$ and thus splits the Dirac cones. This term can be interpreted as a

staggered potential on the two sublattices and therefore breaking the inversion symmetry. One can also write down a term that treats the two valleys as well as the sublattices differently and open a gap that way. This term $\tau_z \otimes \sigma_z$ breaks time-reversal symmetry while preserving inversion symmetry.
In conclusion, it is necessary that we break at least one of the above mentioned symmetries if we want to induce a mass gap to spinless Dirac fermions. In the following section we will look at 3d band structures and which band crossings are allowed under certain symmetries.

1.3 Dirac & Weyl semimetals in 3d

This section is based on the review article "Weyl and Dirac semimetals in three-dimensional solids" Rev. Mod. Phys. 90, 15001 (2018) [10].
In the previous section we have seen that in 2d systems certain symmetries are required for the formation of Dirac points. It turns out that in higher spatial dimensions, where there are more tuning parameters a.k.a. momenta, it is much easier to achieve band crossings without symmetries. A general two band Hamiltonian can be written as [11, 12]

$$H = \begin{pmatrix} h_3(\boldsymbol{k}) & h_1(\boldsymbol{k}) - ih_2(\boldsymbol{k}) \\ h_1(\boldsymbol{k}) + ih_2(\boldsymbol{k}) & -h_3(\boldsymbol{k}) \end{pmatrix} = h_1(\boldsymbol{k})\sigma_x + h_2(\boldsymbol{k})\sigma_y + h_3(\boldsymbol{k})\sigma_z, \tag{1.8}$$

with general functions $h_i(\boldsymbol{k}) \in \mathbb{R}$. The corresponding energy eigenvalues will be given by $\epsilon(\boldsymbol{k}) = \pm\sqrt{h_1^2(\boldsymbol{k}) + h_2^2(\boldsymbol{k}) + h_3^2(\boldsymbol{k})}$. To achieve a band crossing all three terms must be zero simultaneously, thus obeying $h_1 = h_2 = h_3 = 0$. These conditions can be fulfilled when there are at least three tuning parameters which would be the case in three or higher dimensions. In 2d on the other hand, we just have two momenta and require additional symmetries to realize a band crossing. For example, time-reversal symmetry requires the σ_y term to be excluded from the Hamiltonian which leaves us with only two terms that need to be set to zero.

1.3.1 Weyl semimetals

If there exists such a crossing point at momentum $\boldsymbol{k}_0$ we can perform an expansion of the Hamiltonian around that point and obtain

$$H \approx \hbar \sum_{i=1,2,3} v_i k_i \sigma_i, \tag{1.9}$$

where $\boldsymbol{k}$ is the momentum relative to the location of the band crossing, which is called a Weyl point. For an isotropic system we can set $v_i = v$ and the Fermi surface close to the crossing point will become a sphere with $\epsilon_F^2 = \hbar^2 v^2 (k_x^2 + k_y^2 + k_z^2)$. For such a Fermi surface we can calculate a topological invariant, the Chern number, by integrating the

Berry curvature $\boldsymbol{\Omega}$

$$C = \frac{1}{2\pi} \int_{\mathcal{FS}} \boldsymbol{\Omega} \, \mathrm{d}\boldsymbol{S}, \tag{1.10}$$

with $\boldsymbol{\Omega}(\boldsymbol{k}) = \boldsymbol{\nabla}_{\boldsymbol{k}} \times \boldsymbol{A}(\boldsymbol{k})$ and the Berry connection $\boldsymbol{A}(\boldsymbol{k}) = -i \langle u_{\boldsymbol{k}} | \boldsymbol{\nabla}_{\boldsymbol{k}} | u_{\boldsymbol{k}} \rangle$. The Berry curvature is gauge-invariant and describes the local geometric properties of the wavefunction. On the other hand, the Berry connection is a gauge-dependent quantity that measures the local phase change of the wavefunction when the momentum is changed infinitesimally. The integral of the Berry connection over a closed curve will be gauge-independent and thus can be related to physical observables. It is called the Berry phase. The eigenstates of the isotropic Weyl Hamiltonian are given by [13]

$$|u_-\rangle = \begin{pmatrix} \sin(\theta/2)\ \mathrm{e}^{i\varphi} \\ -\cos(\theta/2) \end{pmatrix} \quad |u_+\rangle = \begin{pmatrix} \cos(\theta/2)\ \mathrm{e}^{-i\varphi} \\ \sin(\theta/2) \end{pmatrix}, \tag{1.11}$$

where we have switched to polar coordinates (due to the rotational symmetry of the problem) with polar angle φ and azimuthal angle θ. As the normal vector of the Fermi surface points radially outward we just need the radial component of the Berry curvature $\Omega_r = \frac{1}{r\ \sin(\theta)} \left(\partial_\theta (A_\varphi \sin\theta) - \partial A_\theta\right) = \frac{1}{2r^2}$ with $r = \sqrt{k_x^2 + k_y^2 + k_z^2}$. If we compute the total Chern number for the state $|u_+\rangle$, which corresponds to a positive energy $\epsilon_F > 0$, the integration gives us $C = +1$ [13]. Thus, there is a quantized Berry flux through the Fermi surface. The source of this flux is the Weyl point. In the next chapter, we will see how this flux can be interpreted as a magnetic field and which consequences it has on transport. If we instead have $\epsilon_F < 0$ we need to use the state $|u_-\rangle$ which has Chern number $C = -1$. As the Brillouin zone is periodic in all three space-directions it is required that there always exists an even number of band crossings. With just a single crossing point the bands can not be periodic and therefore, each Weyl point must have one partner. This result is known as the Nielsen-Ninomiya theorem or "fermion doubling theorem" [14, 15]. The second Weyl point must have opposite chirality, meaning we have the opposite sign in the Hamiltonian $H = -\hbar v \boldsymbol{k} \cdot \boldsymbol{\sigma}$ as compared to Eq. (1.9). As this Weyl point will also have opposite Chern number it acts as a drain of the Berry flux instead of a source. If we extend the integration surface in Eq. (1.10) to be the whole BZ it is equivalent to a single point due to periodicity. In this case, the total Chern number has to be zero. This is fulfilled as the integration surface encloses both a source and sink of the Berry curvature and there will be no net flux. One consequence of the topological nature of the Weyl points is that they can not be gapped by a small perturbation but instead, they will just be shifted in k-space. The only way to annihilate them is if two Weyl points of opposite chirality meet at the same momentum. Otherwise if a single Weyl point would remain we would have a net Berry charge in the system. So far we have not invoked any symmetries and have shown that in 3d we can still construct linear band crossings of two

Time-reversal symmetry	Inversion symmetry	Consequences	Minimal number of Weyl nodes
No	No	Weyl nodes can be at any $\boldsymbol{k}$	2
Yes	No	Weyl node at $\boldsymbol{k}_0 \Rightarrow$ node of same chirality at $-\boldsymbol{k}_0$	4
No	Yes	Weyl node at $\boldsymbol{k}_0 \Rightarrow$ node of opposite chirality at $-\boldsymbol{k}_0$	2
Yes	Yes	No separated Weyl nodes	None

Table 1.1: Consequences of time-reversal and inversion symmetry on the location and minimal number of Weyl points.

bands which are protected by topology and always come in pairs of opposite chirality. To detect these Weyl points experimentally they need to sit at the Fermi energy. The charge density and therefore chemical potential of a three-dimensional system can not easily be controlled by electrostatic gating (as for example in graphene). This means that a lot of 3d materials have Weyl points somewhere in their band structure, which typically do not contribute to transport as they sit far away from the Fermi level.

To conclude this section on Weyl semimetals we want to look into the consequences if additional symmetries are present. For this, we consider a single Weyl point at momentum $\boldsymbol{k}_0$ and arbitrary chirality:

$$H(\boldsymbol{k} \approx \boldsymbol{k}_0) = \pm \hbar v \boldsymbol{\sigma} \cdot (\boldsymbol{k} - \boldsymbol{k}_0)\,. \tag{1.12}$$

Let us start in a system with time-reversal symmetry which maps $\boldsymbol{k} \to -\boldsymbol{k}$ and $\boldsymbol{\sigma} \to -\boldsymbol{\sigma}$. Thus, the Hamiltonian transforms into

$$H(-\boldsymbol{k} \approx \boldsymbol{k}_0) = \pm \hbar v \boldsymbol{\sigma} \cdot (\boldsymbol{k} + \boldsymbol{k}_0) \tag{1.13}$$

and we will have another Weyl node of the **same** chirality at momentum $-\boldsymbol{k}_0$. As we have seen before, due to fermion doubling, each Weyl node needs a partner of opposite chirality. So in total there are at least 4 Weyl points if time-reversal symmetry is present.

Next, we look at inversion symmetry which leaves the spin unchanged but maps $\boldsymbol{k} \to -\boldsymbol{k}$. Here, the Hamiltonian becomes

$$H(-\boldsymbol{k} \approx \boldsymbol{k}_0) = \mp \hbar v \boldsymbol{\sigma} \cdot (\boldsymbol{k} + \boldsymbol{k}_0)\,. \tag{1.14}$$

In this case, the node at $\boldsymbol{k}_0$ has a partner with **opposite** chirality at $-\boldsymbol{k}_0$. Thus, the total Chern number is zero and no additional nodes are required by symmetry. If both inversion and time-reversal symmetry are present there can be no separated Weyl nodes

as opposite chiralities would be superimposed and therefore annihilated. In the absence of both symmetries Weyl points of opposite chirality are independent in $\boldsymbol{k}$-space and can even sit at different energies. These conclusions are summarized in Table 1.1.

In reality, three-dimensional samples have surfaces that terminate the crystal bulk. We can project each Weyl point from the bulk onto these 2d surface Brillouin zones. Due to the topology of the Weyl points there will be a one-dimensional surface state connecting the projections. These so called Fermi-arcs have been the topic of a lot of research [16–18], but as they will not be of too much interest in the scope of this thesis, we will not further elaborate on this subject.

1.3.2 Dirac semimetals

In the previous chapter we have seen that Weyl crossings of two bands are forbidden if time-reversal and inversion symmetry are present simultaneously. Let us now consider a system of four bands with Hamiltonian

$$H_D = \hbar v \tau_x \otimes (\boldsymbol{\sigma} \cdot \boldsymbol{k}) = \begin{pmatrix} 0 & \hbar v(\boldsymbol{\sigma} \cdot \boldsymbol{k}) \\ \hbar v(\boldsymbol{\sigma} \cdot \boldsymbol{k}) & 0 \end{pmatrix}. \tag{1.15}$$

The eigenvalues are $\epsilon_{\boldsymbol{k}} = \pm\hbar v|\boldsymbol{k}|$ where each of the positive and negative energy bands are now doubly degenerate. Fig. 1.3 a) shows the linear band crossing of four bands at $\boldsymbol{k} = 0$, which is called a Dirac point in three dimensions. The Chern number (1.10) of a Fermi surface enclosing this point is zero and there is no topological protection. We can view the Hamiltonian (1.15) as the superposition of two energetically degenerate Weyl points with opposite chirality. Therefore, the total Chern number of all four bands cancels [19].

In this basis, the combined symmetry operator of time-reversal and inversion can be written as $\mathcal{TI} = i\tau_z \otimes \sigma_y K_c$ with K_c meaning complex conjugation. The band crossing of our Hamiltonian is not protected by this symmetry as we can write down a mass term $H_m = m\tau_z \otimes \mathbb{1}$ which is symmetry allowed but still opens a gap in the spectrum. This leads to a dispersion $\epsilon_{\boldsymbol{k}} = \pm\sqrt{(\hbar v)^2|\boldsymbol{k}|^2 + m^2}$ as seen in Fig. 1.3 b). To ensure symmetry protection of a Dirac crossing, rotation symmetries are required. Examples for materials with such symmetry-protected Dirac points are Cd_3As_2 and Na_3Bi which have C_4 and C_6 symmetries, respectively [20, 21]. Invariance under 180° rotation (C_2 symmetry) is not sufficient as in this case time-reversal partners do not have different eigenvalues and can still be gapped by H_m.

Even though these Dirac points in three dimensions are not inherently topological, they can still be split into a pair of Weyl points when time-reversal symmetry is broken, e.g. via a magnetic field, which is described by $H_b = b\ \mathbb{1} \otimes \sigma_z$. The total Hamiltonian

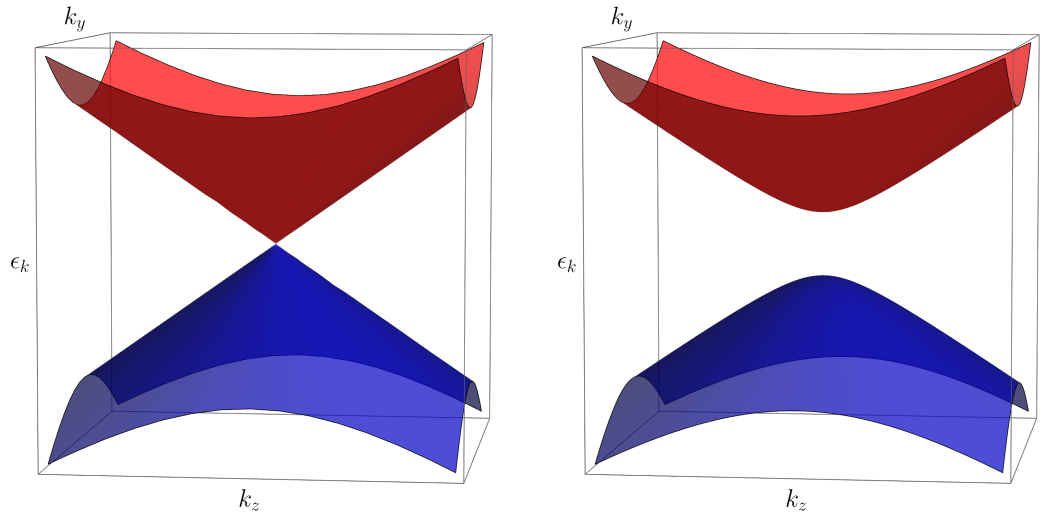

Figure 1.3: Bandstructure $\epsilon_{\boldsymbol{k}}$ of the Dirac Hamiltonian (1.15) for $k_x = 0$: a) Dirac semimetal with doubly degenerate bands crossing at $k_y = k_z = 0$ for $m = 0$. b) Including a mass term gives a trivial insulator with a bandgap for $m = 0.5\hbar v$.

$H = H_D + H_m + H_b$ in this case becomes

$$H = \begin{pmatrix} m+b & 0 & \hbar v k_z & \hbar v(k_x - ik_y) \\ 0 & m-b & \hbar v(k_x + ik_y) & -\hbar v k_z \\ \hbar v k_z & \hbar v(k_x - ik_y) & -m+b & 0 \\ \hbar v(k_x + ik_y) & \hbar v k_z & 0 & -m-b \end{pmatrix}, \tag{1.16}$$

with energies $\epsilon_{\boldsymbol{k}} = \pm\sqrt{\hbar^2 v^2(k_x^2 + k_y^2) + \left(\sqrt{m^2 + \hbar^2 v^2 k_z^2} \pm b\right)^2}$ where the two $\pm$ signs are independent of each other. We see that the magnetic field lifts the degeneracy of the eigenvalues and, for $|b| > |m|$, splits the four-band crossing into two Weyl points along the z-direction as shown in Fig. 1.4 a).

1.4 Nodal line semimetals

So far, we have seen that in a magnetic field a Dirac point can be split into two Weyl points along a certain direction in momentum space. Another possible term that breaks time-reversal symmetry of our Dirac Hamiltonian (1.15) is $H_{b'} = b'\,\tau_z \otimes \sigma_x$. For this term the Hamiltonian $H = H_D + H_m + H_{b'}$ becomes

$$H = \begin{pmatrix} m & b' & \hbar v k_z & \hbar v(k_x - ik_y) \\ b' & m & \hbar v(k_x + ik_y) & -\hbar v k_z \\ \hbar v k_z & \hbar v(k_x - ik_y) & -m & -b' \\ \hbar v(k_x + ik_y) & \hbar v k_z & -b' & -m \end{pmatrix}, \tag{1.17}$$

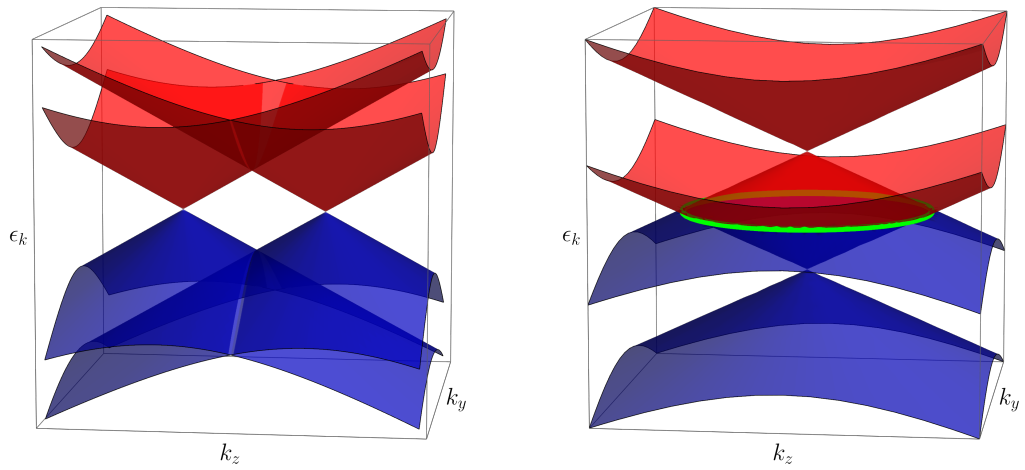

Figure 1.4: Lifting the degeneracy of a four-fold crossing by breaking time-reversal symmetry. Band structures are shown for $k_x = 0$. a) Splitting the Dirac point into two Weyl cones of opposite chirality at $k_z = \pm(b^2 - m^2)/(\hbar v)$ using (1.16) for $|b| > |m|$. b) For each degenerate band the symmetry breaking term in (1.17) shifts one band up and one down in energy. This leads to a nodal line of band crossings at $\epsilon_{\boldsymbol{k}} = 0$ shown in green with a radius $k_r = (b'^2 - m^2)/(\hbar v)$.

with eigenvalues $\epsilon_{\boldsymbol{k}} = \pm\sqrt{(\hbar v k_x)^2 + \left(\sqrt{m^2 + \hbar^2 v^2 (k_y^2 + k_z^2)} \pm b'\right)^2}$. Going to polar coordinates in the yz-plane with $k_y = k\cos(\theta)$ and $k_z = k\sin(\theta)$ one obtains $\epsilon_{\boldsymbol{k}} = \pm\sqrt{(\hbar v k_x)^2 + (\sqrt{m^2 + \hbar^2 v^2 k^2} \pm b')^2}$ with $k > 0$. Therefore, in the plane defined by $k_x = 0$ two bands can cross at $\epsilon_{\boldsymbol{k}} = 0$ if $k = (b'^2 - m^2)/(\hbar v)$ for $|b'| > |m|$. This defines a circle $k_y^2 + k_z^2 = (b'^2 - m^2)/(\hbar v)$ of linear band crossings called a nodal line. For each degenerate pair of bands (e.g. the red ones with $\epsilon > 0$ in Fig. 1.3) $H_{b'}$ shifts one of the bands up in energy while moving the other one down by the same amount. This leads to the line crossing, indicated in Fig. 1.4 b) by the green circle. For $k_x \neq 0$ the spectrum is always gapped. Here, we have neglected a possible momentum dependence of the mass term $m(\boldsymbol{k})$. In this case, the line crossing will not occur at constant energy and therefore can not be at the Fermi level. On the other hand, if the system is described sufficiently by Eq. (1.17) and sits at finite chemical potential $0 < \mu < b'$, the Fermi surface is a torus.

We will later see when we derive the low-energy Hamiltonian describing $ZrTe_5$ that a nodal line crossing can also be achieved by breaking inversion symmetry and at least one mirror-symmetry, which defines the plane in which the line crossings appear.

To summarize, there are a lot of condensed matter realizations of the Dirac equation. They host a plethora of novel and interesting physical phenomena and are thus at the forefront of solid state material research. Symmetries and topology play a central role in protecting these band crossings from gapping out. In the remainder of this thesis we will focus on electronic transport properties, mainly for nodal line semimetals.

2 Electronic transport in solids

Transport measurements have been a part of material classifications for a long time. Metals like copper are great electric conductors while other materials like, for example, diamond are insulating. These properties are mainly influenced by the electronic band structure and the degree of disorder. Even though the conductivity of a system does not provide direct insight into the underlying physical mechanisms, there have been a lot of fundamental insights gained through transport. Two examples are the chiral anomaly in Weyl semimetals [10] or the topological protection of Dirac surface states [22, 23]. The main part of this chapter deals with the semi-classical Boltzmann equation, which we will employ in the following chapters to compute various transport properties. Additionally, we will also illustrate the quantum mechanical description of disorder and linear response theory via the Kubo formula. At the end of the chapter the phenomenon of quantum oscillations will be explained. Here, we introduce a very important separation of time scales depending on which kind of excitations are considered.

2.1 Drude theory of linear conductivity

The earliest theory of electronic transport in solids is the Drude model [24, 25] which treats the electrons as classical particles which carry a charge e and have an effective mass m_{eff}. These electrons get accelerated by an applied electric field E and are subject to friction characterized by a transport scattering time τ_{tr}. We emphasize that this time scale is different from the conventional scattering time τ as not all scattering events are relevant for transport properties[1]. The resulting current density is given by $j = \sigma E$ with the Drude conductivity $\sigma = \frac{ne^2\tau_{\text{tr}}}{m_{\text{eff}}}$ where n is the density of electrons. In general, the electric field and current density are three-dimensional vectors. Thus, the conductivity σ becomes a tensor relating all field directions and resulting currents $\boldsymbol{j} = \sigma \boldsymbol{E}$. The next step to a more refined theory is to consider the quantum mechanical statistics of electrons which will lead us to the Boltzmann transport equation.

2.2 Boltzmann equation

The main method applied to calculate transport properties in this thesis will be the Boltzmann equation. Due to the electrons obeying fermionic statistics we have a lot of particles at finite energy and with finite momentum, even at $T = 0$. In equilibrium no

[1] For example, forward scattering (or small-angle scattering) does not lead to a decay of a current. This issue will become important later in the context of quantum oscillations

current is flowing as the number of particles with positive and negative momenta are equal. Applying an external field leads to a deviation from the Fermi-Dirac distribution and enables transport. We describe the electrons in a certain band[2] n as wave-packets which have a certain distribution function $f_n(\boldsymbol{r}, \boldsymbol{k}, t)$ that depends on position $\boldsymbol{r}$, momentum $\boldsymbol{k}$ and time t. This semi-classical description is valid if we are interested in transport properties on length scales larger than the wavelength of electrons.
The distribution function can change due to different mechanisms, the first being due to scattering with e.g. defects, phonons or other electrons. These effects are combined into the collision integral $I[f] = \frac{\partial f}{\partial t}\big|_{\text{coll}}$.
Furthermore, the momentum of the wave-packet will change due to external forces

$$\dot{\boldsymbol{k}} = \frac{1}{\hbar}\boldsymbol{F} = -\frac{e}{\hbar}\left(\boldsymbol{E} + \boldsymbol{v}_k \times \boldsymbol{B}\right), \tag{2.1}$$

coming from electric and magnetic fields. Lastly we consider the change due to a flow of particles. The corresponding velocity is given by

$$\dot{\boldsymbol{r}} = \boldsymbol{v}_k = \frac{1}{\hbar}\frac{\partial \epsilon(\boldsymbol{k})}{\partial \boldsymbol{k}} - \hbar\dot{\boldsymbol{k}} \times \boldsymbol{\Omega}(\boldsymbol{k}), \tag{2.2}$$

which contains the band velocity as well as the so-called anomalous velocity arising from the Berry curvature $\boldsymbol{\Omega}(\boldsymbol{k})$. Collecting all these contributions leads us to the Boltzmann equation:

$$\frac{\partial f}{\partial t} + \boldsymbol{v}_k \cdot \frac{\partial f}{\partial \boldsymbol{r}} + \frac{1}{\hbar}\boldsymbol{F} \cdot \frac{\partial f}{\partial \boldsymbol{k}} = \left.\frac{\partial f}{\partial t}\right|_{\text{coll}}. \tag{2.3}$$

In the case of homogeneous, time-independent fields the first two terms on the left side vanish as the distribution function $f(\boldsymbol{k})$ only depends on momentum in this case. To describe deviations from equilibrium, we write $f(\boldsymbol{k}) = f_0(\boldsymbol{k}) + \delta f(\boldsymbol{k})$ with the equilibrium state $f_0(\boldsymbol{k}) = f_0(\epsilon_{\boldsymbol{k}} - \mu)$ being the Fermi-Dirac distribution. In the following chapters we will expand $\delta f = f^{(1)} + f^{(2)} + f^{(3)} + (...)$ in powers of the electric field with $f^{(1)} \sim E$, $f^{(2)} \sim E^2$ and so on. This allows us to solve the Boltzmann equation iteratively order by order in perturbation theory.
After simplifying the left side of Eq. (2.3) we turn to the collision integral. This term can describe different scattering mechanisms with the most common ones being impurity scattering, electron-electron interactions or coupling to quasi-particles, e.g. to phonons. In the case of impurity scattering the collision integral takes the form:

$$\left.\frac{\partial f}{\partial t}\right|_{\text{coll}} = -\int W_{k'k} f(\boldsymbol{k})(1 - f(\boldsymbol{k}'))\frac{\mathrm{d}\boldsymbol{k}'}{(2\pi)^d} + \int W_{kk'} f(\boldsymbol{k}')(1 - f(\boldsymbol{k}))\frac{\mathrm{d}\boldsymbol{k}'}{(2\pi)^d}. \tag{2.4}$$

Here, the first term describes scattering processes out of the state $\boldsymbol{k}$ into $\boldsymbol{k}'$ which decrease $f(\boldsymbol{k})$. The second term covers the opposite events which scatter into $\boldsymbol{k}$ and thus

[2] We will omit the band index n in the following until it becomes relevant again.

increase $f(\boldsymbol{k})$. For elastic scattering the transition rates can be written as $W_{k'k} = \frac{2\pi}{\hbar} |\langle k'|\Delta H|k\rangle|^2 \delta(\epsilon_k - \epsilon_{k'})$. Thus, collisions conserve particle number and energy but only change the momentum and distribution of electrons. Due to the symmetry $W_{kk'} = W_{k'k}$ the scattering term is simply linear in the distribution function:

$$\left.\frac{\partial f}{\partial t}\right|_{\text{coll}} = \int W_{kk'}(f(\boldsymbol{k}') - f(\boldsymbol{k}))\frac{\mathrm{d}\boldsymbol{k}'}{(2\pi)^d}. \tag{2.5}$$

As mentioned above, the distribution function consists of an equilibrium part $f_0(\boldsymbol{k})$ and a perturbation $\delta f(\boldsymbol{k})$. The equilibrium state is uniquely defined by the condition $\int W_{kk'}(f_0(\boldsymbol{k}') - f_0(\boldsymbol{k}))\frac{\mathrm{d}\boldsymbol{k}'}{(2\pi)^d} = 0$. This allows us to write the Boltzmann equation without magnetic fields to linear order as

$$\frac{e}{\hbar}\boldsymbol{E}\cdot\frac{\partial f_0(\boldsymbol{k})}{\partial \boldsymbol{k}} = -\int M_{kk'} f^{(1)}(\boldsymbol{k}')\frac{\mathrm{d}\boldsymbol{k}'}{(2\pi)^d}, \tag{2.6}$$

with the scattering kernel $M_{kk'} = \delta(\boldsymbol{k} - \boldsymbol{k}')\int W_{kk''}\frac{\mathrm{d}\boldsymbol{k}''}{(2\pi)^d} - W_{kk'}$. The solution to this equation can be (in principle) easily written down as

$$f^{(1)}(\boldsymbol{k}) = \int (M^{-1})_{kk'}\frac{e}{\hbar}\boldsymbol{E}\cdot\boldsymbol{v}_{k'}\frac{\partial f_0(\boldsymbol{k})}{\partial \epsilon_{\boldsymbol{k}'}}\frac{\mathrm{d}\boldsymbol{k}'}{(2\pi)^d}. \tag{2.7}$$

In practice, inverting the scattering kernel $M_{kk'}$ is not trivial due to conservation laws. For each conserved quantity, M has a left eigenvector with eigenvalue 0. As two examples we will consider particle number and energy conservation. Because collisions preserve particle number we have $\frac{\mathrm{d}}{\mathrm{d}t}\sum_{\boldsymbol{k}} f_{\boldsymbol{k}} = 0$. This implies

$$\int \frac{\mathrm{d}\boldsymbol{k}}{(2\pi)^d} M_{kk'} = 0 \tag{2.8}$$

for all momenta $\boldsymbol{k}'$. Therefore, the constant vector $(1, 1, 1, ...)$ is a left eigenvector of the matrix M with eigenvalue 0. A similar statement can be made for the conservation of energy under elastic collisions

$$\frac{\mathrm{d}}{\mathrm{d}t}\sum_{\boldsymbol{k}} \epsilon_{\boldsymbol{k}} f_{\boldsymbol{k}} = \int \frac{\mathrm{d}\boldsymbol{k}}{(2\pi)^d}\epsilon_{\boldsymbol{k}} M_{kk'} = 0. \tag{2.9}$$

Here, the left eigenvector with eigenvalue 0 is the vector $(\epsilon_{\boldsymbol{k_1}}, \epsilon_{\boldsymbol{k_2}}, \epsilon_{\boldsymbol{k_3}}, ...)$ where each entry contains the energy of the corresponding momentum point. Therefore, a straightforward inversion of the full scattering kernel is mathematically problematic.
As collisions relax the system back to equilibrium in a certain time scale we can approximate the collision integral by

$$\left.\frac{\partial f}{\partial t}\right|_{\text{coll}} \approx -\frac{f(\boldsymbol{k}) - f_0(\boldsymbol{k})}{\tau_{\text{tr}}(\boldsymbol{k})}, \tag{2.10}$$

with a momentum-dependent transport scattering time $\tau_{\mathrm{tr}}(\boldsymbol{k})$. This time scale should be chosen such that it obeys

$$\frac{f^{(1)}(\boldsymbol{k})}{\tau_{\mathrm{tr}}(\boldsymbol{k})} = \int W_{kk'}(f(\boldsymbol{k}') - f(\boldsymbol{k}))\frac{\mathrm{d}\boldsymbol{k}'}{(2\pi)^d}. \tag{2.11}$$

Within this **relaxation-time approximation**, we can now calculate the linear response to an applied electric field from

$$\frac{e}{\hbar}\boldsymbol{E}\cdot\frac{\partial f_0(\boldsymbol{k})}{\partial \boldsymbol{k}} = -\frac{f^{(1)}(\boldsymbol{k})}{\tau_{\mathrm{tr}}(\boldsymbol{k})}, \tag{2.12}$$

which can be easily solved for $f^{(1)}(\boldsymbol{k})$. This allows us to write the full distribution function in the presence of an electric field as

$$f(\boldsymbol{k}) = f_0(\boldsymbol{k}) - \frac{e}{\hbar}\tau_{\mathrm{tr}}(\boldsymbol{k})\boldsymbol{E}\cdot\frac{\partial f_0(\boldsymbol{k})}{\partial \boldsymbol{k}} = f_0(\boldsymbol{k}) - \frac{e}{\hbar}\tau_{\mathrm{tr}}(\boldsymbol{k})\boldsymbol{E}\cdot\boldsymbol{v}_k\frac{\partial f_0(\boldsymbol{k})}{\partial \epsilon_{\boldsymbol{k}}}, \tag{2.13}$$

where in the last step we have rewritten the momentum derivative to an energy derivative by multiplying with the velocity $\boldsymbol{v}_k$. This is useful as the Fermi-Dirac distribution is only a function of $\epsilon_{\boldsymbol{k}}$ and not explicitly of the momentum. At $T = 0$, all states up to the chemical potential are occupied so the derivative w.r.t. energy is simply $\frac{\partial f_0(\boldsymbol{k})}{\partial \epsilon_{\boldsymbol{k}}} = -\delta\left(\epsilon_{\boldsymbol{k}} - \mu\right)$. Interpreting Eq. (2.13) as the first two terms of a Taylor expansion, we can write

$$f(\boldsymbol{k}) \approx f_0\left(\boldsymbol{k} - \frac{e}{\hbar}\tau_{\mathrm{tr}}\boldsymbol{E}\right) \tag{2.14}$$

for a constant scattering time τ_{tr}. This means that the Fermi distribution gets shifted by a vector proportional to $\tau_{\mathrm{tr}}\boldsymbol{E}$. Due to this shift there can be a non-zero current after averaging over all momenta

$$\boldsymbol{j} = -e\int\frac{\mathrm{d}\boldsymbol{k}}{(2\pi)^d}\boldsymbol{v}_k f^{(1)}(\boldsymbol{k}) = \frac{e^2}{\hbar}\int\frac{\mathrm{d}\boldsymbol{k}}{(2\pi)^d}\boldsymbol{v}_k\tau_{\mathrm{tr}}(\boldsymbol{k})\boldsymbol{E}\cdot\boldsymbol{v}_k\frac{\partial f_0(\boldsymbol{k})}{\partial \epsilon_{\boldsymbol{k}}}. \tag{2.15}$$

This expression shows that not all electrons contribute to transport but only those close to the Fermi energy. At first glance, this seems to be contradicting the Drude formula from the previous chapter where the total electron density n entered. But it turns out that the Boltzmann equation reproduces the Drude formula for the longitudinal conductivity if we assume a constant transport scattering time and take $\boldsymbol{v}_k \sim \frac{\partial \epsilon_{\boldsymbol{k}}}{\partial \boldsymbol{k}}$ to be the band velocity. In this case, the conductivity is given by

$$\sigma_{ii} = \frac{j_i}{E_i} = \frac{ne^2\tau_{\mathrm{tr}}}{m_{\mathrm{eff}}}, \tag{2.16}$$

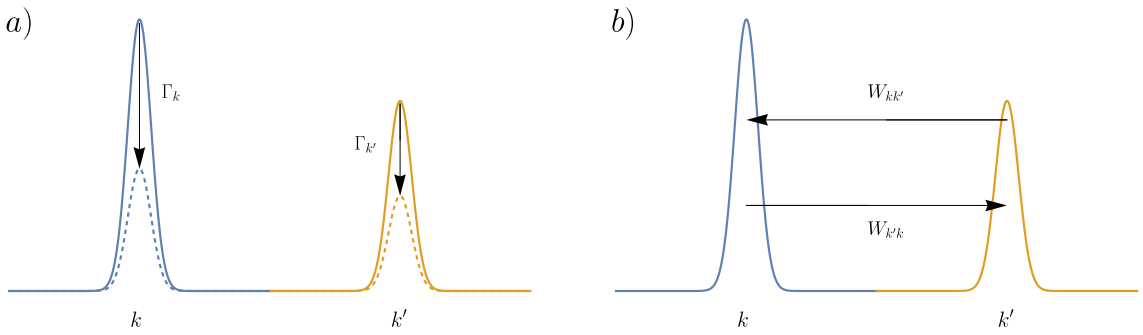

Figure 2.1: Equilibration in the relaxation-time approximation and for microscopic scattering mechanism. The two peaks represent the occupation function at different momenta. a) If each mode has a separate relaxation rate $\Gamma_k \sim 1/\tau_{\mathrm{tr}}$ there is no interplay between the modes. Here, particle number and energy are not conserved. b) For the microscopic scattering mechanism there will be an exchange of particles between the k-modes. This guarantees that conservation laws are fulfilled if a summation over all momenta is performed.

where $n = \int \frac{\mathrm{d}\boldsymbol{k}}{(2\pi)^d} f_0(\boldsymbol{k})$ is the electron density and the effective mass is defined by

$$\frac{1}{m_{\mathrm{eff}}} = \frac{\int \frac{\mathrm{d}\boldsymbol{k}}{(2\pi)^d} \frac{\partial^2 \epsilon_{\boldsymbol{k}}}{\partial k_i^2} f_0(\boldsymbol{k})}{\int \frac{\mathrm{d}\boldsymbol{k}}{(2\pi)^d} f_0(\boldsymbol{k})}. \tag{2.17}$$

Unfortunately, the simple relaxation time approximation for the collision term violates the conservation laws for particle number and energy as

$$\frac{\mathrm{d}}{\mathrm{d}t} \sum_{\boldsymbol{k}} f_{\boldsymbol{k}} = \frac{e}{\hbar} \frac{\mathrm{d}}{\mathrm{d}t} \sum_{\boldsymbol{k}} \tau_{\mathrm{tr}}(\boldsymbol{k}) \boldsymbol{E} \cdot \frac{\partial f_0(\boldsymbol{k})}{\partial \boldsymbol{k}} \neq 0, \tag{2.18}$$

$$\frac{\mathrm{d}}{\mathrm{d}t} \sum_{\boldsymbol{k}} \epsilon_{\boldsymbol{k}} f_{\boldsymbol{k}} = \frac{e}{\hbar} \frac{\mathrm{d}}{\mathrm{d}t} \sum_{\boldsymbol{k}} \tau_{\mathrm{tr}}(\boldsymbol{k}) \epsilon_{\boldsymbol{k}} \boldsymbol{E} \cdot \frac{\partial f_0(\boldsymbol{k})}{\partial \boldsymbol{k}} \neq 0. \tag{2.19}$$

In the relaxation-time approximation each $\boldsymbol{k}$-mode at the Fermi energy relaxes to equilibrium in a time scale set by $\tau_{\mathrm{tr}}(\boldsymbol{k})$ independent of what the other modes $\boldsymbol{k}'$ do. If we compare this with the microscopic scattering term (2.4) one recognizes that information is lost, as we no longer know into which states particles with momentum $\boldsymbol{k}$ are scattered[3]. As this balance of in- and out-scattering of particles is ignored when using the relaxation-time approximation, conservation laws can not be fulfilled. An illustration of this is shown in Fig. 2.1. This obstruction of the relaxation-time approximation can be circumvented by additionally requiring $\sum_{\boldsymbol{k}} \delta f_{\boldsymbol{k}} = 0$ for $\tau_{\mathrm{tr}}(\boldsymbol{k}) = \tau_{\mathrm{tr}} = \mathrm{const}$.

For a rotation-invariant system with $\epsilon_{\boldsymbol{k}} = \epsilon(|\boldsymbol{k}|)$ we can derive an analytic expression for the transport scattering time. We will be working with randomly placed impurities,

[3] As well as information about the opposite process where states $\boldsymbol{k}'$ are scattered into $\boldsymbol{k}$.

which generate a potential $U(\boldsymbol{r}) = \sum_i u(\boldsymbol{r} - \boldsymbol{R}_i)$. After averaging over all possible impurity positions $\boldsymbol{R}_i$ we obtain the averaged transition rates between two states as

$$\overline{W}_{\boldsymbol{k}\boldsymbol{k}'} = \frac{2\pi}{\hbar} n_{\text{imp}} |u_{\boldsymbol{k}-\boldsymbol{k}'}|^2 \delta(\epsilon_k - \epsilon_{k'}), \tag{2.20}$$

where $u_{\boldsymbol{q}}$ is the Fourier transform of the single-impurity potential $u(\boldsymbol{r})$ and n_{imp} is the impurity density. Let us for now assume that we work in a three-dimensional setting where the band velocity is $\boldsymbol{v}_{\boldsymbol{k}} = \frac{1}{\hbar}\frac{\partial \epsilon_{\boldsymbol{k}}}{\partial \boldsymbol{k}} = \frac{\hbar}{m}\boldsymbol{k}$ due to rotation symmetry. If we plug this into the collision term (2.5), the linearized Boltzmann equation in an electric field reads

$$\frac{e}{m}\boldsymbol{E}\cdot\boldsymbol{k}\frac{\partial f_0(\boldsymbol{k})}{\partial \epsilon_{\boldsymbol{k}}} = \frac{2\pi}{\hbar} n_{\text{imp}} \int \frac{\mathrm{d}^3 k'}{(2\pi)^3} |u_{\boldsymbol{k}-\boldsymbol{k}'}|^2 \delta(\epsilon_k - \epsilon_{k'})(f^{(1)}(\boldsymbol{k}') - f^{(1)}(\boldsymbol{k})). \tag{2.21}$$

To solve this equation we can use the ansatz $f^{(1)}(\boldsymbol{k}) = \boldsymbol{E}\cdot\boldsymbol{k}\eta(\epsilon_k)$ with an unknown function η, which only depends on the energy and thus the magnitude of k but not on the momentum direction. This is motivated by the fact that we want the response to be linear in the applied field and dependent on momentum. Additionally, the distribution function has to be a scalar quantity. If the scattering potential is also rotation-symmetric the potential in momentum space will only depend on the magnitude $|\boldsymbol{k}|$ and the angle ϑ between $\boldsymbol{k}$ and $\boldsymbol{k}'$. Choosing the z-axis in the direction of $\boldsymbol{k}$ our equation in spherical coordinates for an arbitrary orientation of $\boldsymbol{E}$ becomes

$$\begin{aligned}\frac{e}{m}\boldsymbol{E}\cdot\boldsymbol{k}\frac{\partial f_0(\boldsymbol{k})}{\partial \epsilon_{\boldsymbol{k}}} &= n_{\text{imp}} \int \frac{\mathrm{d}k' k'^2}{2\pi} \delta(\epsilon_k - \epsilon_{k'})\eta(\epsilon_k) \int_0^\pi \mathrm{d}\vartheta\, \sin(\vartheta)|u(k',\vartheta)|^2 E_z\,(k'\cos(\vartheta) - k) \\ &= \frac{\pi}{2} n\; n_{\text{imp}}\eta(\epsilon_k)\rho(\epsilon_k) \int_0^\pi \mathrm{d}\vartheta\, \sin(\vartheta)|u(\vartheta)|^2\,(\cos(\vartheta) - 1)\,\boldsymbol{E}\cdot\boldsymbol{k},\end{aligned} \tag{2.22}$$

where in the second line we have replaced the momentum integral by the density of states $\rho(\epsilon)$ and the electron density n. Comparing this with the Boltzmann equation in the relaxation time approximation (2.12) we can read of the transport scattering time as

$$\frac{1}{\tau_{\text{tr}}(\boldsymbol{k})} = \frac{\pi}{2} n\; n_{\text{imp}}\rho(\epsilon_k) \int_0^\pi \mathrm{d}\vartheta\, \sin(\vartheta)|u(\vartheta)|^2\,(1 - \cos(\vartheta))\,. \tag{2.23}$$

The reduction factor $1 - \cos(\vartheta)$ distinguishes the transport scattering time from the conventional lifetime $\tau(\boldsymbol{k})$ of an excitation at $\boldsymbol{k}$. This can be understood because a small scattering angle ϑ only leads to a small change in the velocity $\boldsymbol{v}_{\boldsymbol{k}}$ and therefore does not significantly contribute to the decay of the current. These processes are thus weighted less in the total transport scattering rate.

So far, we have mostly neglected the anomalous velocity $\boldsymbol{v}_{\text{anom}} = -\hbar\dot{\boldsymbol{k}} \times \boldsymbol{\Omega}(\boldsymbol{k})$. In a

homogeneous system, this term will not give a contribution to the distribution function. However, Berry curvatures can lead to transport responses as the velocity enters into the definition of the current

$$j_m = -e \int \frac{\mathrm{d}\boldsymbol{k}}{(2\pi)^d} \left(\frac{1}{\hbar} \frac{\partial \epsilon(\boldsymbol{k})}{\partial k_m} - (\boldsymbol{F} \times \boldsymbol{\Omega}(\boldsymbol{k}))_m \right) \cdot (f_0(\boldsymbol{k}) + \delta f(\boldsymbol{k})). \tag{2.24}$$

To linear order in the electric field, the anomalous velocity generates a Hall current which is proportional to the equilibrium distribution function $f_0(\boldsymbol{k})$. The corresponding conductivity is given by

$$\sigma_{mn}^{\mathrm{anom}} = e^2 \int \frac{\mathrm{d}\boldsymbol{k}}{(2\pi)^d} \epsilon_{mnl} \Omega_l(\boldsymbol{k}) f_0(\boldsymbol{k}). \tag{2.25}$$

The resulting current will always be perpendicular to the external electric field and thus does not give a contribution to the longitudinal conductivity. As the perturbation of the distribution function does not enter this expression, the anomalous Hall conductivity is independent of the transport scattering time $\sigma_{mn}^{\mathrm{anom}} \sim \tau_{\mathrm{tr}}^0$. Therefore, it is often referred to as an intrinsic mechanism.

2.3 Disorder and self-energy

For a realistic description of quantum materials it is necessary to consider disorder which breaks the translation symmetry of the system. Possible examples can be impurities, which are induced during the growth process or grain boundaries of differently ordered parts of a sample. As mentioned previously, such impurities act as sources of scattering and enable finite conductivities in solids. Therefore, they need to be considered in any theory that aims to obtain finite conductivities. Additionally, disordered systems allow us to study new and more exotic electronic states. Below three dimensions even a small amount of disorder can lead to the localization of electrons and absence of diffusive states which is known as Anderson localization [26]. For doped semiconductors or 3d topological insulators long-ranged disorder potentials can form due to charged impurities. These charge puddles can enable transport through an otherwise insulating bulk system and have been experimentally observed using optical spectroscopy [27, 28]. Furthermore, the stability of the quantized plateaus in the resistivity for the integer quantum Hall effect require a certain amount of disorder to be present [29]. Therefore, disorder opens up many new exciting phenomena and is not just an annoyance that one tries to get rid of.

In the following section, we want to describe the impact of disorder on the wavefunction and see how impurities are related to the broadening of the density of states. In this context, we introduce the concept of the self-energy and derive the program to calculate

it in self-consistent Born approximation.

2.3.1 Self-consistent Born approximation

The goal of this section is to illustrate the theoretical methods to treat disorder and its influence on the electrons in a solid. We start from a single impurity placed at $\boldsymbol{R} = 0$ with disorder potential $u(\boldsymbol{r})$. The eigenenergies of the clean system with a single impurity are determined by the equation

$$(H + u(\boldsymbol{r}))\,\psi(\boldsymbol{r}) = \epsilon\psi(\boldsymbol{r}), \tag{2.26}$$

where the wave function obeys the Lippmann-Schwinger equation

$$\psi(\boldsymbol{r}) = \psi_0(\boldsymbol{r}) + \int \mathrm{d}\boldsymbol{r'} G_0(\boldsymbol{r} - \boldsymbol{r'}) u(\boldsymbol{r'}) \psi(\boldsymbol{r'}), \tag{2.27}$$

with ψ_0 being the wave function of the clean system and the free Greens function in momentum space given by $G_0(\epsilon, \boldsymbol{k}) = (\epsilon - H(\boldsymbol{k}) + i\delta)^{-1}$. If multiple bands are considered and the Hamiltonian has a matrix structure the Greens function is also a matrix of same dimensions. As Eq. (2.27) is a self-consistent equation for $\psi(\boldsymbol{r})$, we can instead rewrite it using operator inversion into a form where the wavefunction in the presence of the impurity only appears on one side of the equation. Next, we perform a perturbative expansion in the disorder potential $u(\boldsymbol{r})$ which gives us the Born series

$$\begin{aligned}\psi(\boldsymbol{r}) = \psi_0(\boldsymbol{r}) &+ \int \mathrm{d}\boldsymbol{r'} G_0(\boldsymbol{r} - \boldsymbol{r'}) u(\boldsymbol{r'}) \psi_0(\boldsymbol{r'}) \\ &+ \int \mathrm{d}\boldsymbol{r'}\mathrm{d}\boldsymbol{r''} G_0(\boldsymbol{r} - \boldsymbol{r'}) u(\boldsymbol{r'}) G_0(\boldsymbol{r'} - \boldsymbol{r''}) u(\boldsymbol{r''}) \psi_0(\boldsymbol{r''}) + \mathcal{O}(u^3).\end{aligned} \tag{2.28}$$

In a real material we, of course, do not deal with a single impurity but with a macroscopic number of them. Therefore, we model the disorder as the superposition of N_{imp} point-like impurities at random locations $\boldsymbol{R}_i$ which generate a potential $U(\boldsymbol{r}) = \sum_{i=1}^{N_{\mathrm{imp}}} u(\boldsymbol{r} - \boldsymbol{R}_i)$. Instead of the wavefunction we can also consider the full Greens function of the disordered system which also is defined by a Lippmann-Schwinger equation

$$G(\boldsymbol{r_1}, \boldsymbol{r_2}) = G_0(\boldsymbol{r_1} - \boldsymbol{r_2}) + \int \mathrm{d}\boldsymbol{r'} G_0(\boldsymbol{r_1} - \boldsymbol{r'}) U(\boldsymbol{r'}) G(\boldsymbol{r'} - \boldsymbol{r_2}). \tag{2.29}$$

In this case the Born series to n-th order contains all possible scattering events where the electrons interact with n impurities. For example, we can scatter every time from the same impurity or have scattering events where different impurities contribute. As the location of the impurities are unknown and we are dealing with a large number of them, such a straightforward expansion of the Greens function is not viable. Therefore, we divide our

system into subsystems with the size set by the decoherence length l_d. On this length scale, enough scattering events take place for the phase of the wavefunction to be fully random. For a macroscopic sample this length scale is usually still small compared to the system size and we have a large number of subsystems. This allows us to perform an impurity average over all possible disorder configurations. As a consequence, on average translation symmetry is restored in our system and we can work again in momentum space. Here, the impurity-averaged Greens function will be diagonal with $\langle G(k,k')\rangle_{\text{imp}} = \boldsymbol{G}(k) \sim \delta_{k,k'}$ as after the averaging all random phases force the total in- and out-going momenta of a scattering event to be the same.

Performing the impurity average for the Born series of our full Greens function and only keeping the irreducible diagrams[4] leaves us with the Dyson equation for our Greens function

$$\boldsymbol{G}(\boldsymbol{k}) = \boldsymbol{G}_0(\boldsymbol{k}) + \boldsymbol{G}_0(\boldsymbol{k})\boldsymbol{\Sigma}_{\boldsymbol{k}}(\omega)\boldsymbol{G}(\boldsymbol{k}). \tag{2.30}$$

Diagrammatically this equation can be illustrated as

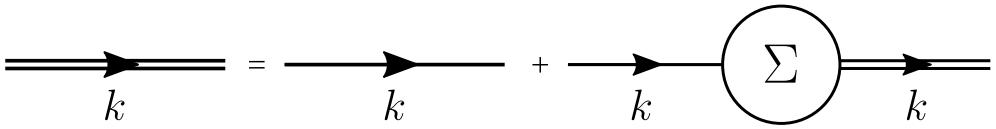

with single fermion lines for the free Greens function, a self-energy bubble and double fermion lines for the full Greens function. Here, $\boldsymbol{\Sigma}_k(\omega)$ is the frequency-dependent self-energy. From the Dyson equation (2.30) we can obtain the full Greens function of the disordered system as

$$\boldsymbol{G}(\boldsymbol{k}) = \left(\boldsymbol{G}_0(\boldsymbol{k})^{-1} - \boldsymbol{\Sigma}_{\boldsymbol{k}}(\omega)\right)^{-1}. \tag{2.31}$$

In this expression we can interpret the self-energy as the broadening of states compared to the clean system described by the free Greens function $\boldsymbol{G}_0(\boldsymbol{k})$. Therefore, the self-energy is also related to the scattering time via $\frac{1}{\tau_{\boldsymbol{k}}} = -2\ \text{Tr}\left(\text{Im}\boldsymbol{\Sigma}_{\boldsymbol{k}}(\omega)\right)$. The self-energy contains all irreducible diagrams which can be sorted in orders of impurity density as follows

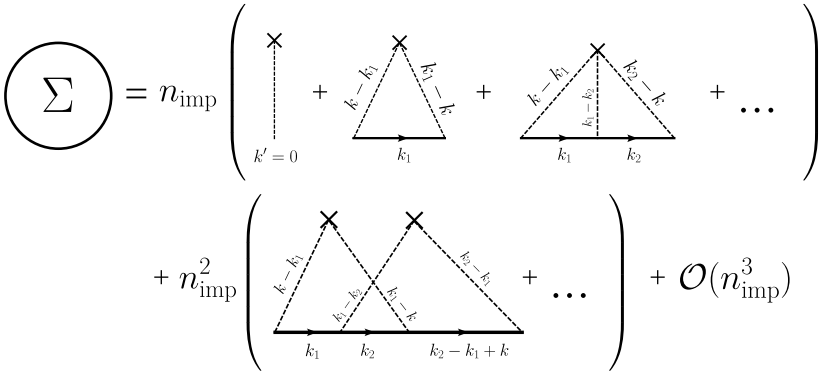

[4]These are the diagrams where we can not cut the Greens function line without crossing any of the scattering lines.

In the limit of weak impurity scattering a good approximation for the self-energy is obtained by only taking terms linear in impurity density. This is known as the Born approximation. In this case, the first term $\sim n_{\mathrm{imp}} u_0$ can be absorbed as a constant shift of the chemical potential μ. If we replace the free fermion line in the next diagram by the full Greens function we obtain the self-energy in **self-consistent Born approximation**

$$\boldsymbol{\Sigma}_{\mathrm{SCBA}}(\omega) = n_{\mathrm{imp}} u_0^2 \int \frac{\mathrm{d}\boldsymbol{k}'}{(2\pi)^d} \boldsymbol{G}(\boldsymbol{k}'). \tag{2.32}$$

The corresponding diagram for this approximation is

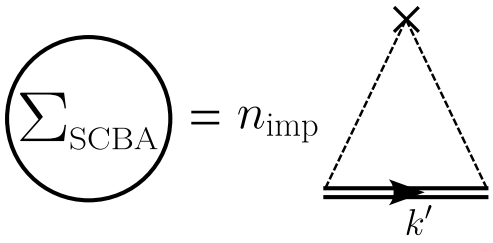

The density of states (DoS) $\nu(\epsilon)$ of the disordered system is given by the trace of the imaginary part of the full Greens function

$$\nu(\epsilon) = -\frac{1}{\pi} \mathrm{Tr} \left(\mathrm{Im} \int \frac{\mathrm{d}\boldsymbol{k}'}{(2\pi)^d} \boldsymbol{G}(\boldsymbol{k}') \right), \tag{2.33}$$

where the trace is taken over all degrees of freedom like spin and orbitals. We will use this quantity as a measure of convergence in our self-consistent calculation of $\boldsymbol{G}(\boldsymbol{k})$ and $\boldsymbol{\Sigma}_{\mathrm{SCBA}}(\omega)$. Starting from an ansatz for the self-energy Σ_{init}, we can iterate the equations (2.31) and (2.32) until the density of states $\nu(\epsilon)$ has converged. Once the DoS as a function of energy is known, one can obtain the carrier density via integration up to the chemical potential

$$n(\mu) = \int_0^\mu \nu(\epsilon) \mathrm{d}\epsilon. \tag{2.34}$$

Depending on the setting in which one employs these techniques, the Greens function will depend on additional parameters, like, for example, the magnetic field strength. To compare our theoretical calculations with experimental results which are taken at fixed density n_0 one needs to determine the correct chemical potential from $n(\mu, B) = n_0$.

After capturing the effects of disorder we now turn to the calculation of linear transport properties using diagrammatics. The self-energy will serve as a mechanism to decay the current response and produce a finite conductivity.

2.4 Linear response theory

For a fully quantum-mechanical description of transport properties we employ linear response theory. This chapter follows reference [30]. The current response to an applied vector potential is given by

$$\langle j^\alpha(t)\rangle = i\int \mathrm{d}^3x'\mathrm{d}t'\Theta(t-t')\langle\left[j^\alpha(x), j^\beta(x')\right]\rangle A^\beta(x'), \tag{2.35}$$

where the Heaviside theta function $\Theta(t-t')$ ensures causality. This integral contains the two-point correlation function of the current. Going to momentum- and frequency space, the longitudinal response function without vertex corrections is given by

$$\Pi_{\alpha\alpha}(i\omega) = \frac{1}{\beta}\sum_{\omega_n}\int\frac{\mathrm{d}^3k}{(2\pi)^3}\mathrm{Tr}\left[j_\alpha \boldsymbol{G}(i\omega_n + i\omega, \boldsymbol{k}) j_\alpha \boldsymbol{G}(i\omega_n, \boldsymbol{k})\right] \tag{2.36}$$

with current operators $j_\alpha = e\frac{\partial H}{\partial k_\alpha}$ and the Matsubara frequencies $\omega_n = (2n+1)\pi/\beta$ where $n \in \mathbb{Z}$ and β is the inverse temperature. Diagrammatically, the response function without vertex corrections is given by the bare conductivity bubble

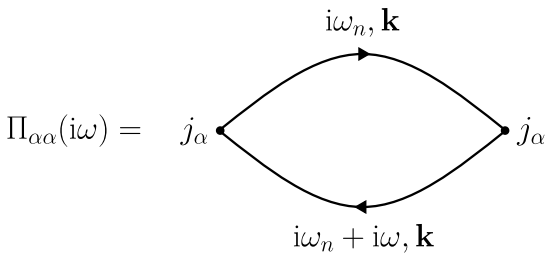

Neglecting vertex corrections means ignoring all diagrams where the two lines of this bubble are connected by at least one impurity scattering line. This simplification ignores the effects of anisotropic scattering but to leading order these should be captured by the Greens function in self-consistent Born approximation.
The summation over Matsubara frequencies can be performed by a contour integral along a circle with radius going to infinity in the complex plane

$$\Pi_{\alpha\alpha}(i\omega) = \int\frac{\mathrm{d}^3k}{(2\pi)^3}\int\frac{\mathrm{d}z}{2\pi i}n_F(z)\mathrm{Tr}\left[j_\alpha \boldsymbol{G}(z+i\omega, \boldsymbol{k}) j_\alpha \boldsymbol{G}(z, \boldsymbol{k})\right], \tag{2.37}$$

where $n_F(z)$ is the Fermi-Dirac distribution. To return to the real frequency domain we perform an analytic continuation by setting $i\omega \to \omega + i\delta$

$$\begin{aligned}\Pi_{\alpha\beta}(\omega) = \int\frac{\mathrm{d}\epsilon}{2\pi}n_F(\epsilon)\int\frac{\mathrm{d}^3k}{(2\pi)^3}\mathrm{Tr}[&\left(\boldsymbol{G}^R(\epsilon,\boldsymbol{k}) - \boldsymbol{G}^A(\epsilon,\boldsymbol{k})\right) j_\alpha \boldsymbol{G}^A(\epsilon-\omega,\boldsymbol{k}) j_\beta \\ &+ \boldsymbol{G}^R(\epsilon+\omega,\boldsymbol{k}) j_\alpha \left(\boldsymbol{G}^R(\epsilon,\boldsymbol{k}) - \boldsymbol{G}^A(\epsilon,\boldsymbol{k})\right) j_\beta].\end{aligned} \tag{2.38}$$

Here, $\boldsymbol{G}^R(\epsilon,\boldsymbol{k}) = (\epsilon - H(\boldsymbol{k}) - \Sigma)^{-1}$ is the retarded Greens function and $\boldsymbol{G}^A(\epsilon,\boldsymbol{k}) = \left(\boldsymbol{G}^R(\epsilon,\boldsymbol{k})\right)^\dagger = \left(\epsilon - H(\boldsymbol{k}) - \Sigma^\dagger\right)^{-1}$ is the advanced Greens function. As we are interested in the DC conductivities of our system we evaluate the limit

$$\sigma_{\alpha\beta} = -\lim_{\omega\to 0}\frac{\Pi_{\alpha\beta}(\omega)}{\omega}. \tag{2.39}$$

Therefore, we write $\boldsymbol{G}^{R/A}(\epsilon\pm\omega,\boldsymbol{k}) = \boldsymbol{G}^{R/A}(\epsilon,\boldsymbol{k}) \pm \frac{\partial \boldsymbol{G}^{R/A}}{\partial\epsilon}\omega + \mathcal{O}(\omega^2)$ where all higher orders will vanish in the limit $\omega\to 0$. The remaining terms are

$$\begin{aligned}\sigma_{\alpha\beta} = \int\frac{\mathrm{d}\epsilon}{4\pi}n_F(\epsilon)\int\frac{\mathrm{d}^3k}{(2\pi)^3}\mathrm{Tr}\Big[&-\left(\boldsymbol{G}^R(\epsilon,\boldsymbol{k}) - \boldsymbol{G}^A(\epsilon,\boldsymbol{k})\right)j_\alpha\frac{\partial\boldsymbol{G}^A}{\partial\epsilon}j_\beta \\ &+ \frac{\partial\boldsymbol{G}^R}{\partial\epsilon}j_\alpha\left(\boldsymbol{G}^R(\epsilon,\boldsymbol{k}) - \boldsymbol{G}^A(\epsilon,\boldsymbol{k})\right)j_\beta\Big].\end{aligned} \tag{2.40}$$

Using partial integration we can move some of the energy derivatives from the Greens functions to the Fermi function. At zero temperature this derivative is just given by the Dirac delta distribution $\frac{\partial n_F(\epsilon)}{\partial\epsilon} = -\delta(\mu-\epsilon)$. Therefore, for these terms we only need the Greens function at the chemical potential. Collecting all these terms yields

$$\sigma^{(I)}_{\alpha\beta} = \frac{1}{2\pi}\int\frac{\mathrm{d}^3k}{(2\pi)^3}\mathrm{Re}\left(\mathrm{Tr}\left[\boldsymbol{G}^R(\mu,\boldsymbol{k})j_\alpha\left(\boldsymbol{G}^R(\mu,\boldsymbol{k}) - \boldsymbol{G}^A(\mu,\boldsymbol{k})\right)j_\beta\right]\right). \tag{2.41}$$

The remaining terms will still contain an energy integration over the Fermi function

$$\begin{aligned}\sigma^{(II)}_{\alpha\beta} = \int\frac{\mathrm{d}\epsilon}{4\pi}n_F(\epsilon)\int\frac{\mathrm{d}^3k}{(2\pi)^3}\mathrm{Tr}\Big[&\frac{\partial\boldsymbol{G}^R}{\partial\epsilon}j_\alpha\boldsymbol{G}^R(\epsilon,\boldsymbol{k})j_\beta + \boldsymbol{G}^A(\epsilon,\boldsymbol{k})j_\alpha\frac{\partial\boldsymbol{G}^A}{\partial\epsilon}j_\beta \\ &- \boldsymbol{G}^R(\epsilon,\boldsymbol{k})j_\alpha\frac{\partial\boldsymbol{G}^R}{\partial\epsilon}j_\beta - \frac{\partial\boldsymbol{G}^A}{\partial\epsilon}j_\alpha\boldsymbol{G}^A(\epsilon,\boldsymbol{k})j_\beta\Big].\end{aligned} \tag{2.42}$$

This term describes the anomalous Hall effect coming from Berry curvatures which are captured in the energy derivatives of the Greens function. For the longitudinal conductivity this term cancels as tracing over a product is cyclic $\mathrm{Tr}[AB] = \mathrm{Tr}[BA]$. In conclusion, $\sigma^{(II)}_{\alpha\alpha} = 0$ and the longitudinal conductivity without vertex corrections can be computed by the Kubo formula

$$\sigma_{\alpha\alpha} = \frac{1}{2\pi}\int\frac{\mathrm{d}^3k}{(2\pi)^3}\mathrm{Re}\left(\mathrm{Tr}\left[\boldsymbol{G}^R(\mu,\boldsymbol{k})j_\alpha\left(\boldsymbol{G}^R(\mu,\boldsymbol{k}) - \boldsymbol{G}^A(\mu,\boldsymbol{k})\right)j_\alpha\right]\right). \tag{2.43}$$

We will use both the self-consistent Born approximation as well as the Kubo formula in section 5.7 to compute the conductivity parallel and perpendicular to a magnetic field.

To finish this chapter we will consider the phenomenon of quantum oscillations which are a very useful experimental tool to measure the Fermi surface of a material and obtain various parameters relevant for transport properties.

2.5 Quantum oscillations

This section is based on the review article "Topological Insulator Materials" J. Phys. Soc. Jpn. 82, 102001 (2013) [31].

In a magnetic field the electrons in a material form quantized Landau levels. Therefore, the density of states (DoS) at the Fermi level will be periodically modulated as a function of magnetic field. This can lead to periodic changes in different physical observables, known as quantum oscillations. Once all electrons are in the lowest Landau level there are no more oscillations, giving us an upper field B_{QL} above which oscillations die out. In this case one speaks of the system being in the quantum limit. One prominent example are the de Haas-van Alphen oscillations in the magnetic susceptibility [32]. As this thesis mainly deals with electronic transport properties, we will focus on oscillations in the electrical resistivity, known as Shubnikov-de Haas oscillations (SdH) [33]. These oscillations in R_{xx} can be used to describe 2d surface states as well as 3d bulk conducting states. Additionally, they allows us to detect Berry phases through phase shifts in the oscillations. To analyse the SdH oscillations, it is necessary to subtract a background resistance to obtain the oscillating part ΔR_{xx}, see Fig. 2.2. Using the Lifshitz-Kosevich formula [33] the oscillating component of the resistance can be expressed as

$$\Delta R_{xx} \sim R_T R_D R_S \cos\left[2\pi\left(\frac{F}{B} - \frac{1}{2} + \beta\right)\right], \tag{2.44}$$

with the frequency F measured in Tesla (just like the magnetic field) and $0 \leq \beta \leq 1$ accounting for phase shifts due to Berry curvature. Through these phases, it is possible to distinguish surface and bulk states. Here, $R_T = 2\pi^2 k_B T/(\hbar\omega_c \sinh[2\pi^2(k_B T)/(\hbar\omega_c)])$ with the cyclotron frequency $\omega_c \sim B$ is the temperature damping factor. This term describes the broadening of the occupation function for each state due to temperature which will reduce the oscillation amplitude. Next, $R_D = \exp\left(-2\pi^2 \frac{k_B T_D}{\hbar\omega_c}\right)$ is called the Dingle damping term with the Dingle temperature $T_D = \hbar/(2\pi k_B \tau_D)$ where τ_D is the scattering time. This factor takes into account the reduction of amplitude due to a finite scattering time τ_D which can be related to an effective temperature T_D. Therefore, it is hard to see quantum oscillations in very disordered samples as the amplitude will be exponentially suppressed. The last reduction factor $R_S = \cos\left(\frac{1}{2}\pi g m^*/m_0\right)$ is the spin damping that depends on the electronic g-factor g, the cyclotron mass m^* and the bare electron mass m_0. The magnetic field splits spin up and down electrons by the Zeeman effect, giving us two oscillations with a small phase shift. The superposition of these two paths leads to the spin damping factor R_S. It should be noted that the phase shift β is just the Berry phase γ of the electron path in momentum space divided by 2π.

Using SdH oscillations it is possible to extract a lot of information about the band structure and Fermi surface of a material. For example, in a fixed magnetic field the Dingle damping is constant and we can extract the cyclotron mass from the temperature

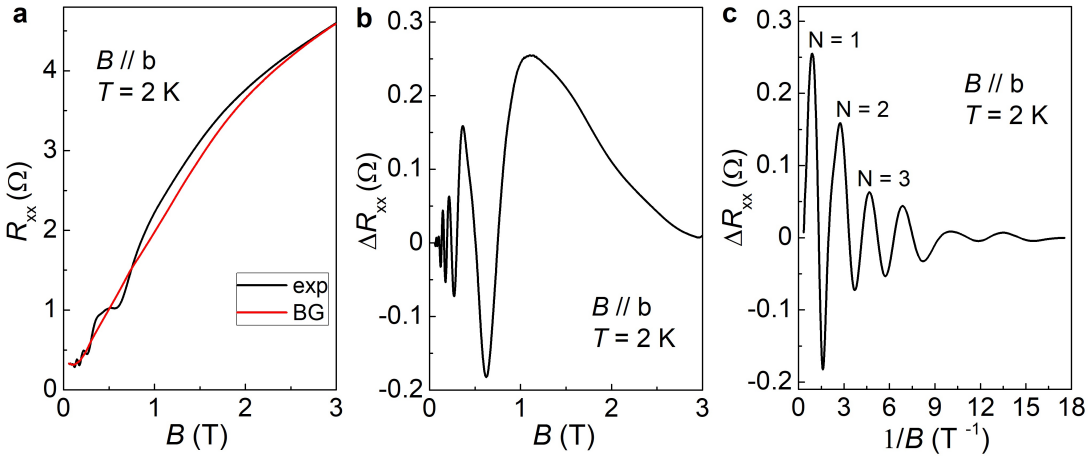

Figure 2.2: Shuhbnikov-de Haas oscillations in $ZrTe_5$. a) Longitudinal resistance as a function of magnetic field. The red fit shows a polynomial which is used to subtract the background component. b) Oscillating part ΔR_{xx} of the resistance. c) When plotting ΔR_{xx} as a function of $1/B$ the periodicity of the oscillations becomes visible. Figures taken from publication 1 [34].

dependence of the oscillation amplitude as only R_T changes. As the electrons will run along extremal orbits on the Fermi surface the cyclotron mass is given by

$$m^* = \frac{\hbar^2}{2\pi}\left(\frac{\partial A(E)}{\partial E}\right)_{E=E_F}, \tag{2.45}$$

where $A(E_F)$ is the area enclosed by such an extremal orbit perpendicular to the applied field. For a 2d system with a linear dispersion we have $E(k) = \hbar v_F|\boldsymbol{k}|$ with an area $A(E_F) = \pi k_F^2 = \pi E_F^2/(\hbar^2 v_F^2)$ for a magnetic field perpendicular to the 2d plane. This results in a cyclotron mass $m^* = E_F/v_F^2 = \hbar k_F/v_F$. From this, we can compute the cyclotron frequency ω_c via

$$m^* = \frac{eB}{\omega_c}. \tag{2.46}$$

Additionally, it is possible to extract the scattering time from the Dingle damping factor. Here, temperature is kept fixed and one analyses the magnetic field dependence of the oscillation amplitude. Plotting $\ln(\mathrm{A}/\mathrm{R_T})$ vs $1/B$ one can extract the Dingle temperature T_D as the linear slope of the data. The corresponding time scale τ_D is different from the transport scattering time τ_{tr} of the previous section as it includes all scattering events regardless of scattering angle. Usually, the fact that small-angle scattering leads to a decay of quantum oscillations while not affecting the transport manifests as $\tau_{\mathrm{tr}} > \tau_D$ [5].

From Eq. 2.44 we can also see that the SdH oscillations are periodic in $1/B$. Fourier transforming $R_{xx}(B^{-1})$ allows us to read off the oscillation frequencies as peaks in the spectrum. If there are multiple orbits the measured SdH oscillations will be a superposition of different frequencies. Each frequency F_{k^*} will correspond to an extremal orbit of the

[5] We will see in chapter 4.2 that this only hold for homogeneous systems.

Fermi surface and is given by the area A_{k^*} perpendicular to the applied field enclosed by such an orbit:

$$F_{k^*} = \frac{\hbar}{2\pi e} A_{k^*}. \tag{2.47}$$

Using this relation, one can determine the parameters of any metallic model with a band structure by calculating the Fermi surface, determining the extremal orbits as well as the corresponding areas, and fitting the SdH frequencies to the results. Knowing the shape of the Fermi surface through the extremal orbits we can also determine the Fermi volume which gives us information about the carrier density n. We will apply this procedure in section 3.4 and go into more detail there.

To summarize, in this chapter we have developed the necessary tools to calculate transport properties in homogeneous systems using the semi-classical Boltzmann equation. Comparing to the theory of quantum oscillations, we recognized two different time scales τ and τ_{tr} as not all scattering events lead to a decay in the current. Additionally, we have seen how to calculate the linear conductivity using the Kubo formula where the self energy contains the impact of disorder and is treated in self-consistent Born approximation.

3 Experimental system: $ZrTe_5$

This chapter is based on the publication 1: "Gigantic magnetochiral anisotropy in the topological semimetal $ZrTe_5$" Phys. Rev. Lett. 128, 176602 (2022) and its supplementary material [34].

3.1 Crystal structure and previous experiments

Zirconium pentatelluride ($ZrTe_5$) grows as a 3d bulk crystal in an orthorhombic layered structure, see Fig. 3.1 a) [35]. Each layer is formed by $ZrTe_3$ chains extending in the crystallographic a-direction which are connected by additional Te atoms. These layers are stacked along the b-direction and are bound together by van der Waals interactions. For transport experiments the crystallographic axes a, c, b correspond to the x, y, z directions. $ZrTe_5$ has already been a prominently studied material with a big focus on transport experiments [35–44]. A few examples include the chiral magnetic effect, unconventional anomalous Hall effect and 3d quantum Hall effect. Due to its special crystal structure, $ZrTe_5$ is a highly anisotropic material with a hierarchy of Fermi velocities $v_b \ll v_c < v_a$, shown by different groups through ARPES or quantum oscillation measurements [37, 45].

It was shown that most samples of $ZrTe_5$ undergo a transition from a strong 3d topological insulator (TI) state to a weak 3d TI (layered 2d TI states) with increasing temperature [46]. At the critical point T_p the system thus should be in a Dirac semimetal state as the energy gap closes, see Fig. 3.1 b). When measuring the resistivity ρ_{xx} as a function of temperature, a clear peak at T_p is visible. In the semimetal state the conduction and valence band will touch at the Γ-point in the middle of the Brillouin zone. For such samples, the resistivity peaks around temperature zero. By doping the system to a finite chemical potential the Fermi surface will become an ellipsoid (due to the velocity anisotropies) around this point [42].

The alleged space group of $ZrTe_5$ is *Cmcm* (D_{2h}^{17}). However, recent works such as the one cited at the beginning of this chapter as well as by other groups [47] indicate that the actual symmetry is much lower. X-ray diffraction (XRD) experiments performed by Sebastian Biesenkamp in the group of Prof. Markus Braden suggest a breaking of the mirror-plane symmetries m_{ab} and m_{ac} as well as the absence of inversion symmetry [34]. Additionally, the existence of certain responses in transport experiments can give conclusive evidence of the absence or presence of symmetries. This will be the topic of the next section.

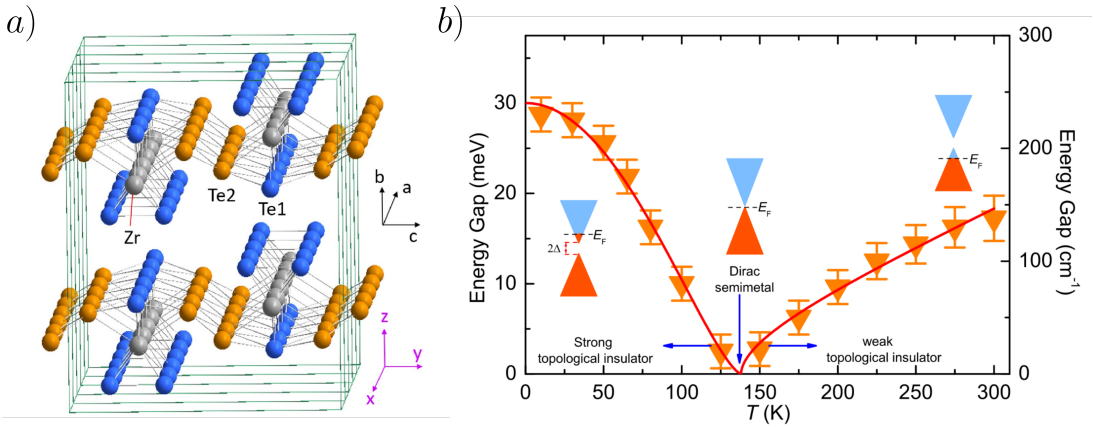

Figure 3.1: a) Crystal structure of $ZrTe_5$: The $ZrTe_3$ prisms form chains along the a-direction which are connected by additional Te atoms. This structure is stacked along the b-direction with the sheets interacting via van der Waals forces. b) Phase diagram of $ZrTe_5$: As a function of temperature the system changes from a strong to a weak topological insulator. At the transition point T_p the gap closes and a semimetal is realized. Figure taken from [46]

3.2 Motivation for symmetry breaking: Magnetochiral anisotropy

The theoretical work in this thesis was initiated by a series of experiments mainly performed by Yongjian Wang in the group of Prof. Yoichi Ando. As a function of temperature, the samples used for these experiments show a clear peak of the longitudinal resistivity ρ_{xx} at zero temperature as shown in Fig. 3.2 a). Thus, they sit right at the phase transition between strong- and weak topological insulator and the mass gap has been carefully tuned to zero.

Applying a low-frequency AC current $I = I_0 \sin(\omega t)$, the longitudinal resistivity ρ_{xx} was measured. Surprisingly, the data shows a sizable second-harmonic voltage $V_{2\omega}$, which is quadratic in the applied current I and changes sign when the magnetic field direction is reversed, see Fig. 3.2 b). This indicates that there is *nonreciprocal* transport in this system, meaning that the resistance is different for a current $\boldsymbol{I}$ flowing to the right $(+I)$ or to the left $(-I)$. Such an effect is only allowed if inversion symmetry is absent[1]. The magnetochiral anisotropy (MCA) is an effect where nonreciprocal transport is enabled by an external magnetic field [48]. There are two types of this effect, depending on the generation mechanism: Firstly, the inner-product type with resistance $R = R_0 \left[1 + \gamma(\boldsymbol{B} \cdot \boldsymbol{I})\right]$, where R_0 is the reciprocal resistance and γ measures the size of the nonlinearity [49]. From the formula we can see that the nonreciprocal resistance is maximal when the magnetic field is applied parallel to the current. Furthermore, there is the vector-product type with

[1]This should be known to almost any physicist when his/her desk fills up with dirty coffee cups and the flow back to the kitchen is much smaller than going from the coffee machine to the office.

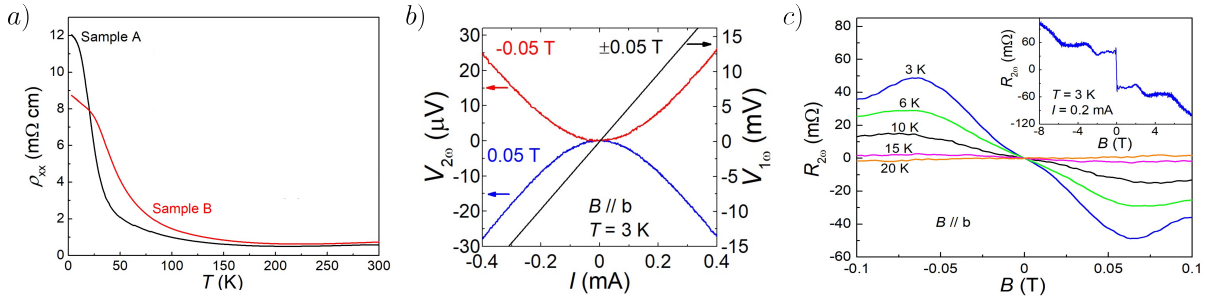

Figure 3.2: a) Longitudinal resistivity as a function of temperature for two samples used in [34]. The peak value is reached at the lowest temperature, indicating that the samples are in the semimetallic state. b) First- and second-harmonic voltage as a function of applied current. $V_{1\omega}$ is linear in I and symmetric under reversal of the magnetic field. $V_{2\omega}$ is quadratic in current and changes sign when $B \to -B$. c) Second-harmonic resistance as a function of magnetic field for different temperatures. The inset shows a larger field range. Figures taken from publication 1 [34].

resistance $R = R_0[1+\gamma(\hat{\boldsymbol{P}}\times\boldsymbol{B})\cdot\boldsymbol{I}]$ [50]. Here, $\hat{\boldsymbol{P}}$ is a unit vector that indicates the direction of symmetry breaking, e.g. through a polarization. For this type, the largest nonreciprocal resistance is obtained when the magnetic field is perpendicular to the current.

Both expressions contain the nonlinear coefficient $\gamma = (R/R_0 - 1)/(|\boldsymbol{B}|\cdot|\boldsymbol{I}|)$ with $\boldsymbol{B} \parallel \boldsymbol{I}$ for the inner-product type and $\boldsymbol{B} \perp \boldsymbol{I}$ for the vector-product case. It measures the size of the MCA. The measured voltage in the setup with the maximal nonreciprocal response is given by $V = R_0 I(1 + \gamma B I)$. If we inject a sinusoidal AC current, this expression becomes $V = R_0 I_0 \sin(\omega t) + \frac{1}{2}\gamma R_0 B I_0^2(1 + \sin(2\omega t - \pi/2))$. From this, we identify the second harmonic resistance $R_{2\omega} = \frac{1}{2}\gamma R_0 B I_0$ as a measure of the nonlinearity. It should be added that there is a phase shift between first- and second-harmonic components. The measured second-harmonic voltage is observed for $\boldsymbol{I} \parallel \hat{a}$ and $\boldsymbol{B} \parallel \hat{b}$. Therefore, the MCA has to be of the vector-product type. In Fig. 3.2 c) $R_{2\omega}$ as a function of magnetic field is shown for different temperatures. The effect is largest for the smallest temperature of 3 K and is almost zero for $T \geq 15$ K. In the small field range of $|B| \leq 0.06$ T the resistance is almost linear in the applied field and grows rapidly to about 60 mΩ. Afterwards, it still increases but way slower, as shown in the inset.

To determine the direction of the unit vector $\hat{\boldsymbol{P}}$ in the vector-type MCA, the second-harmonic voltage was measured for varying magnetic field directions. The result for field rotations in the ab-, bc-, and ac-plane are shown in Fig. 3.3. Here, $R_{2\omega}$ is normalized by $R_0 B$ to exclude the change of the reciprocal response. At very low field of $B = 0.03$ T, the first two measurements show the angle dependence where in both cases θ is measured from the b-axis. In the ac-plane the nonlinear response is essentially zero for all rotation angles φ. The current is always injected along the a-direction and therefore the vector $\hat{\boldsymbol{P}}$ should point along the c-axis. Resistivity measurements up to large temperatures show no signatures of structural phase transitions at high T, as seen in Fig. 3.2 a). Therefore,

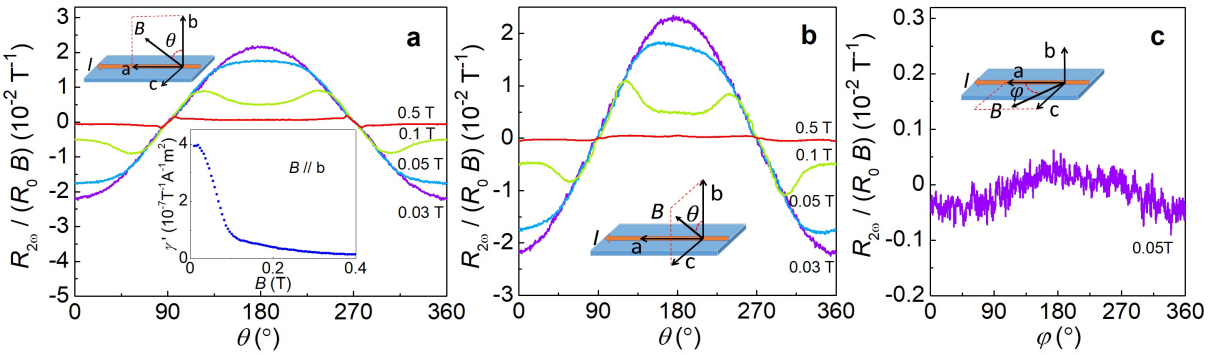

Figure 3.3: Second-harmonic resistance for different directions of the magnetic field. In the first two cases different magnitudes of B were measured with the largest nonlinearity occurring at 0.03 T. The field rotations were performed in all three coordinate planes as indicated by the schematics. The inset in panel a) shows the nonlinear coefficient (defined in the main text) as a function of magnetic field. Figures taken from publication 1 [34].

the symmetry breaking is most likely introduced during crystal growth. From the second-harmonic resistance the nonlinear coefficient can be calculated as $\gamma = 2R_{2\omega}/(R_0 B I_0)$. As this quantity contains the total injected current I_0 it will depend on the sample cross section. Therefore, it is useful to define a more intrinsic coefficient to compare nonlinear effects in multiple samples or even different materials. From now on, we will refer to the nonlinear coefficient γ' defined as

$$\gamma' = A_\perp \gamma = \frac{2A_\perp R_{2\omega}}{R_0 B I_0}, \tag{3.1}$$

where $A_\perp$ is the area cross section perpendicular to the applied current. The inset of Fig. 3.3 a) shows that the nonlinear coefficient is maximal for the smallest fields and we have $\gamma'(B \to 0) = 4 \cdot 10^{-7}$ m^{2}T^{-1}A^{-1}. Compared to other systems showing magnetochiral anisotropies this value is at least an order of magnitude larger than for other known bulk systems [48, 51].

To set up a theoretical description of nonlinear transport in $ZrTe_5$ we first have to develop a model which obeys the same symmetries as the experiments. This will be the topic of the next section.

3.3 Symmetry broken Hamiltonian

According to first principles calculations [35] the four bands describing the low energy physics near the Fermi level are made up of p_y orbitals from Te atoms. These states form two Kramers pairs which we label $\uparrow$ / $\downarrow$. Additionally, each pair has a different parity eigenvalue which we denote as $\tau = \pm 1$. Therefore, the low-energy Hamiltonian can be written in terms of 4×4 matrices $\sigma_i \otimes \tau_j$ with the spin quantization axis being the b-direction. The corresponding basis states are $\left\{\left|\psi_+^\uparrow\right\rangle, \left|\psi_-^\uparrow\right\rangle, \left|\psi_+^\downarrow\right\rangle, \left|\psi_-^\downarrow\right\rangle\right\}$. In this basis

the symmetry operations can be written as follows

- Reflection at the ab-plane: $m_{ab} = i\sigma_y \otimes \tau_z$.
- Reflection at the bc-plane: $m_{bc} = i\sigma_x \otimes \mathbb{1}$.
- Reflection at the ac-plane: $m_{ac} = i\sigma_z \otimes \mathbb{1}$.
- Space inversion: $\mathcal{I} = \mathbb{1} \otimes \tau_z$.
- Time-reversal: $\mathcal{T} = (i\sigma_y \otimes \mathbb{1})K_c$.

Taking all these symmetries into account and only looking at terms linear in momentum, we end up with a Hamiltonian [36] containing all symmetry-allowed terms

$$H_0 = m\mathbb{1} \otimes \tau_z + \hbar\left(v_a k_a \sigma_z \otimes \tau_x + v_b k_b \sigma_x \otimes \tau_x + v_c k_c \mathbb{1} \otimes \tau_y\right) + \mu \mathbb{1}_4, \tag{3.2}$$

where m is the mass gap around the Γ-point and μ is the chemical potential. The sign of m determines whether we are in the weak or strong topological insulator regime. As our samples are located very close to the phase transition point the mass term has to be very small. So far, we have only derived a model for the fully-symmetric Dirac semimetal (with anisotropic velocities). As shown in the previous sections, there is convincing experimental evidence that ab-mirror symmetry m_{ab} and ac-mirror symmetry m_{ac} are broken in our samples. This allows us to write down two additional terms in the Hamiltonian $\mathbb{1} \otimes \tau_x$ and $\sigma_x \otimes \tau_y$ which break m_{ab} and m_{ac}, respectively. Characterizing the strength of the symmetry breaking by energy scales Δ and ξ we obtain

$$H = m\mathbb{1}\otimes\tau_z + \hbar\left(v_a k_a \sigma_z \otimes \tau_x + v_b k_b \sigma_x \otimes \tau_x + v_c k_c \mathbb{1} \otimes \tau_y\right) + \mu\mathbb{1}_4 + \Delta\mathbb{1}\otimes\tau_x + \xi\sigma_x\otimes\tau_y. \tag{3.3}$$

As symmetries are broken now, it is useful to define new (rescaled) momentum coordinates in the bc-plane as $K_1 = v_b k_b \cos(\phi) + v_c k_c \sin(\phi)$ and $K_2 = -v_b k_b \sin(\phi) + v_c k_c \cos(\phi)$. The angle ϕ is determined by $\cos(\phi) = \Delta/\sqrt{\Delta^2 + \xi^2}$. The eigenvalues of our 4×4 Hamiltonian in these coordinates are

$$\epsilon_{\boldsymbol{k}} = \pm\sqrt{m^2 + (\hbar K_2)^2 + \left(\hbar\sqrt{(v_a k_a)^2 + (K_1)^2} \pm \sqrt{\Delta^2 + \xi^2}\right)^2}. \tag{3.4}$$

We have 4 bands as the two $\pm$ signs are unconnected. Two of the bands always have a gap of $\pm\sqrt{m^2 + \Delta^2 + \xi^2}$ compared to $\epsilon = 0$, while the other two bands can cross for $m = 0$ when $\sqrt{(v_a k_a)^2 + (K_1)^2} = \sqrt{\Delta^2 + \xi^2}$ and $K_2 = 0$. An example of this can be seen in Fig. 3.4 a). In this case, the band crossings form a nodal line and the Fermi surface at finite chemical potential is a torus as seen in Fig. 3.4 b). The nodal line will lie in the plane defined by $K_2 = 0$, which coincides with the ab-plane for $\xi = 0$. For finite symmetry breaking of m_{ac}, this plane will be rotated around the a-axis by an angle

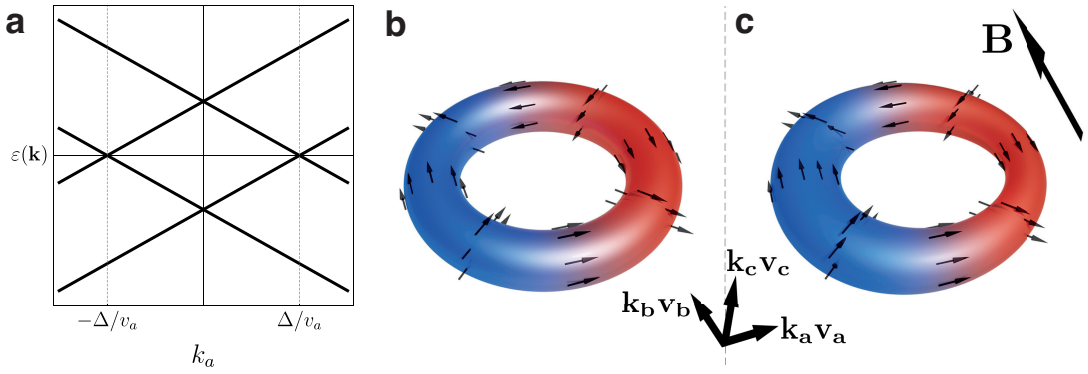

Figure 3.4: a) Band structure along the a-direction for $m = 0 = \xi$. Two bands cross at $k_a = \pm\Delta/v_a$. The dispersion along k_b has the same properties, giving us a nodal line in the ab-plane. b) For finite chemical potential μ the Fermi surface is a torus. Momenta are rescaled by the Fermi velocities to obtain a circular nodal line. The color code indicates the spin components along the b-direction with red and blue being opposite directions. c) For a magnetic field in b-direction the Fermi surface grows (shrinks) in the region where the spin is parallel (anti-parallel) to the field due to the Zeeman effect.

$\theta_{\text{tilt}} = \Delta/\sqrt{\Delta^2 + v_b^2\xi^2/v_c^2} \approx 1 - \frac{v_b^2\xi^2}{2\Delta^2 v_c^2}$. As mentioned in section 3.1, $ZrTe_5$ is an anisotropic material with different Fermi velocities in each direction. As we have $v_b^2 \ll v_c^2$, this tilt angle is expected to be small. Recent experiments on the parallel-field Hall effect in $ZrTe_5$ suggest that even more symmetries are broken [52]. In section 6.2 we show that in this more general case there still exists a nodal line and the Fermi surface is a torus.

In a magnetic field we can include an additional Zeeman term, which breaks time-reversal symmetry. As we are, for now, only interested in the physics at low fields we neglect orbital effects on the Hamiltonian level. For a magnetic field in b-direction we write $H_{\text{Zeeman}} = gB\sigma_z \otimes \mathbb{1}$ with $g = \frac{1}{2}g_b\mu_B$ where g_b is the g-factor for a magnetic field along the b-axis and μ_B is the Bohr magneton for the magnetic moment of an electron. The torus Fermi surface has a particular spin texture, which is typical for topological materials [48] as shown in Fig. 3.4 b). The color code indicates the spin component along b-direction with blue (red) showing S_z parallel (anti-parallel) to $\hat{b}$. As the Zeeman energy favors the spin to align with the applied field, the Fermi surface will enlarge in the region where spins are parallel to $\boldsymbol{B}$. At the same time spins pointing opposite to the field have a higher Zeeman energy and therefore these regions of the Fermi surface shrink. The resulting deformed torus can be seen in Fig. 3.4 c). We will see in the next chapter that this imbalance of spin can lead to nonreciprocal transport via the MCA. As the existence of the nodal line is of significant importance to our understanding of $ZrTe_5$ it is necessary to look for experimental evidence of the torus Fermi surface. Therefore, in the next section we will look at quantum oscillation data and extract the parameters of our model.

3.4 Parameters for toroidal Fermi surface

For three-dimensional materials mapping the bulk band structure via ARPES is not possible. Instead, we can use quantum oscillation measurements to probe the shape of the Fermi surface. For this, the longitudinal resistance R_{xx} was measured as a function of magnetic field in a clean sample of $ZrTe_5$. To determine the shape of the Fermi surface these measurements where performed for different magnetic field orientations in the *bc*- and *ab*-plane. The oscillating part of the resistance as well as the corresponding Fourier spectra for fields in the *bc*-plane can be seen in Fig. 3.5. It is clearly visible that the oscillations for angles up to $\sim 85°$ are composed of multiple frequencies. For each field direction the oscillation frequencies can be extracted from the peaks of the Fourier spectra shown in Fig. 3.5 b), c). These, up to four, peaks are marked with only two different colors as it turns out that we see the original oscillation and their second harmonics in the spectrum. For the peaks F_1 marked in blue a second peak at double frequency can be seen at a lot of different angles. On the other hand, the low frequency oscillations F_1 colored in red are largely submerged in the background component and can only be seen at $\theta = 75°$. Only the second harmonics $2F_1$ can be clearly identified for all field directions. For angles larger than $\theta_c \approx 86°$ only a single, new frequency F_3, marked in green, is observed. This indicates that for field configurations close to 90° the electrons move along a different extremal orbit. When applying the magnetic field in the *b*-direction, the relevant orbits perpendicular to the field are the γ and δ orbits shown in Fig. 3.6 a) [53]. By rotating the field to point along the *c*-axis the extremal orbits will instead become α and β. The fact that we observe multiple frequencies for almost all angles as well as the switching of orbits at a critical angle θ_c are not compatible with an ellipsoidal Fermi surface coming from a single Dirac cone at the Γ-point but is in accordance with the toroidal Fermi surface of a nodal line system at finite chemical potential, see Fig. 3.6 b).

From the δ orbit around the small diameter of the torus we can determine the velocity anisotropy in the *ab*-plane by fitting

$$F_2(\theta) = \frac{2\hbar A(\theta)}{2\pi e} = \frac{\mu^2}{e\hbar^2 v_c v_\perp(\theta)}, \tag{3.5}$$

with $v_\perp(\theta) = \sqrt{v_a^2 \cos^2(\theta) + v_b^2 \sin^2(\theta)}$ where θ is the angle in the *ab*-plane as shown in Fig. 3.6 c). With a ratio $v_a/v_b \approx 16$ the theoretical prediction matches well to the experimental data. For the frequency F_1 of the γ orbit we need to calculate the extremal area numerically as a function of angle. Fitting these results yields a ratio $v_c/v_b \approx 4$. From the β orbit one can determine the absolute value of the Fermi velocities using additionally the cyclotron

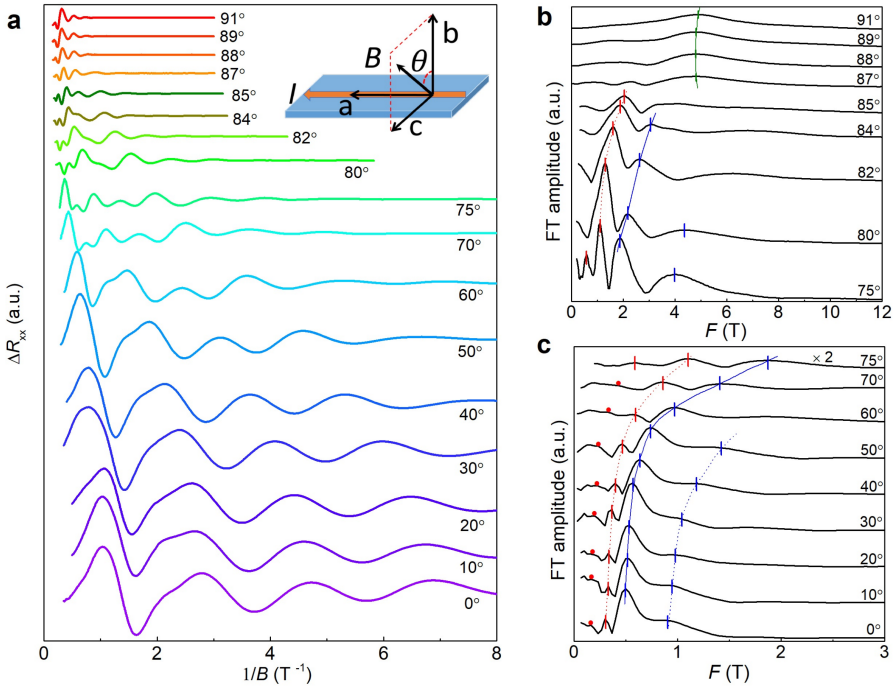

Figure 3.5: a) Quantum oscillations in $ZrTe_5$ for magnetic field rotated in the bc-plane as a function of $1/B$. b),c) Frequency spectrum for different field angles. Two frequencies (red and blue) and their second harmonics can be tracked starting at $\theta = 0$. Close to 90° a new frequency is seen (marked in green). Figures taken from publication 1 [34].

mass obtained from the temperature-dependence of the oscillations in c-direction

$$F_3 = \frac{(\Delta-\mu)^2}{2e\hbar^2 v_a v_b} = 5.0 \text{ T}, \qquad m^* = \frac{\hbar^2}{2\pi}\frac{\partial A}{\partial \mu} = \frac{\Delta-\mu}{v_a v_b} = 0.089 m_e. \tag{3.6}$$

Therefore, the velocities are $v_a = 6.9 \cdot 10^5$ m/s, $v_b = 0.43 \cdot 10^5$ m/s, and $v_c = 1.7 \cdot 10^5$ m/s, which is consistent with previous works [42] even though they assume an ellipsoidal Fermi surface instead of a toroidal one.

Furthermore, these frequencies can be used to determine the chemical potential μ as well as the symmetry breaking Δ. In the b-direction we have $\mu = \sqrt{e\hbar v_c v_a F_2} \approx 4.9$ meV from Eq. (3.5) with $2F_2 = 0.32$ T. With this information and the radius of the β orbit $\Delta - \mu = \frac{2e\hbar F_3}{m^*}$ we have $\Delta \approx 19.1$ meV. These parameters allow us to determine the carrier density, which is given by the Fermi volume of the torus

$$n = \int_{\mathcal{FV}} \frac{\mathrm{d}^3 k}{(2\pi)^3} = \frac{\Delta\mu^2}{4\pi^3\hbar^3 v_a v_b v_c} \approx 2.3 \cdot 10^{16} \text{ cm}^{-3}. \tag{3.7}$$

For a metal we are dealing with a small carrier density and a tiny Fermi surface which can only be seen in very clean samples. Other groups using samples with a resistivity peak at a finite temperature T_p measured an ellipsoidal Fermi surface and obtained densities $n \approx 10^{17}$ cm^{-3} from quantum oscillations [42]. The higher carrier density in such samples

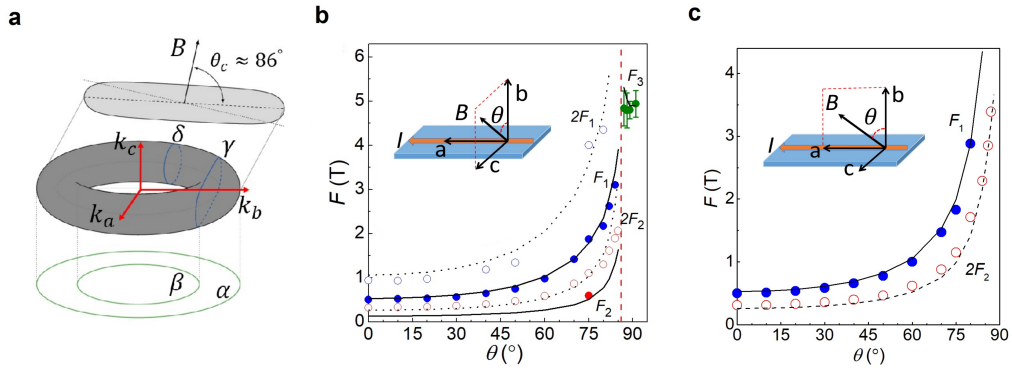

Figure 3.6: a) The extremal orbits of the torus depend on the magnetic field orientation. b) Quantum oscillation frequencies as a function of angle in the bc-plane. F_1 and F_2 correspond to the γ and δ orbits. As F_2 is very small only its second harmonics is experimentally detectable. The lines show theoretical fits to the data points. At the critical angle $\theta_c \approx 86^\circ$ the behavior changes drastically and a new frequency F_3, corresponding to the β orbit, is seen. c) Frequencies for field rotations in the ab-plane. The fits are consistent with the previous results. There is no critical angle where new frequencies emerge. Figures taken from publication 1 [34].

is one of the reasons why the nonlinear effects we will discuss in the following chapters have not been seen before. Usually, higher order terms respecting the crystalline symmetries can significantly change the dispersion as for example via hexagonal warping in topological insulators [54, 55]. As the Fermi surface only encloses a small region in momentum space around the Γ-point, such terms should be small and our linear Hamiltonian provides a good description of $ZrTe_5$.

As mentioned in section 2.5 the Dingle damping factor of the oscillations can be used to determine the relevant scattering times. The linear slope of $\ln(A/R_T)$ as a function of $1/B$ is given by the Dingle temperature T_D of 2.4 K (3.7 K) for a field in b-direction (c-direction). The corresponding scattering times $\tau_D = \hbar/(2\pi k_B T_D)$ in these directions are 500 fs and 320 fs.

To round out the findings from quantum oscillations, it should be mentioned that the nodal line of our model in Eq. (3.3) does not perfectly lie in the ab-plane due to the m_{ac} symmetry breaking $\sim \xi$. We have already previously argued that the tilt angle θ_{tilt} has to be small due to the velocity anisotropy. Additionally, when rotating the field beyond the c-direction the critical frequencies $|\theta_c^{\pm} - 90^\circ|$ are symmetric within the experimental error of 1° which suggests $\xi \ll \Delta$. Therefore, in the following chapter we will focus on the nodal line in the ab-plane with $\xi \approx 0$ and the dispersion in the absence of a magnetic field given by

$$\epsilon_{\boldsymbol{k}} = \pm\sqrt{m^2 + (\hbar v_c k_c)^2 + \left(\hbar\sqrt{(v_a k_a)^2 + (v_b k_b)^2} \pm \Delta\right)^2}. \tag{3.8}$$

4 Magnetochiral anisotropy

This chapter is based on the publication 1: "Gigantic magnetochiral anisotropy in the topological semimetal $ZrTe_5$" Phys. Rev. Lett. 128, 176602 (2022) and its supplementary material [34].

4.1 Boltzmann theory

To simplify the calculation, we map our elongated torus to a circular one by rescaling the momenta $k_i \to vk_i/v_i$ with $i = a, b, c$ and an isotropic velocity v. For convenience, we set $\hbar = 1$ until the end of the calculation. In the ab-plane we can then describe the toroidal Fermi surface in polar coordinates with $k_a = k\cos(\phi)$ and $k_b = k\sin(\phi)$. Including the effect of magnetic fields into the band structure, we also consider the Zeeman term $H_{\text{Zeeman}} = gB\sigma_z \otimes \mathbb{1}$ for a field in b-direction. In this isotropic case the energy of the lowest partially occupied band, for $0 < \mu < \Delta$, up to first order in gB is given by

$$\epsilon_{\boldsymbol{k}} \approx \sqrt{m^2 + (vk_c)^2 + (vk - \Delta)^2} - gB\,\cos(\phi). \tag{4.1}$$

For this isotropic case most transport coefficients can be calculated analytically for $m = 0$. We have checked numerically that the conductivity does not depend on the mass term as long as $|m| \ll \mu$ which is the experimentally relevant regime. As the mass term opens a gap around $\epsilon = 0$ and thus only deforms the dispersion at small energies, it will not have much of an impact on the electrons responsible for transport close to the Fermi level.
Up to first order the Boltzmann equation in relaxation time approximation reads

$$-e\left(\boldsymbol{E} + \boldsymbol{v}_k \times \boldsymbol{B}\right) \cdot \frac{\partial f_0(\boldsymbol{k})}{\partial \boldsymbol{k}} = -\frac{f^{(1)}(\boldsymbol{k})}{\tau_{\text{tr}}(\boldsymbol{k})}. \tag{4.2}$$

Here, we note that $\boldsymbol{v}_k = \frac{\partial \epsilon(\boldsymbol{k})}{\partial \boldsymbol{k}} - \hbar\dot{\boldsymbol{k}} \times \boldsymbol{\Omega}(\boldsymbol{k})$ contains also the anomalous velocity arising from Berry curvatures. This term will give no contribution to the MCA as it is $\sim \boldsymbol{E} \times \boldsymbol{\Omega}(\boldsymbol{k})$ and the response will therefore always be perpendicular to the applied electric field. In this approximation the first-order distribution function for $\boldsymbol{E} = E\hat{a}$ and $\boldsymbol{B} = B\hat{b}$ is given by

$$f^{(1)}(\boldsymbol{k}) = e\tau_{\text{tr}}(\boldsymbol{k}) \left(E\frac{\partial \epsilon_{\boldsymbol{k}}}{\partial k_a} + B \underbrace{\left(\frac{\partial \epsilon_{\boldsymbol{k}}}{\partial k_a}\frac{\partial \epsilon_{\boldsymbol{k}}}{\partial k_c} - \frac{\partial \epsilon_{\boldsymbol{k}}}{\partial k_c}\frac{\partial \epsilon_{\boldsymbol{k}}}{\partial k_a} \right)}_{=0} \right) \frac{\partial f_0}{\partial \epsilon_{\boldsymbol{k}}}. \tag{4.3}$$

As expected, the orbital contribution vanishes to linear order. For $T = 0$ the distribution

function only changes at the Fermi energy and we have $\frac{\partial f_0}{\partial \epsilon_{\boldsymbol{k}}} = -\delta(\mu - \epsilon_{\boldsymbol{k}})$. The band velocity along a-direction is given by

$$\frac{\partial \epsilon_{\boldsymbol{k}}}{\partial k_a} = \frac{\partial \epsilon_{\boldsymbol{k}}}{\partial k}\cos(\phi) - \frac{\partial \epsilon_{\boldsymbol{k}}}{\partial \phi}\frac{\sin(\phi)}{k} = \frac{vk - \Delta}{\sqrt{(v^2 k_c^2 + (vk-\Delta)^2}} - \frac{gB\,\sin^2(\phi)}{k}. \tag{4.4}$$

Using this and assuming a momentum-independent scattering time τ_{tr}, the first order current can be written as

$$j_a^{(1)} = -e\int \frac{\mathrm{d}^3k}{(2\pi)^3} v_a f^{(1)}(\boldsymbol{k}) = e^2 E \tau_{\mathrm{tr}} \int \frac{\mathrm{d}k\mathrm{d}\phi\mathrm{d}k_c}{(2\pi)^3} k \left(\frac{\partial \epsilon_{\boldsymbol{k}}}{\partial k_a}\right)^2 \delta(\mu - \epsilon_{\boldsymbol{k}}) \tag{4.5}$$

$$= \frac{e^2 E}{v(2\pi)^3}\tau_{\mathrm{tr}} \int_0^{2\pi} \mathrm{d}\phi\pi \left((gB\cos(\phi)+\mu)\Delta\cos^2(\phi) + 2g^2B^2\sin^4(\phi)\sqrt{\frac{(gB\cos(\phi)+\mu)^2}{\Delta^2 - (gB\cos(\phi)+\mu)^2}} \right)$$

$$\approx \frac{e^2 E \pi^2}{v(2\pi)^3}\tau_{\mathrm{tr}}\Delta\mu\left(1 + \frac{3g^2B^2}{2\Delta\sqrt{\Delta^2-\mu^2}}\right), \tag{4.6}$$

where in the last line we have only taken effects up to second order in gB into account. In the experimentally relevant regime of $|B| \lesssim 0.1$ T we have $\frac{g^2B^2}{\Delta\sqrt{\Delta^2-\mu^2}} \ll 1$ for a g-factor $g \approx 20$ in the b-direction [36, 56]. Therefore, the Zeeman contribution to the linear conductivity is almost negligible for our toroidal Fermi surface.

To restore the anisotropic velocities we transform back the integration measure $\mathrm{d}^3k \to \frac{\mathrm{d}^3k}{v_a v_b v_c}$ and all momentum derivatives $\frac{\partial}{\partial k_i} \to v_i \frac{\partial}{\partial k_i}$. With that, we obtain the zero-field conductivity

$$\sigma^{(1)} = \frac{e^2 \tau_{\mathrm{tr}} v_a \Delta\mu}{8\pi\hbar^3 v_b v_c}. \tag{4.7}$$

Using this result we can estimate the transport scattering time by using the experimental value for the reciprocal resistance in zero field $R_0 \approx 8.9$ mΩcm. With the values for Δ and μ from the SdH oscillations from section 3.4 we obtain a scattering time $\tau_{\mathrm{tr}} \approx 57$ fs.

4.1.1 Nonreciprocal response from Zeeman effects

The MCA is quadratic in the electric and linear in the applied magnetic field, therefore we are interested in the conductivity $\sigma^{(2)} \sim E^2 B$ [57]. We will firstly only look at the Zeeman term and later investigate contributions from orbital effects. For this case the distribution function at second order is

$$f^{(2)}(\boldsymbol{k}) = eE\tau_{\mathrm{tr}}\frac{\partial f^{(1)}(\boldsymbol{k})}{\partial k_a} = e^2E^2\tau_{\mathrm{tr}}^2\left(\frac{\partial^2\epsilon_{\boldsymbol{k}}}{\partial k_a^2}\frac{\partial f_0}{\partial \epsilon_{\boldsymbol{k}}} + \left(\frac{\partial \epsilon_{\boldsymbol{k}}}{\partial k_a}\right)^2 \frac{\partial^2 f_0}{\partial \epsilon_{\boldsymbol{k}}^2}\right). \tag{4.8}$$

Using this, we get the corresponding current density for $\mu < \Delta$

$$j_a^{(2)} = -e \int \frac{\mathrm{d}^3 k}{(2\pi)^3} v_a f^{(2)}(\boldsymbol{k}) = e^3 E^2 \tau_{\mathrm{tr}}^2 \int \frac{\mathrm{d}k \mathrm{d}\phi \mathrm{d}k_c}{(2\pi)^3} k \frac{\partial \epsilon_{\boldsymbol{k}}}{\partial k_a} \frac{\partial^2 \epsilon_{\boldsymbol{k}}}{\partial k_a^2} \delta(\mu - \epsilon_{\boldsymbol{k}}) \tag{4.9}$$
$$\approx \frac{3e^3 E^2 g B \tau_{\mathrm{tr}}^2}{128\pi},$$

where the result of the integral was obtained by numerical integration. Restoring the anisotropic velocities and factors of $\hbar$ the second-order conductivity due to Zeeman effects is

$$|\sigma^{(2)}| = |j_a^{(2)}|/E^2 = \frac{3e^3 g B \tau_{\mathrm{tr}}^2 v_a^2}{128\pi\hbar^3 v_b v_c}. \tag{4.10}$$

It should be noted that the size of the nonlinear conductivity does not depend on the parameters Δ and μ, but the sign of the conductivity is set by the sign of Δ, which controls the orientation of the Fermi surface spin texture, as well as the sign of μ distinguishing between electrons or holes as carrier type.

The total current density is given by the sum of first- and second-order contributions $j = \sigma^{(1)} E + \sigma^{(2)} E^2$ and the nonlinear coefficient γ' characterizing the size of the MCA is

$$|\gamma'| = \frac{|\sigma^{(2)}|}{|B| \left(\sigma^{(1)}\right)^2} = \frac{3\hbar^3 \pi g v_b v_c}{2e\Delta^2 \mu^2} = \frac{3g}{8 e v_a \Delta n} \sim 10^{-11}\ \mathrm{m^2 A^{-1} T^{-1}}. \tag{4.11}$$

This coefficient is independent of scattering time and depends only on the Fermi velocity v_a along the direction of the electric field. Furthermore, it diverges for both $\mu \to 0$ as well as $\Delta \to 0$. As we are dealing with a small Fermi surface with low carrier density n nonlinear effects will be large compared to values of γ' found in other materials. On the other hand, our theoretical result is four orders of magnitude smaller than the experimentally observed value and thus the spin texture of the Fermi surface can not be the only explanation for the large MCA in $ZrTe_5$. In the following, we will look at two further mechanisms in the framework of the Boltzmann equation that can lead to an enhancement of γ', namely momentum-dependent scattering rates and nonlinear effects from orbital terms.

4.1.2 Anisotropic scattering

Firstly, we want to investigate contributions due to the anisotropic scattering rate which comes from the spin texture of the Fermi surface. The Zeeman term will lead to an angle dependent relaxation time $\tau_{\mathrm{tr}}(\phi)$ which can give rise to additional terms in the Boltzmann equation. We assume diagonal impurities $U = u_0 \mathbb{1} \otimes \mathbb{1}$ and write the scattering time at the Fermi surface using Fermi's golden rule

$$\frac{1}{\tau_{\boldsymbol{k}}(\mu)} = \int \frac{\mathrm{d}^3k'}{(2\pi)^3} |\langle \boldsymbol{k}'| U |\boldsymbol{k}\rangle|^2 \delta(\epsilon_{\boldsymbol{k}} - \epsilon_{\boldsymbol{k}})\delta(\epsilon_{\boldsymbol{k}'} - \mu) \tag{4.12}$$

$$\approx \frac{n_{\mathrm{imp}} u_0^2}{4} \rho_0(\mu) \left(1 + \frac{gB}{2\mu}\cos(\phi)\right), \tag{4.13}$$

with the impurity density n_{imp} and the zero-field density of states $\rho_0(\mu) = \pi^2 \frac{\partial n}{\partial \mu} = \frac{\Delta\mu}{2\pi\hbar^3 v_a v_b v_c}$. The prefactor 1/4 is due to the averaging of the matrix elements at the Fermi energy. Therefore, the anisotropy in the scattering time linear in the magnetic field due to Zeeman effects can be written as

$$\tau(\phi) \approx \tau_0 \left(1 - \frac{gB}{2\mu}\cos(\phi)\right), \tag{4.14}$$

where τ_0 is the scattering time in the absence of magnetic fields. For the largest experimentally relevant fields of $B \sim 0.1$ T the anisotropic contribution is of the order of 10^{-2} and therefore quite small. As mentioned above, the angle dependence of τ leads to additional terms in the Boltzmann equation and the second-order distribution function becomes

$$\begin{aligned} f^{(2)}(\boldsymbol{k}) &= eE\tau(\phi)\frac{\partial f^{(1)}(\boldsymbol{k})}{\partial k_a} = e^2E^2\tau(\phi)\frac{\partial}{\partial k_a}\left(\tau(\phi)\frac{\partial f_0}{\partial k_a}\right) \\ &= e^2E^2\tau(\phi)\left(\tau(\phi)\left(\frac{\partial^2\epsilon_{\boldsymbol{k}}}{\partial k_a^2}\frac{\partial f_0}{\partial \epsilon_{\boldsymbol{k}}} + \left(\frac{\partial \epsilon_{\boldsymbol{k}}}{\partial k_a}\right)^2 \frac{\partial^2 f_0}{\partial \epsilon_{\boldsymbol{k}}^2}\right) + \frac{\partial \tau(\phi)}{\partial k_a}\frac{\partial \epsilon_{\boldsymbol{k}}}{\partial k_a}\frac{\partial f_0}{\partial \epsilon_{\boldsymbol{k}}}\right). \end{aligned} \tag{4.15}$$

It turns out that the conductivity for anisotropic scattering is about a factor three larger than the result for the deformation of the Fermi surface with

$$|\sigma_\tau^{(2)}| \approx \frac{9e^3 gB\tau_0^2 v_a^2}{128\pi\hbar^3 v_b v_c}. \tag{4.16}$$

Therefore, this effect needs to be taken into account to capture the nonlinear transport properties of our model correctly but it is not enough to explain the giant MCA observed in $ZrTe_5$.

4.1.3 MCA from orbital effects

We have seen that purely from the Zeeman effect, we can not obtain a MCA of similar magnitude as in the experiment. Another candidate for a possible mechanism are orbital effects arising from $\boldsymbol{v_k} \times \boldsymbol{B}$ in the Boltzmann equation. An expansion of these contributions to the distribution function can be written in powers of $\omega_c\tau$ with the cyclotron frequency $\omega_c \sim B$. For clean systems with large scattering times the magnetoresistance from orbital effects is expected to be much greater than contributions due to the Zeeman term. In

the following, we will write the distribution function as $f = f_0 + f_1 + f_2 + f_3 + ...$ where the subscript i now indicates the combined powers of electric and magnetic field, e.g. f_3 contains terms $\sim EB^2$ and $\sim E^2B$ which will contribute to the first- and second-order conductivity, respectively. The Boltzmann equation to order i reads

$$e\boldsymbol{E}\frac{\partial f_{i-1}(\boldsymbol{k})}{\partial \boldsymbol{k}} + e\left(\boldsymbol{v}_k \times \boldsymbol{B}\right)\frac{\partial f_{i-1}(\boldsymbol{k})}{\partial \boldsymbol{k}} = \frac{f_i(\boldsymbol{k})}{\tau_{\mathrm{tr}}}. \tag{4.17}$$

For an electric field $\boldsymbol{E} = E\hat{a}$ and the magnetic field pointing in b-direction with $\boldsymbol{B} = B\hat{b}$ the recursion formula determining the next highest order is

$$f_i(\boldsymbol{k}) = e\tau_{\mathrm{tr}}\left(E\frac{\partial}{\partial k_a} + B\left[\frac{\partial \epsilon_{\boldsymbol{k}}}{\partial k_a}\frac{\partial}{\partial k_c} - \frac{\partial \epsilon_{\boldsymbol{k}}}{\partial k_c}\frac{\partial}{\partial k_a}\right]\right) f_{i-1}(\boldsymbol{k}). \tag{4.18}$$

Previously, we have already shown in (4.3) that f_1 does not contain any terms $\sim B$ as the relevant derivatives cancel out. Going to the next order we obtain

$$f_2(\boldsymbol{k}) = e^2\tau_{\mathrm{tr}}^2E^2\left(\frac{\partial^2\epsilon_{\boldsymbol{k}}}{\partial k_a^2}\frac{\partial f_0}{\partial \epsilon_{\boldsymbol{k}}} + \left(\frac{\partial \epsilon_{\boldsymbol{k}}}{\partial k_a}\right)^2\frac{\partial^2 f_0}{\partial \epsilon_{\boldsymbol{k}}^2}\right) + e^2\tau_{\mathrm{tr}}^2EB\left(\frac{\partial \epsilon_{\boldsymbol{k}}}{\partial k_a}\frac{\partial^2\epsilon_{\boldsymbol{k}}}{\partial k_c \partial k_a} - \frac{\partial \epsilon_{\boldsymbol{k}}}{\partial k_c}\frac{\partial^2\epsilon_{\boldsymbol{k}}}{\partial k_a^2}\right)\frac{\partial f_0}{\partial \epsilon_{\boldsymbol{k}}}, \tag{4.19}$$

where the term $\sim EB$ will give rise to the usual Hall effect with $\boldsymbol{j} \perp \boldsymbol{E} \perp \boldsymbol{B}$. As we are, for now, only interested in the longitudinal transport with $\boldsymbol{j} \parallel \boldsymbol{E}$ this term does not contribute to the conductivity. Corrections to the first- and second-order conductivity will arise when looking at f_3. Firstly, we consider the linear current $j^{(1)} \sim EB^2$ where the relevant distribution function is given by

$$\begin{aligned} f_3^{(1)}(\boldsymbol{k}) &= e\tau_{\mathrm{tr}}B\left[\frac{\partial \epsilon_{\boldsymbol{k}}}{\partial k_a}\frac{\partial}{\partial k_c} - \frac{\partial \epsilon_{\boldsymbol{k}}}{\partial k_c}\frac{\partial}{\partial k_a}\right]\left(e^2\tau_{\mathrm{tr}}^2EB\left(\frac{\partial \epsilon_{\boldsymbol{k}}}{\partial k_a}\frac{\partial^2\epsilon_{\boldsymbol{k}}}{\partial k_a \partial k_c} - \frac{\partial \epsilon_{\boldsymbol{k}}}{\partial k_c}\frac{\partial^2\epsilon_{\boldsymbol{k}}}{\partial k_a^2}\right)\frac{\partial f_0}{\partial \epsilon_{\boldsymbol{k}}}\right) \\ &= e^3\tau_{\mathrm{tr}}^3EB^2\left(\left(\frac{\partial \epsilon_{\boldsymbol{k}}}{\partial k_c}\right)^2\frac{\partial^3\epsilon_{\boldsymbol{k}}}{\partial k_a^3} - 2\frac{\partial \epsilon_{\boldsymbol{k}}}{\partial k_a}\frac{\partial \epsilon_{\boldsymbol{k}}}{\partial k_c}\frac{\partial^3\epsilon_{\boldsymbol{k}}}{\partial k_a^2 \partial k_c} - \frac{\partial \epsilon_{\boldsymbol{k}}}{\partial k_a}\frac{\partial^2\epsilon_{\boldsymbol{k}}}{\partial k_a^2}\frac{\partial^2\epsilon_{\boldsymbol{k}}}{\partial k_c^2}\right. \\ &\qquad \left. + \frac{\partial \epsilon_{\boldsymbol{k}}}{\partial k_a}\left(\frac{\partial^2\epsilon_{\boldsymbol{k}}}{\partial k_a \partial k_c}\right)^2 + \left(\frac{\partial \epsilon_{\boldsymbol{k}}}{\partial k_a}\right)^2\frac{\partial^3\epsilon_{\boldsymbol{k}}}{\partial k_a \partial k_c^2}\right)\frac{\partial f_0}{\partial \epsilon_{\boldsymbol{k}}}. \end{aligned} \tag{4.20}$$

This results in an orbital contribution to the current linear in electric field

$$j_{a,\mathrm{orb}}^{(1)} = -e\int\frac{\mathrm{d}^3k}{(2\pi)^3}\frac{\partial \epsilon_{\boldsymbol{k}}}{\partial k_a}f_3^{(1)}(\boldsymbol{k}) = \frac{3e^4\tau_{\mathrm{tr}}^3v_a^3v_cEB^2}{2^4\pi v_b\mu^3}\Delta\left(\Delta\sqrt{\Delta^2-\mu^2} - \Delta^2\right). \tag{4.21}$$

In the limit $\mu \ll \Delta$ the conductivity quadratic in the magnetic field is therefore

$$\sigma_{aa}^{(1)} \approx \frac{e^2\tau_{\mathrm{tr}}v_a\Delta\mu}{8\pi\hbar^3v_bv_c} - \frac{3e^4\tau_{\mathrm{tr}}^3v_a^3v_cB^2}{2^5\pi\hbar^3v_b\mu}\Delta, \tag{4.22}$$

where we have ignored the much smaller contribution from the Zeeman term.

A possible source of nonreciprocal transport and the MCA are terms in $f_3^{(2)} \sim E^2 B$ which take the form

$$f_3^{(2)}(\boldsymbol{k}) = e^3 \tau_{\mathrm{tr}}^3 E^2 B \left[\frac{\partial}{\partial k_a} \left(\left(\frac{\partial \epsilon_{\boldsymbol{k}}}{\partial k_a} \frac{\partial^2 \epsilon_{\boldsymbol{k}}}{\partial k_a \partial k_c} - \frac{\partial \epsilon_{\boldsymbol{k}}}{\partial k_c} \frac{\partial^2 \epsilon_{\boldsymbol{k}}}{\partial k_a^2} \right) \frac{\partial f_0}{\partial \epsilon_{\boldsymbol{k}}} \right) \right. \\ \left. + \left(\frac{\partial \epsilon_{\boldsymbol{k}}}{\partial k_a} \frac{\partial}{\partial k_c} - \frac{\partial \epsilon_{\boldsymbol{k}}}{\partial k_c} \frac{\partial}{\partial k_a} \right) \left(\frac{\partial^2 \epsilon_{\boldsymbol{k}}}{\partial k_a^2} \frac{\partial f_0}{\partial \epsilon_{\boldsymbol{k}}} + \left(\frac{\partial \epsilon_{\boldsymbol{k}}}{\partial k_a} \right)^2 \frac{\partial^2 f_0}{\partial \epsilon_{\boldsymbol{k}}^2} \right) \right], \tag{4.23}$$

which will lead to a nonlinear current from orbital effects

$$j_{a,\mathrm{orb}}^{(2)} = e^4 \tau_{\mathrm{tr}}^3 E^2 B I^{(2)}, \tag{4.24}$$

with the integral

$$I^{(2)} = \int \frac{\mathrm{d}^3 k}{(2\pi)^3} \left(\frac{\partial \epsilon_{\boldsymbol{k}}}{\partial k_a} \left(\frac{\partial \epsilon_{\boldsymbol{k}}}{\partial k_c} \frac{\partial^3 \epsilon_{\boldsymbol{k}}}{\partial k_a^3} - \frac{\partial \epsilon_{\boldsymbol{k}}}{\partial k_a} \frac{\partial^3 \epsilon_{\boldsymbol{k}}}{\partial k_a^2 \partial k_c} - 3 \frac{\partial^2 \epsilon_{\boldsymbol{k}}}{\partial k_a^2} \frac{\partial^2 \epsilon_{\boldsymbol{k}}}{\partial k_a \partial k_c} \right) + 3 \frac{\partial \epsilon_{\boldsymbol{k}}}{\partial k_c} \left(\frac{\partial^2 \epsilon_{\boldsymbol{k}}}{\partial k_a^2} \right)^2 \right) \frac{\partial f_0}{\partial \epsilon_{\boldsymbol{k}}}.$$

As we are interested in the current linear in magnetic field the relevant band structure $\epsilon_{\boldsymbol{k}}$ is that of the nodal line system in the absence of a magnetic field given by Eq. (3.8). In this case, we have time-reversal symmetry $\epsilon_{-\boldsymbol{k}} = \epsilon_{\boldsymbol{k}}$. Each term in the integral $I^{(2)}$ contains an odd number of momentum derivatives. Therefore, if we use the transformation $\boldsymbol{k} \to -\boldsymbol{k}$, we obtain $I^{(2)} = -I^{(2)} = 0$ and $j_{a,\mathrm{orb}}^{(2)}$ has to be zero by symmetry. This result holds beyond the relaxation-time approximation as long as we have a time-reversal invariant scattering matrix with $M_{\boldsymbol{k},\boldsymbol{k}'} = M_{-\boldsymbol{k}',-\boldsymbol{k}}$. That means that at least in the framework of the Boltzmann equation orbital effects do not contribute to the MCA. As this calculation is exact up to leading order in τ there can be no conductivity $\sigma^{(2)} \sim \tau^3$. If we consider quantum effects which go beyond the Boltzmann equation, the resulting nonlinear current would be of subleading power $\sim \tau^4$.

4.1.4 Reciprocal conductivity tensor and Hall angles

Before we consider another possible mechanism for the enhancement of the nonreciprocal transport that goes beyond the Boltzmann equation, we first want to complete the description of the linear response. As $ZrTe_5$ is a highly anisotropic 3d material, the resistance will vary greatly for different directions. We will find that if the external current is applied along an axis with low Fermi velocity the electrons will flow almost exclusively in perpendicular diraction. This behavior can be characterized by a large Hall angle between the electric field and the resulting current.

As the magnetic field in the experimental setup points along the b-direction, the only finite Hall response should be $\sigma_{ac} = -\sigma_{ca}$. Using $f_2(\boldsymbol{k})$ from Eq. (4.19) we obtain

$$\sigma_{ca} = \frac{j_c}{E_a} = -\frac{e}{E}\int \frac{\mathrm{d}^3k}{(2\pi)^3}\frac{\partial \epsilon_{\boldsymbol{k}}}{\partial k_c} f_2(\boldsymbol{k}) = \frac{e^3\tau_{\mathrm{tr}}^2 v_a v_c \Delta}{8\pi\hbar^3 v_b} B. \tag{4.25}$$

It should be noted that recent experiments also report a parallel-field Hall effect with $\boldsymbol{j_H} \perp \boldsymbol{B} \parallel \boldsymbol{E}$ in $ZrTe_5$ [52]. As this phenomenon requires additional symmetries to be broken we will not consider it here but instead investigate it in chapter 6. The reciprocal conductivity tensor in the ac-plane therefore is given by

$$\sigma = \begin{pmatrix} \sigma_{aa} & \sigma_{ac} \\ \sigma_{ca} & \sigma_{cc} \end{pmatrix} = \begin{pmatrix} \frac{e^2\tau_{\mathrm{tr}} v_a \Delta\mu}{8\pi\hbar^3 v_b v_c} - \frac{3e^4\tau_{\mathrm{tr}}^3 v_a^3 v_c \Delta}{2^5\pi\hbar^3 v_b \mu} B^2 & -\frac{e^3\tau_{\mathrm{tr}}^2 v_a v_c \Delta}{8\pi\hbar^3 v_b} B \\ \frac{e^3\tau_{\mathrm{tr}}^2 v_a v_c \Delta}{8\pi\hbar^3 v_b} B & \frac{e^2\tau_{\mathrm{tr}} v_c \Delta\mu}{4\pi\hbar^3 v_a v_b} - \frac{e^4\tau_{\mathrm{tr}}^3 v_c^3 v_a \Delta}{8\pi\hbar^3 v_b \mu} B^2 \end{pmatrix}. \tag{4.26}$$

The conductivity σ_{cc} has slightly different numerical prefactors as this is the direction perpendicular to the torus plane and therefore the band structure is different. σ_{bb} on the other hand can be obtained directly from σ_{aa} by exchanging $v_a \leftrightarrow v_b$ due to the rotational symmetry in the torus plane. For our model orbital terms will not lead to a longitudinal conductivity $\sim B^2$ in the b-direction as we have $\boldsymbol{E} \parallel \boldsymbol{B}$. Therefore, in this direction we expect a much smaller magnetoresistance only governed by the Zeeman effect.

A useful quantity to characterize the direction of the resulting current relative to the applied electric field is the Hall angle α defined by

$$\cos(\alpha_{\mathrm{Hall}}) = \frac{\boldsymbol{j}\cdot\boldsymbol{E}}{|\boldsymbol{j}|\cdot|\boldsymbol{E}|}. \tag{4.27}$$

For an electric field in a-direction we have $\boldsymbol{j} = \begin{pmatrix} \sigma_{aa} \\ \sigma_{ca} \end{pmatrix} E$ and therefore the Hall angle is given by

$$\alpha_{\mathrm{Hall}}^{(a)} = \arccos\left(\frac{\sigma_{aa}}{\sqrt{\sigma_{aa}^2 + \sigma_{ca}^2}}\right). \tag{4.28}$$

As the longitudinal conductivity σ_{ii} is symmetric in B the current component along the applied field will not change under $B \to -B$. The Hall conductivity on the other hand is linear in magnetic field and therefore the current perpendicular to $\boldsymbol{E}$ will change sign when B is reversed. This can be seen in Fig. 4.1 a) for two different orientations of electric field. To account for this behavior one can define the Hall angle such that it also changes sign under $B \to -B$. In this case we have

$$\alpha_{\mathrm{Hall}}^{(a)} = \arctan\left(\frac{\sigma_{ca}}{\sigma_{aa}}\right) \tag{4.29}$$

or

$$\alpha_{\mathrm{Hall}}^{(c)} = \arctan\left(\frac{\sigma_{ac}}{\sigma_{cc}}\right) \tag{4.30}$$

for $\boldsymbol{E} = E\hat{c}$.

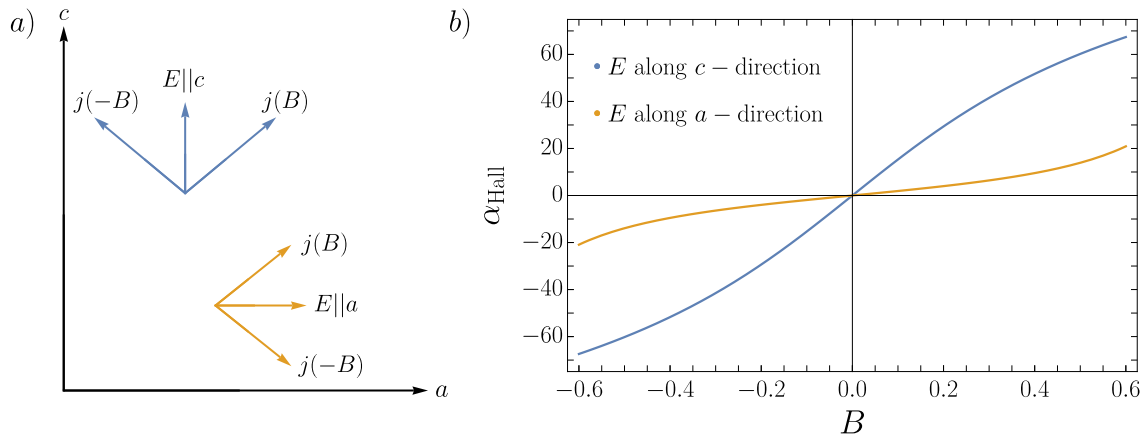

Figure 4.1: a) Illustration of the Hall angles in the ac-plane and a magnetic field along the b-direction. The current component perpendicular to the electric field changes sign when the direction of B is reversed. b) Hall angles as a function of magnetic field for the two electric field orientations. In the direction of smaller Fermi velocity large Hall angles can be achieved at small magnetic fields. As shown in the illustration the Hall angle changes sign when $B \to -B$.

The two Hall angles as a function of magnetic field are shown in Fig. 4.1 b). As v_a is the largest Fermi velocity in $ZrTe_5$, Hall angles in this direction are small and the current mostly flows along the applied field. In the c-direction, where the Fermi velocity is about a factor 4 smaller than along the a-axis, Hall angles of up to 60° can be reached already at small fields $B = 0.6$ T. Here, a substantial part of the current flows perpendicular to the electric field. Even larger Hall angles could be observed when the magnetic field is applied along the c-axis and the electric field is in the direction of the lowest Fermi velocity $v_b \approx v_a/16$. In this setup, Hall angles of almost 90° can be achieved at small fields meaning that the electrons flow almost perpendicular to the direction of the applied voltage. The existence of large Hall angles is not a property of the nodal line system but can be traced back to the anisotropic velocities in our system. The same results can be obtained for a Weyl point with linear dispersion $\epsilon_{\text{lin}} = \hbar\sqrt{v_x^2k_x^2 + v_y^2k_y^2 + v_z^2k_z^2}$ and anisotropic velocities v_i or even for a quadratic dispersion $\epsilon_{\text{quad}} = \frac{\hbar^2k_x^2}{2m_x} + \frac{\hbar^2k_y^2}{2m_y} + \frac{\hbar^2k_z^2}{2m_z}$ with anisotropic band masses m_i. In the case of such a Schrödinger-like system each momentum k_i needs to be rescaled by $\sqrt{m_i}$ to map the Hamiltonian to an isotropic one.

4.2 Charge density modulations

As mentioned previously, $ZrTe_5$ samples which show large nonreciprocal transport coefficients have small charge densities $n \approx 10^{16}$ cm^{-3} as computed via Eq. (3.7) from quantum oscillation data. Therefore, screening effects in our system are expected to be small and charged impurities can lead to the formation of large-scale inhomogeneities in the electron density. These can be described by a space-dependent chemical potential

$\mu(\boldsymbol{r})$. In compensation-doped topological insulators a similar phenomenon takes place where due to Coulomb disorder conducting regions, so-called puddles, form inside the otherwise insulating bulk. As we are dealing with a metallic system there is no clear separation of insulating and conducting parts of our system. Still, we will refer to regions of low density, and therefore large resistivity, as "puddles" in $ZrTe_5$.

Comparing the scattering times obtained from quantum oscillations as well as from transport measurements yields strong experimental evidence for an inhomogeneous system. The scattering time $\tau_D = 500$ fs obtained from Dingle damping is about one order of magnitude larger than the transport scattering time $\tau_{\mathrm{tr}} \approx 57$ fs, which was fitted to the reciprocal resistance at zero field. Usually, the transport scattering time is larger than the decay time of quantum oscillations as small-angle scattering does not contribute to the decay of currents, see Eq. (2.23). Therefore, $\tau_{\mathrm{tr}} \ll \tau_D$ is quite noteworthy and indicates that the resistivity is governed by the physics of badly conducting regions in a system with varying charge density. Due to the velocity anisotropy, $v_b \ll v_c < v_a$, these regions also will not be short-circuited but instead the transport becomes almost one-dimensional and currents are forced through low density puddles. In the following chapter 4.3 we obtain numerical confirmation of this phenomenon using a resistor network model.

In such a setting where the transport is almost unidirectional we can model the chemical potential to only vary along the direction of the applied current $\mu = \mu(x)$. This leads to space-dependent conductivities and locally varying electric fields with

$$j = \sigma^{(1)}(x)E(x) + \sigma^{(2)}(x)E(x)^2. \tag{4.31}$$

In this case, the nonreciprocal coefficient for the inhomogeneous system is

$$\gamma'_{\mathrm{in}} = -\frac{\int \frac{\sigma^{(2)}(x)}{B(\sigma^{(1)}(x))^3}\mathrm{d}x}{\int \frac{1}{\sigma^{(1)}(x)}\mathrm{d}x}. \tag{4.32}$$

From Eq. (4.7) and (4.10) we know that $\sigma^{(1)}$ is linear in $|\mu|$ while $\sigma^{(2)}$ is independent of the chemical potential for $\mu < \Delta$. Therefore, the enhancement from a spatially varying chemical potential can be estimated via

$$\gamma'_{\mathrm{in}} = -\frac{\int (\frac{\bar{\mu}}{\mu(x)})^3\mathrm{d}x}{\int \frac{\bar{\mu}}{|\mu(x)|}\mathrm{d}x}\gamma', \tag{4.33}$$

where $\bar{\mu}$ is the average chemical potential and γ' is the nonlinear coefficient of the homogeneous system. This enhancement factor is highly divergent for $\mu \to 0$ due to the $1/\mu(x)^3$ integration in the numerator. Hence, large-scale inhomogeneities in the electron density can lead to a significant enhancement of the nonlinear properties of a material

compared to the homogeneous setting. Additional mechanisms like an energy-dependent scattering time or the three-dimensional nature of our samples will regularize this divergence and therefore Eq. (4.33) can not be used to obtain a quantitative estimate. Additionally, in a system with spatially varying density the formation of local p-n junctions can take place. These can further enhance the nonlinear properties by enhancing the local electric fields.

4.3 Resistor networks

The previous arguments that a locally varying charge density can lead to an enhancement of the MCA relies on transport being dominated by low density regions. Here, local electric fields can be greatly amplified and lead to large nonlinear effects. In a three-dimensional sample, these regions could naively just be short-circuited via currents flowing around these "puddles" through better conducting regions. Using a resistor network model, we study the current flow through a medium with space-dependent conductivities as a function of resistivity anisotropy. For that we set up a rectangular lattice of size $L_x \times L_y$ and define a voltage V_i at each lattice site i. On each bond between two sites we place a linear resistor, where we distinguish x- and y-bonds as shown in Fig. 4.2. The currents through these resistors also live on the bonds and are given by:

$$I_x(i,j) = \sigma_{xx}(i,j)\Delta V(i,j), \tag{4.34}$$

$$I_y(i,j) = \sigma_{yy}(i,j)\Delta V(i,j), \tag{4.35}$$

where $\sigma_{xx}(i,j), \sigma_{yy}(i,j)$ are the local conductivities of the resistors and $\Delta V(i,j) = V_j - V_i$ is the voltage drop at a resistor. Here, we focus on the transport in the absence of magnetic fields and therefore ignore Hall effects, which would require a modified model with four-terminal resistors. To solve these equations, we need to impose current conservation at each node i which can be written as

$$\sum_{k=1}^{4} I_i^{(k)} = -I_x(i,i+1) + I_x(i-1,i) - I_y(i,i+L_x) + I_y(i-L_x,i) = 0. \tag{4.36}$$

Each of these equations connects the voltage at one site with the voltages on their four neighboring sites (see Fig. 4.2). As a boundary condition we apply a finite external voltage difference V_0 across the whole system and thus fix all voltages on sites with $x = 0$ to have $V = 0$ and sites with $x = L_x$ at $V = V_0$. Thus we are left with $(L_x-2)\cdot L_y$ unknown voltages and the same number of equations through Eq. (4.36). Combining all these equations into

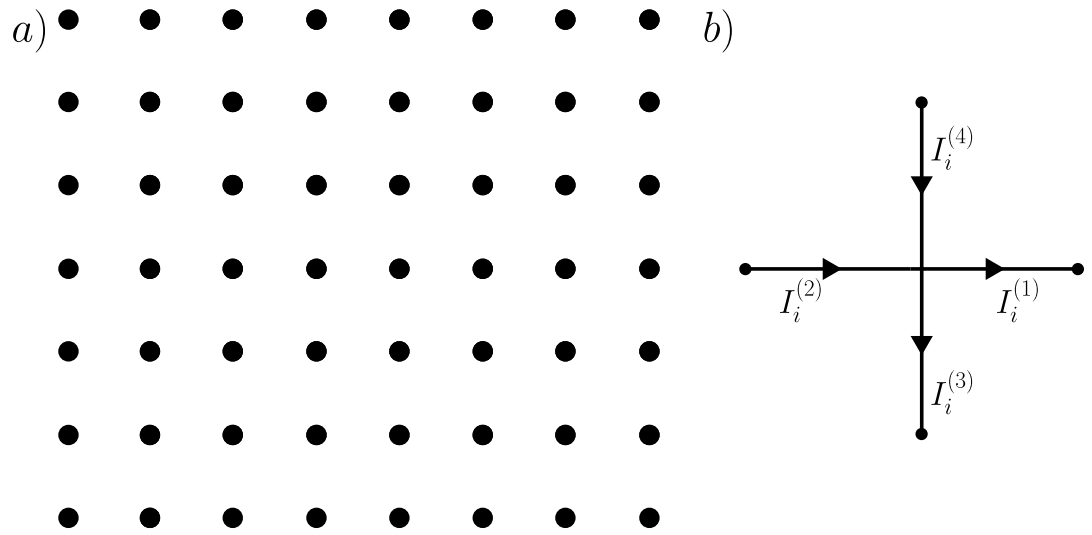

Figure 4.2: a) 2d resistor network. At each node we define a voltage V_i. Neighboring sites are connected via linear resistors in x- and y-direction. b) Current conservation at a single node i. Incoming and outgoing currents have to be equal.

a matrix equation we can easily obtain the solution by matrix inversion

$$G \cdot (\mathbf{V} + \mathbf{V_0}) = 0 \quad \Rightarrow \quad \mathbf{V} = -G^{-1} \cdot \mathbf{V_0}. \tag{4.37}$$

Here, G is the matrix of conductivities, the vector $\mathbf{V}$ contains all unknown voltages and $\mathbf{V_0}$ is the vector of boundary conditions. Each row of the conductivity matrix contains at most five non-zero entries as the current conservation at each node only cares about the nearest neighbors. Thus, we are dealing with a sparse matrix allowing us to solve large systems with up to $L_x = 400$ via exact diagonalization. Now, we want to consider a system with inhomogeneous density profile. The local conductivities will be chosen such that the anisotropy

$$\alpha(i,j) = \frac{\sigma_{yy}(i,j)}{\sigma_{xx}(i,j)} \tag{4.38}$$

is constant in space. To create a disorder configuration, we sum up randomly positioned Gaussians leading to a density profile $n(\mathbf{x}) \sim \sum_i \exp\left(\frac{(\mathbf{x}-\mathbf{x_i})^2}{2\sigma_i^2}\right)$ where the peak locations $\mathbf{x_i}$ and the width σ_i are randomly distributed. To simplify our model further we restrict it to just distinguish between two regions A,B. Therefore, we chose a cutoff n_0 such that all points with $n(\mathbf{x}) \leq n_0$ are part of region A while region B consists of all sites with $n(\mathbf{x}) > n_0$. The parameter n_0 will be chosen such that region A of the resulting configuration has a volume fraction p with $0 < p < 1$. The conductivities in the two regions are labeled by $\sigma_{ii}^A, \sigma_{ii}^B$. One example of such a disorder realization for $p = 0.85$ and $\sigma_{xx}^A = 10\sigma_{xx}^B$ can be seen in Fig. 4.3 a). Using this configuration in our conductivity matrix, we can solve Eq. (4.37) to obtain the voltage profile and current distribution. The result will greatly depend on the anisotropy (4.38) as can be seen in Fig. 4.3 b,c).

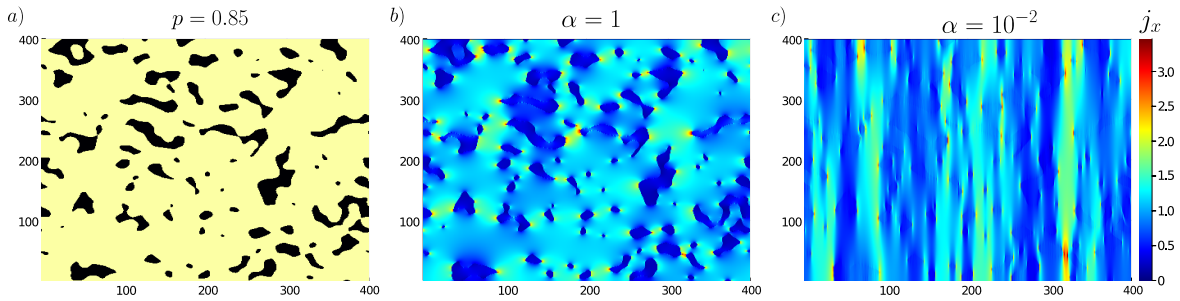

Figure 4.3: a) Disorder configuration for a 400×400 system with volume fraction $p = 0.85$ of region A and $\sigma^A_{xx} = 10\sigma^B_{xx}$. b,c) Current patterns for different anisotropies $\alpha = 1$ and $\alpha = 10^{-2}$. If there is no anisotropy currents can flow around badly conducting regions. For a highly anisotropic system the transport becomes almost one-dimensional and the current is forced through regions of low density.

If the conductivities in both directions are equal ($\alpha = 1$) the current flows around the badly conducting regions with low density. In a system with larger conductivity in the x-direction (e.g. $\alpha = 10^{-2}$) the transport becomes almost one-dimensional along the direction with higher conductivity. Here, the electron flow around obstacles is suppressed and the current goes through badly conducting regions. As the experimental system has an anisotropy of $\alpha \approx 1/13$ in the ac-plane and $\alpha \approx 1/200$ in the ab-plane, this scenario for the current density seems reasonable. Even though we have used a 2d model the clear hierarchy of Fermi velocities in $ZrTe_5$ supports the picture of quasi one-dimensional transport. Therefore, low density regions will contribute to the transport in our system and can lead to an enhancement of nonlinear effects. Dividing the system into two distinct regions with a sudden jump in conductivity is, of course, a simplification of the realistic density distribution in the experimental system. Instead, one can use the results from the Boltzmann equation for the conductivity tensor $\sigma(n)$ from Eq. (4.26) as a function of density $n = \bar{n} + \delta n$. Here, $\bar{n} = \frac{\Delta\bar{\mu}^2}{4\pi^3\hbar^3 v_a v_b v_c}$ is the average charge density for a mean chemical potential $\bar{\mu}$ and δn are random density fluctuations with $\langle \delta n \rangle = 0$. For such a density profile one obtains qualitatively the same current profiles as in our toy model above. As the screening of charges is a non-local problem due to the long-ranged Coulomb interactions describing the microscopic formation of an inhomogeneous density distribution is a hard task and not within the scope of this thesis.

5 Nonohmic transport

Motivated by a different set of transport experiments where the applied current and magnetic field are parallel to each other and along the crystallographic a-axis, meaning $\mathbf{I} \parallel \mathbf{B} \parallel \hat{a}$, we investigate our model for $ZrTe_5$ in a magnetic field parallel to the nodal line plane. As we are working with a 3d material, the momentum along the magnetic field will not be restricted while wavefunctions along the other two momentum directions will get quantized into Landau orbits. In this setup, the measurements do not need to consider any Hall effects and we can just focus on the longitudinal transport. Furthermore, responses with even powers in electric fields are symmetry-forbidden and the resulting current will be of the form $j = \sigma_1 E + \sigma_3 E^3 + \sigma_5 E^5 + ...$ with the conductivities σ_i. We will refer to the higher-order conductivities as **nonohmic**, as they go beyond what is predicted by Ohm's law. To characterize the size of nonohmic transport effects, we use the coefficient $\gamma_3 = \sigma_3/(\sigma_1)^3$ which, similar to γ_2 from the previous chapter, will not depend on the scattering time τ and can thus be used to compare the nonlinear transport properties of different systems. Additionally, the scattering rate can drastically change as a function of magnetic field, which can be ignored when considering $\gamma_3(B)$. Experimentally, a large increase of the nonohmic coefficient as a function of magnetic field is observed. Once the system reaches the quantum limit, the nonlinearity saturates.
We first will compute the nonohmic coefficient γ_3 in the absence of a magnetic field and set up the theory to describe our nodal line system and its transport properties in a magnetic field. Of central importance will be the lowest Landau level which in our model has a very small bandwidth and sits close to zero energy [58]. Afterwards, we will compare our results to the experimental system and explore possible additional mechanisms present in real samples going beyond our model. Here, more involved calculations are performed in certain limits to validate the approximations which were used. At the end of this chapter, we will use the previously developed techniques to investigate the transport properties of a system without broken mirror symmetries and see how the nonohmic coefficient can be used to distinguish different types of linear band crossings.
This chapter is based on the publication 2: "Nonlinear Transport due to Magnetic-Field-Induced Flat Bands in the Nodal-Line Semimetal $ZrTe_5$" Phys. Rev. Lett. 131, 146602 (2023) and its supplementary material [59].

5.1 Nonohmic coefficient without a magnetic field

We will start by determining the nonohmic coefficient γ_3 in the absence of a magnetic field. This will be an extension of the calculation in chapter 4.1 as the nonlinear term we

need to consider here is proportional to the third power of the applied electric field. The linear conductivity for an electric field applied in a-direction was already computed, see Eq. (4.7), and is given by

$$\sigma_1^{(aa)} = \frac{e^2 \tau \mu \Delta v_a}{8\pi\hbar^3 v_b v_c}. \tag{5.1}$$

Proceeding with the perturbation expansion in powers of E we obtain the third-order current as an integral over the third derivative of the dispersion

$$j_3^{(a)} = \frac{e^4}{\hbar^4}\tau^3 E^3 \int \frac{\mathrm{d}k_r \mathrm{d}k_c \mathrm{d}\phi}{(2\pi)^3} k_r \frac{\partial \epsilon_{\mathbf{k}}}{\partial k_a} \frac{\partial^3 \epsilon_{\mathbf{k}}}{\partial k_a^3} \delta(\epsilon_{\mathbf{k}} - \mu) = \sigma_3^{(aa)} E^3. \tag{5.2}$$

Performing the integral yields

$$\Rightarrow \sigma_3^{(aa)} = \frac{3e^4\tau^3 v_a^3}{128\pi\hbar^3 v_b v_c} \frac{\Delta}{\mu} \left(5 - \frac{8\Delta}{\sqrt{\Delta^2 - \mu^2}}\right). \tag{5.3}$$

To compare to the experimental result we compute the nonohmic coefficient γ_3 which cancels out the unknown transport scattering time τ

$$\gamma_3 = \frac{\sigma_3^{(aa)}}{(\sigma_1^{(aa)})^3} = \frac{12\pi^2\hbar^6 v_b^2 v_c^2}{e^2\Delta^2\mu^4} \left(5 - \frac{8\Delta}{\sqrt{\Delta^2 - \mu^2}}\right). \tag{5.4}$$

We can also express the nonohmic coefficient as a function of carrier density. As we already know, the total charge is determined by an integral over the Fermi volume

$$n(\mu) = \frac{\Delta\mu^2}{4\pi\hbar^3 v_a v_b v_c}. \tag{5.5}$$

This expression is only true for $n \leq n_c$ with $n_c = n(\mu = \Delta)$ being the critical density at which the system is no longer described by a torus Fermi surface. Inserting this relation into Eq. (5.4) gives us

$$\gamma_3(B=0) = \frac{3}{4e^2 v_a^2} \left(\frac{3}{n^2} + 16\pi \frac{\hbar^3 v_a v_b v_c}{\Delta^3 n}\right) = \frac{3}{4e^2 v_a^2} \left(\frac{3}{n^2} + \frac{4}{n_c n}\right). \tag{5.6}$$

The first term will be dominant for small densities $n < n_c$ which is the regime where the experiments take place. Using experimental parameters from chapter 3.4 and assuming a density $n = 10^{22}$ m^{-3}, we obtain $\gamma_3(B=0) = 2.1 \cdot 10^{-18}$ m^4/A^2. This value is much smaller than the experimentally obtained coefficient. We will discuss this discrepancy in section 5.6.2.

Calculating the same coefficient for a Dirac system with a linear dispersion $\epsilon_{\mathbf{k}} = \sqrt{v_a k_a + v_b k_b + v_c k_c}$ gives a similar expression to the first term of the nodal line semimetal

$$\gamma_3^{(\mathrm{Dirac})}(B=0) = \frac{6}{5e^2 v_a^2 n^2}. \tag{5.7}$$

5.2 Landau levels in 3d Dirac systems

In this section we will focus on 3d Dirac systems in a magnetic field. Previously, we have included the effects of the magnetic field only via a Zeeman coupling in the Hamiltonian and a force term in the Boltzmann equation $\sim \vec{v} \times \vec{B}$. This works well in the limit of small magnetic fields meaning $\omega_c \tau \ll 1$ where ω_c is the cyclotron frequency and τ is the scattering time which will also be magnetic field dependent. A proper description includes orbital effects also on the level of the Hamiltonian, leading to quantization perpendicular to the magnetic field.

In 3 spatial dimensions, we can always choose one momentum direction along the applied field and two perpendicular directions, where the wavefunctions will form quantized Landau levels (LL). This leaves us with quasi-1d states that can still be broadened by disorder. Let us first consider a single linear crossing for which the Hamiltonian is given by:

$$H = v_F \vec{\sigma} \cdot \vec{k}. \tag{5.8}$$

We have previously seen in section 1.3.1 that, depending on inversion and time-reversal symmetry, such a crossing of two bands can not exist without at least one partner at a different point in momentum space. For now we are only interested in the properties near a single crossing and assume that these points are far enough apart.

The magnetic field can be defined as $\vec{B} = \nabla \times \vec{A}$. The vector potential $\vec{A}$ then enters into our Hamiltonian (5.8) via minimal coupling to the momentum $\vec{k} \mapsto \vec{k} - e\vec{A}$. There is still some gauge freedom in the choice of the vector potential. If we want the magnetic field to be along the z-axis a simple choice would be $\vec{A} = By\vec{e}_x$ leading to $\vec{B} = B\vec{e}_z$. In this case the Hamilton operator becomes:

$$H = v_F \left(\sigma_x(k_x - eBy) + \sigma_y k_y + \sigma_z k_z\right). \tag{5.9}$$

To solve this Hamiltonian we introduce ladder operators $\hat{a}$ and $\hat{a}^\dagger$ such that they obey the same commutation relations as for the harmonic oscillator $[\hat{a}, \hat{a}^\dagger] = 1$. Here, we can write $\hat{a} = \frac{l_B}{\sqrt{2}}(k_x - eBy - ik_y)$ with the magnetic length $l_B = 1/\sqrt{eB}$. With these new operators the Hamiltonian can be compactly written in matrix form as

$$H = \begin{pmatrix} v_F k_z & \Omega_c \hat{a} \\ \Omega_c \hat{a}^\dagger & -v_F k_z \end{pmatrix}, \tag{5.10}$$

with the cyclotron energy $\Omega_c = \frac{\sqrt{2} v_F}{l_B}$. We know that the number operator $\hat{a}^\dagger \hat{a}$ has

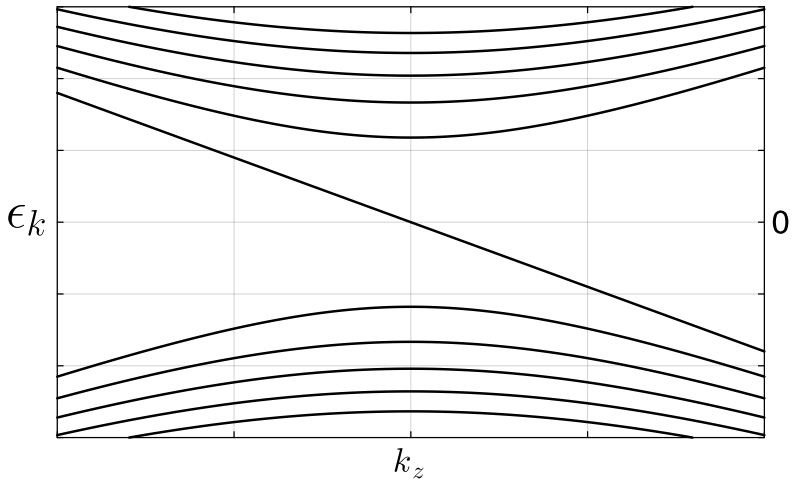

Figure 5.1: Landau level dispersion for a 3d Dirac point described by Eq. (5.9). The lowest LL is a gapless, chiral mode with linear dispersion $\epsilon(k_z) = -v_F k_z$. For the higher bands the level spacing decreases $\propto \sqrt{n} - \sqrt{n-1}$.

eigenstates $|n\rangle$ with $\hat{a}^\dagger \hat{a} |n\rangle = n |n\rangle$. The operators $\hat{a}$ and $\hat{a}^\dagger$ take $|n\rangle$ to the next lowest/highest state, e.g. $\hat{a} |n\rangle = \sqrt{n} |n-1\rangle$. Thus, we make an ansatz to solve the Hamiltonian by these eigenfunctions

$$\begin{pmatrix} v_F k_z & \Omega_c \hat{a} \\ \Omega_c \hat{a}^\dagger & -v_F k_z \end{pmatrix} \begin{pmatrix} \psi_{n-1,\uparrow} \\ \psi_{n,\downarrow} \end{pmatrix} = \begin{pmatrix} v_F k_z & \Omega_c \sqrt{n} \\ \Omega_c \sqrt{n} & -v_F k_z \end{pmatrix} \begin{pmatrix} \psi_{n-1,\uparrow} \\ \psi_{n,\downarrow} \end{pmatrix}, \tag{5.11}$$

with $\psi_n = \mathrm{e}^{ik_z z} |n\rangle$ and spin $\sigma = \uparrow, \downarrow$. This expression is valid for $n \geq 1$. The resulting eigenenergies are $E(n, k_z) = \pm v_F \sqrt{k_z^2 + 2eBn}$. Thus, we have obtained multiple 1d-bands described by the Landau level index n. The lowest Landau level ($n = 0$) requires special attention as we have $a |0\rangle = 0$. Here, the Hamiltonian reads

$$\begin{pmatrix} v_F k_z & \Omega_c \hat{a} \\ \Omega_c \hat{a}^\dagger & -v_F k_z \end{pmatrix} \begin{pmatrix} 0 \\ \psi_{0,\downarrow} \end{pmatrix} = \begin{pmatrix} v_F k_z & 0 \\ 0 & -v_F k_z \end{pmatrix} \begin{pmatrix} 0 \\ \psi_{0,\downarrow} \end{pmatrix}. \tag{5.12}$$

This leads to a single chiral state with dispersion $E(n = 0, k_z) = -v_F k_z$. A corresponding node with opposite chirality would have a dispersion with positive sign.

One should note that the spacing between Landau levels is not constant in a 3d Dirac system (as is the case for Schrödinger-like fermions with a dispersion $E \sim k^2$). Instead, the level spacing between neighboring levels behaves like $\sqrt{n} - \sqrt{n-1}$. Experimentally, this allows us to reach the lowest LL at smaller fields and probe its chiral properties [60].

5.3 Flat bands in nodal line semimetals

We now turn to our nodal line Hamiltonian to investigate it in a similar way as we did for the 3d Dirac system in the previous section. We choose the magnetic field pointing along

the a-direction (just like in the experiment) and define the vector potential as $\vec{A} = By\vec{e}_b$. The total Hamiltonian can then be written as:

$$H = v_a k_a \sigma_z \otimes \tau_x + v_b(k_b + eBy)\sigma_x \otimes \tau_x + vck_c \mathbb{1} \otimes \tau_y + \Delta \mathbb{1} \otimes \tau_x - \frac{g\mu_B B}{2}\sigma_x \otimes \mathbb{1}. \quad (5.13)$$

In an effort to quantize this Hamiltonian, we first perform a unitary transformation $U = \exp(i\pi\sigma_y \otimes \mathbb{1}/4)$ which maps $\sigma_z \to \sigma_x$ and $\sigma_x \to -\sigma_z$. Additionally, we introduce ladder operators $\hat{a} = \frac{l_B}{\sqrt{2v_b v_c}}(v_b(k_b + eBy) + iv_c k_c)$ such that $[\hat{a}, \hat{a}^\dagger] = 1$. The transformed Hamiltonian in matrix form is then given by

$$U^\dagger H U = \begin{pmatrix} \frac{g\mu_B B}{2} & -\Omega_c \hat{a} + \Delta & 0 & v_a k_a \\ -\Omega_c \hat{a}^\dagger + \Delta & \frac{g\mu_B B}{2} & v_a k_a & 0 \\ 0 & v_a k_a & -\frac{g\mu_B B}{2} & \Omega_c \hat{a}^\dagger + \Delta \\ v_a k_a & 0 & \Omega_c \hat{a} + \Delta & -\frac{g\mu_B B}{2} \end{pmatrix}, \quad (5.14)$$

with the cyclotron energy $\Omega_c = \frac{\sqrt{2v_b v_c}}{l_B} \sim \sqrt{B}$. In this representation, the states will be labeled as $|\psi_{n,\sigma,\tau}(k_a)\rangle$ with $\sigma = \uparrow, \downarrow$ and $\tau = \pm$. Comparing to our previous example in chapter 5.2, we see that the Hamiltonian of our nodal line semimetal is not block-diagonal in the quantum number n. The operators $\hat{a}^\dagger, \hat{a}$ raise/lower the Landau level index while the symmetry-breaking term $\Delta \mathbb{1} \otimes \tau_x$ does not change this quantum number. For $\Delta = 0$ we can use the eigenstates of the number operator $|\psi_n\rangle = (0, |\psi_{0,\uparrow,-}\rangle, |\psi_{0,\downarrow,+}\rangle, 0)$ for $n = 0$ and $|\psi_n\rangle = (|\psi_{n-1,\uparrow,+}\rangle, |\psi_{n,\uparrow,-}\rangle, |\psi_{n,\downarrow,+}\rangle, |\psi_{n-1,\downarrow,-}\rangle)$ for $n \geq 1$ and diagonalize separately for each value of n. Turning on a finite Δ couples the states $|\psi_n\rangle$ with $|\psi_{n-1}\rangle$ and $|\psi_{n+1}\rangle$. In this case, we write the Hamiltonian as a large $(4N + 2) \times (4N + 2)$ matrix with the cutoff N chosen such that the eigenenergies of the lowest energy states do not change upon increasing the matrix size. The two energy scales which determine the strength of the coupling are Δ and $\Omega_c\sqrt{n} = \sqrt{2v_b v_c eBn}$. From this we see that for lower magnetic fields more states have to be taken into account, leading to a larger matrix that we need to diagonalize.

Of particular relevance for nodal line semimetals in a magnetic field is the lowest Landau level which, in contrast to the 3d Dirac system, is not chiral but has interesting other properties. We start by setting $k_a = 0$, splitting the Hamiltonian into 2×2 blocks $H_\uparrow, H_\downarrow$ with different spins. Each of these Hamiltonians describes a 2d Weyl point and the two crossings have a momentum-space separation of $\delta k_b = 2\Delta/v_b$. Neglecting the Zeeman term for now, $H_{\uparrow/\downarrow}$ can be written as

$$H_\uparrow = \begin{pmatrix} 0 & -\Omega_c \hat{a}_\uparrow \\ -\Omega_c \hat{a}_\uparrow^\dagger & 0 \end{pmatrix}, \qquad H_\downarrow = \begin{pmatrix} 0 & \Omega_c \hat{a}_\downarrow^\dagger \\ \Omega_c \hat{a}_\downarrow & 0 \end{pmatrix}, \quad (5.15)$$

with lowering operators $\hat{a}_{\uparrow/\downarrow} = \frac{l_B}{\sqrt{2v_c v_b}}(v_b(k_b \mp \delta k_b/2) + v_b Bey + ik_c v_c)$.

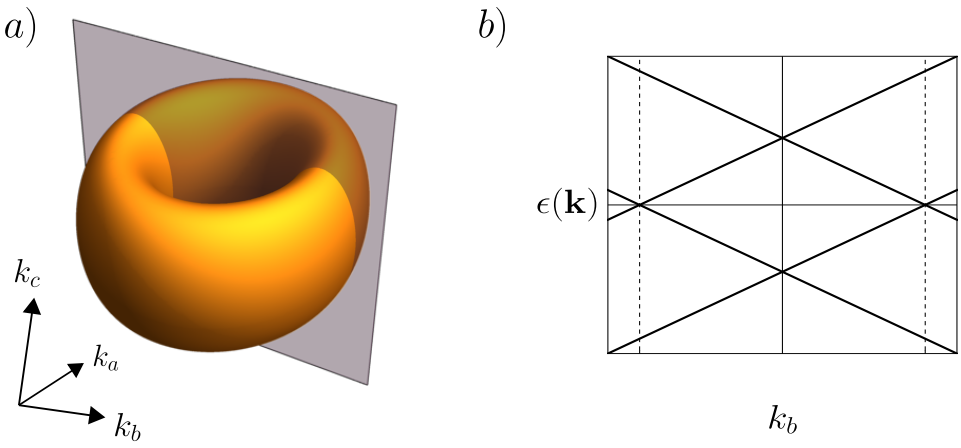

Figure 5.2: a) Torus Fermi surface in the a-b-plane. The grey plane indicates a cut at $k_a = 0$ leaving us with two linear crossings. b) The band structure for $k_a = k_c = 0$ has two Weyl crossings at $\epsilon = 0$. Under Landau quantization, these points will lead to a zero energy state.

Importantly, the lowest Landau levels are located at zero energy with the eigenstates

$$\psi_{0,\uparrow} = \begin{pmatrix} 0 \\ \psi_{0,\uparrow,-}(k_b, y, z) \end{pmatrix}, \qquad \psi_{0,\downarrow} = \begin{pmatrix} \psi_{0,\downarrow,+}(k_b, y, z) \\ 0 \end{pmatrix}, \tag{5.16}$$

$$\begin{aligned} \psi_{0,\uparrow,-}(k_b, y, z) &= \left(\frac{v_b}{\pi v_c l_B^2}\right)^{1/4} \exp\left(-\frac{v_b}{2l_B^2 v_c}\left(y + l_B^2\left(k_b - \delta k_b/2\right)\right)^2\right) e^{ik_b z}, \\ \psi_{0,\downarrow,+}(k_b, y, z) &= \left(\frac{v_b}{\pi v_c l_B^2}\right)^{1/4} \exp\left(-\frac{v_b}{2l_B^2 v_c}\left(y + l_B^2\left(k_b + \delta k_b/2\right)\right)^2\right) e^{ik_b z}. \end{aligned} \tag{5.17}$$

The width of the eigenstates is thus given by $\Delta W = l_B\sqrt{v_c/v_b}$ and the spatial separation in y-direction is $\Delta y = l_B^2 \delta k_b = 2\Delta/v_b$. If we make a cut at finite k_a, we instead have two Weyl points separated by $\delta k_b(k_a) = 2\sqrt{(\Delta/v_b)^2 - k_a^2}$ but our previous consideration remains valid as long as the wavefunctions do not overlap, meaning $\Delta W \ll \Delta y$. This is true for $B \ll \delta k_b^2 v_b/(e v_c) \approx 80$ T which is way larger than the magnetic fields used in the experiments (up to 8 T). Thus, we obtain a degenerate zero energy state for a range of k_a values as is characteristic for a nodal line semimetal [61].

Next, we construct an effective Hamiltonian from degenerate perturbation theory, taking into account the overlap of the two states as well as the Zeeman term:

$$\begin{aligned} H(k_a, k_b) &= \begin{pmatrix} \frac{g\mu_B B}{2} & k_a v_a \int \mathrm{d}y\ \psi^*_{0,\uparrow,-}(k_b, y, z)\psi_{0,\downarrow,+}(k_b, y, z) \\ k_a v_a \int \mathrm{d}y\ \psi^*_{0,\downarrow,+}(k_b, y, z)\psi_{0,\uparrow,-}(k_b, y, z) & -\frac{g\mu_B B}{2} \end{pmatrix} \\ &\sim \begin{pmatrix} \frac{g\mu_B B}{2} & 2k_a v_a e^{-(l_B \delta k_b)^2 v_b/(2v_c)} \\ 2k_a v_a e^{-(l_B \delta k_b)^2 v_b/(2v_c)} & -\frac{g\mu_B B}{2} \end{pmatrix}. \end{aligned} \tag{5.18}$$

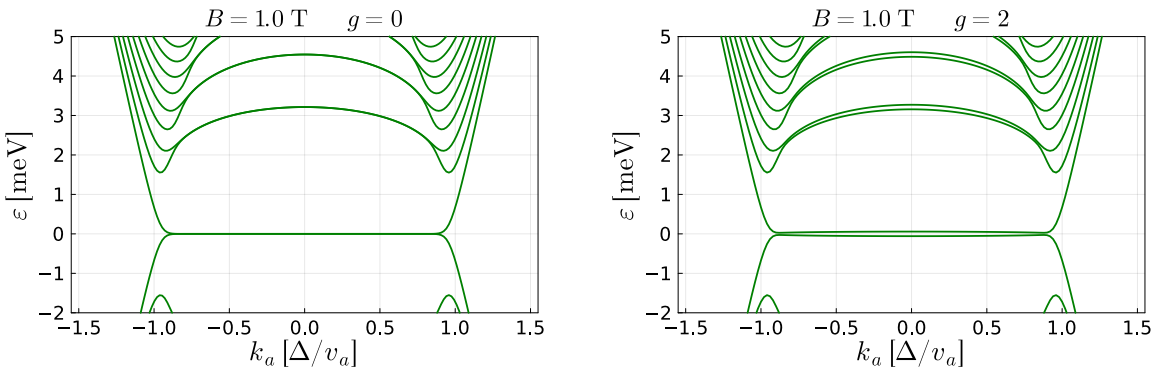

Figure 5.3: Band structure of the nodal line semimetal in a magnetic field. Without Zeeman coupling ($g = 0$) the lowest LL sits at zero energy and is degenerate in an extended region of momenta. Turning on a finite Zeeman term opens a k_a-dependent gap and also splits the degeneracy of higher Landau levels.

Indeed, the overlap between the eigenstates vanishes exponentially as $e^{-(l_B \delta k_b)^2 v_b/(2v_c)}$. The diagonalization of this effective Hamiltonian gives us the energies $\epsilon_f^{\pm}$ and the velocities $v_f^{\pm}$ of the lowest Landau levels as

$$\begin{aligned} \epsilon_f^{\pm} &= \pm\sqrt{(g\mu_B B/2)^2 + (2k_a v_a)^2 e^{-(l_B \delta k_b)^2 v_b/v_c}} \\ v_f^{\pm} &= \pm v_a \frac{4k_a v_a e^{-(l_B \delta k_b)^2 v_b/v_c}}{\sqrt{(g\mu_B B/2)^2 + (2k_a v_a)^2 e^{-(l_B \delta k_b)^2 v_b/v_c}}} \left(1 + 2(k_a l_B)^2 \frac{v_b}{v_c}\right). \end{aligned} \tag{5.19}$$

In the absence of the Zeeman term ($g = 0$) we obtain the band structure seen in Fig. 5.3 a) which shows a pronounced zero-energy state that starts dispersing for $k_a \approx \Delta/v_a$ due to the overlap of two Weyl cones. Additionally, the higher bands do not feature such a flat region and are much more dispersive. For a finite g-factor a k_a-dependent gap opens around $\epsilon = 0$. Furthermore, the Zeeman term also lifts the degeneracy of the higher bands. The charge density can be determined by summing over all occupied bands up to the chemical potential μ as

$$n(\mu) = \frac{1}{2\pi\hbar^2 l_B^2} \sum_n \int \frac{dk}{2\pi} f_0(\epsilon_{n,k} - \mu). \tag{5.20}$$

As the experiments are performed at fixed density and the band structure changes substantially with magnetic field (see Fig. 5.4) we need to determine the corresponding chemical potential $\mu = \mu(n, B)$ for each field.

5.4 Boltzmann equation for 1d Landau levels

To calculate the transport properties of our nodal line system in a magnetic field we employ again the Boltzmann equation. Our previous results (4.1) for the three-dimensional

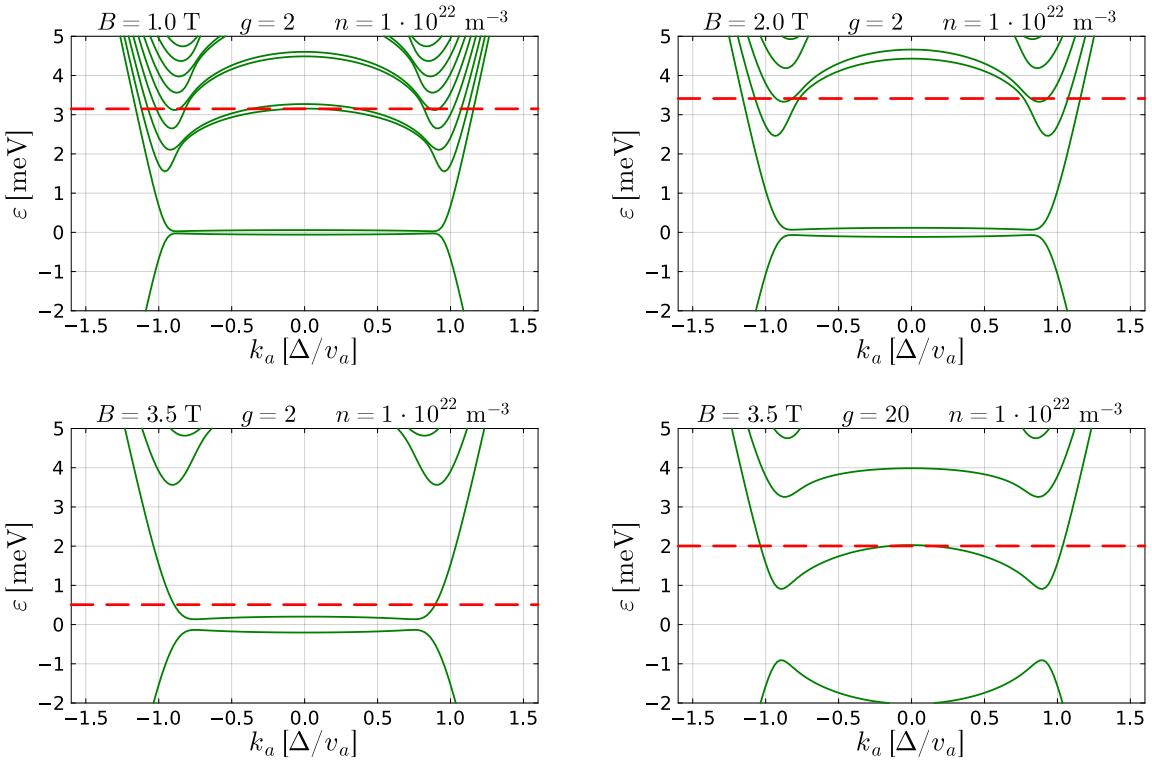

Figure 5.4: Change of the band structure for different magnetic fields. We fix the density $n = 10^{22}$ m^{-3} and indicate the chemical potential by the red dashed line. For larger magnetic fields the gap around zero energy gets bigger and the velocity of the lowest LL increases. Additionally, the higher bands move to larger energies. Increasing the g-factor by a factor of 10 produces a lowest Landau level with comparable band velocities to the next highest band. Here we do not expect to see any of the flatband physics.

Boltzmann equation where only valid for small magnetic fields. Instead, we will directly use the band structure $\epsilon_{n,k}$ of the Landau levels from the previous section. As we now work with a one-dimensional band structure, the Boltzmann equation allows us only to calculate the response to an electric field applied parallel to the magnetic field. The resulting current density is given by a summation over all bands crossing the chemical potential

$$j_{\parallel} = \frac{e}{2\pi\hbar^2 l_B^2} \sum_n \int \frac{\mathrm{d}k}{2\pi} \frac{\partial \epsilon_{n,k}}{\partial k} f_{n,k}, \tag{5.21}$$

with the magnetic length $l_B = \sqrt{\hbar/(eB)}$. The prefactor takes into account the degeneracy of the Landau levels in the directions perpendicular to the magnetic field. Our approach does not consider interband processes e.g. due to a broadening of the Landau levels from impurities. Thus, we consider the limit where scattering rates are smaller than the distance between bands. For each band we can then write

$$eE \frac{\partial f_{n,k}}{\partial k} = \frac{f_{n,k} - f_0(\epsilon_{n,k} - \mu)}{\tau_k}. \tag{5.22}$$

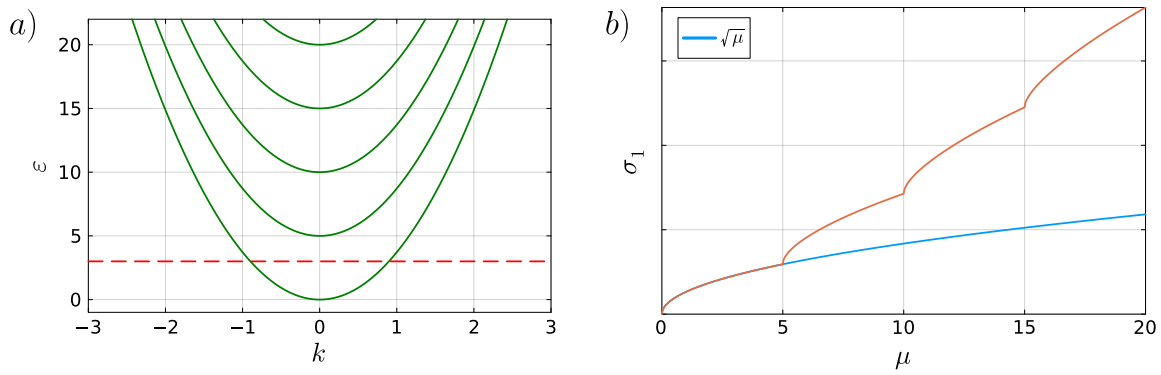

Figure 5.5: a) Quadratic band structure of a Schrödinger-like material in a magnetic field. The chemical potential is indicated by the dashed red line. b) Conductivity of this band structure (orange) calculated via the Boltzmann equation. Each band has a conductivity $\sim \sqrt{\mu}$ and gets activated once the chemical potential touches the band bottom. The blue line shows just the contribution of the lowest band.

The transport scattering time τ_k can strongly vary with magnetic field and charge density. As we are mainly interested in the coefficient γ_3, which is independent of scattering time, we can write all formulas with a constant τ knowing that these factors cancel out in the end. In this case, the 1st-order contribution to the distribution function is given by

$$f^{(1)}_{n,k} = \frac{e}{\hbar}\tau E \frac{\partial \epsilon_{n,k}}{\partial k}\frac{\partial f_0(\epsilon_{n,k}-\mu)}{\partial \epsilon_{n,k}}, \tag{5.23}$$

which gives us the linear conductivity

$$j_1 = \frac{e^3 \tau E B}{2\pi\hbar^3}\sum_n \int \frac{\mathrm{d}k}{2\pi}\left(\frac{\partial \epsilon_{n,k}}{\partial k}\right)^2 \frac{\partial f_0(\epsilon_{n,k}-\mu)}{\partial \epsilon_{n,k}} = \sigma_1 E. \tag{5.24}$$

The prefactor linear in B comes from the degeneracy of the Landau levels which increases with magnetic field. Note that additional B-dependence comes in through the band structure $\epsilon_{n,k}$ and the chemical potential. In the limit of temperature going to zero, we have $\frac{\partial f_0(\epsilon_{n,k}-\mu)}{\partial \epsilon_{n,k}} = -\delta(\epsilon_{n,k}-\mu)$.
As a first sanity check we can consider equally spaced quadratic bands with dispersion $\epsilon_n(k) = \frac{\hbar^2 k^2}{2m} + n\epsilon_0$, see Fig. 5.5. A single band should have a conductivity given by

$$\sigma \sim e^2\tau \int \mathrm{d}k \frac{\partial^2 \epsilon_{n,k}}{\partial k^2} f_0(\epsilon_{n,k}-\mu) \sim \frac{e^2\tau}{m}\int \mathrm{d}k f_0(\epsilon_{n,k}-\mu). \tag{5.25}$$

The remaining integral is simply the total charge density of our system which, for this band structure, is proportional to $\sqrt{\mu}$. As a function of chemical potential we thus expect the conductivity increasing $\sim \sqrt{\mu}$ every time we hit the bottom of a new band. This behavior can be seen in Fig. 5.5.

To calculate the coefficient γ_3 we also need the 3rd-order distribution function which takes

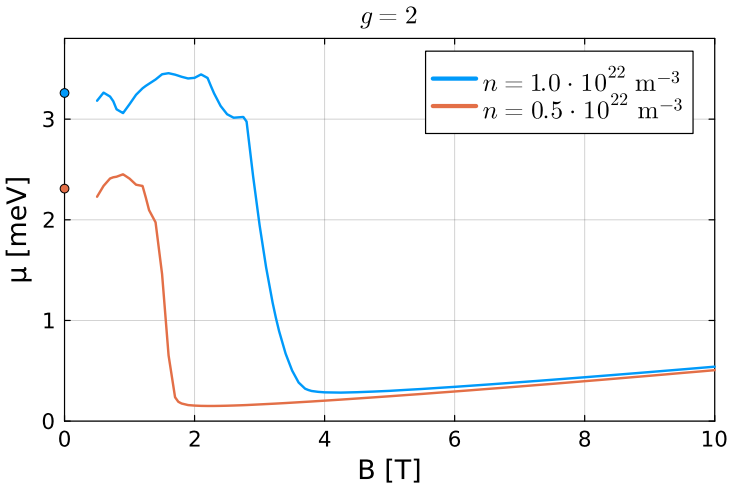

Figure 5.6: Chemical potential as a function of magnetic field for fixed density. As the flat LL can host a large number of states, μ drops sharply once the quantum limit is reached. The drop into the flat band regime occurs earlier for smaller density. The linear increase for large fields is due to the Zeeman term shifting all bands up. The chemical potential will stay pinned to the LL.

the form

$$f^{(3)}_{n,k} = \frac{e^3}{\hbar^3}\tau^3 E^3 \frac{\partial^3 f_{0,n}(k)}{\partial k^3} = \frac{e^3}{\hbar^3}\tau^3 E^3 \left(\frac{\partial^3 \epsilon_{n,k}}{\partial k^3}\frac{\partial f_{0,n}(k)}{\partial \epsilon_{n,k}} + 2\frac{\partial^2 \epsilon_{n,k}}{\partial k^2}\frac{\partial}{\partial k}\frac{\partial f_{0,n}(k)}{\partial \epsilon_{n,k}} + \frac{\partial \epsilon_{n,k}}{\partial k}\frac{\partial^2}{\partial k^2}\frac{\partial f_{0,n}(k)}{\partial \epsilon_{n,k}} \right).$$

Inserting this result into the formula for the conductivity gives us

$$j_3 = \frac{e^5\tau^3 E^3 B}{2\pi\hbar^5} \sum_n \int \frac{dk}{2\pi}\frac{\partial \epsilon_{n,k}}{\partial k}\frac{\partial^3 \epsilon_{n,k}}{\partial k^3}\frac{\partial f_0(\epsilon_{n,k}-\mu)}{\partial \epsilon_{n,k}} = \sigma_3 E^3. \tag{5.26}$$

This allows us to define the nonohmic coefficient γ_3 as

$$\gamma_3(B) = \frac{\sigma_3}{(\sigma_1)^3} = \frac{(2\pi\hbar)^4}{e^4 B^2} \frac{\sum_n \int \frac{dk}{2\pi}\frac{\partial \epsilon_{n,k}}{\partial k}\frac{\partial^3 \epsilon_{n,k}}{\partial k^3}\frac{\partial f_0(\epsilon_{n,k}-\mu)}{\partial \epsilon_{n,k}}}{\left(\sum_n \int \frac{dk}{2\pi}\left(\frac{\partial \epsilon_{n,k}}{\partial k}\right)^2 \frac{\partial f_0(\epsilon_{n,k}-\mu)}{\partial \epsilon_{n,k}}\right)^3}. \tag{5.27}$$

5.5 Tuning into the flat band regime

In this chapter we want to apply the previously derived expressions to the band structure of our nodal line semimetal. As we do not have an analytic expression for the Landau levels, we will only resort to numerical results.

Firstly, we determine the chemical potential as a function of magnetic field for a fixed density via Eq. (5.20). As the degeneracy of the Landau levels increases with magnetic field, we expect the chemical potential to lower. Additionally, the band structure also changes with field, moving all bands to higher energies and changing their dispersion. The resulting curves for two different densities can be seen in Fig. 5.6. The values for

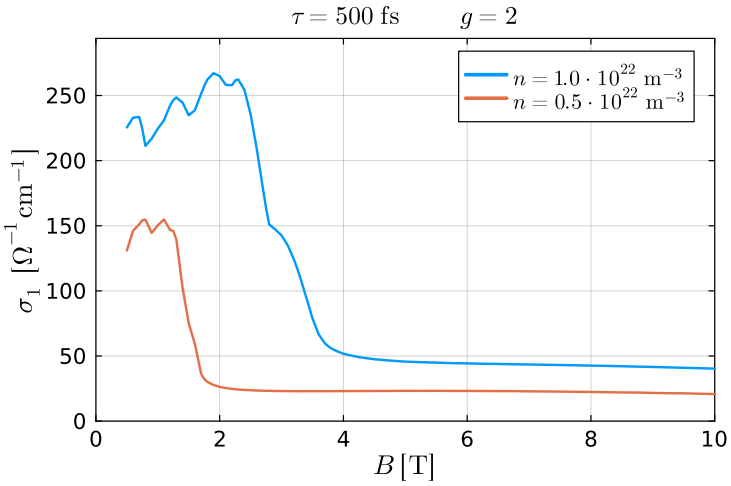

Figure 5.7: Linear conductivity for the Landau levels in relaxation time approximation. Just like for the chemical potential, we see oscillations at small fields and a sudden drop as the quantum limit is reached. As the field increases, the band structure does not change much leading to an almost constant conductivity.

the smallest fields fit well with the results at $B = 0$ where we have obtained $\mu(n) = \sqrt{4\pi\hbar^3 v_a v_b v_c n/\Delta}$, which is shown as single points in Fig. 5.6. For low fields the chemical potential oscillates as the band structure changes. The most prominent feature is a sharp drop when the quantum limit is reached. Here, the chemical potential drops rapidly to the bottom of the flat band which can host a vast number of electrons. For smaller densities this drop takes place at lower magnetic fields. When increasing the field further, the chemical potential increases linearly due to the growing Zeeman gap but it will stay pinned to the bottom of the flat band.

After we have determined the correct chemical potential, we can calculate the linear conductivity (5.24) which can be seen in Fig. 5.7. To obtain the derivative of the dispersion we use an interpolation of the band structure on the momentum interval $[-2\Delta/v_a, 2\Delta/v_a]$ with discretization step $\Delta k = 0.002\Delta/v_a$. This calculation is done for a constant relaxation time as its field dependence can not be determined from the Boltzmann formalism. The conductivity shows similar features to the chemical potential as we see oscillations at small fields and a sharp drop once we reach the quantum limit. Due to the small velocity of the lowest LL the conductivity reduces by a factor of 5 for both curves. As the dispersion of the flat band does not change much when the field is increased, the conductivity stays approximately constant.

This behavior is only observed for small g-factors. If the Zeeman coupling is too large, the flat band will already have a significant dispersion when the quantum limit is reached as can be seen in Fig 5.4 d). In this limit, we do not observe any signatures of flat band physics in the chemical potential or linear conductivity, see Fig. 5.8. Thus, we will focus on small Zeeman couplings to study the properties of the flat band. As we turn to the third-order conductivity, higher-order derivatives of the dispersion are needed. Additionally,

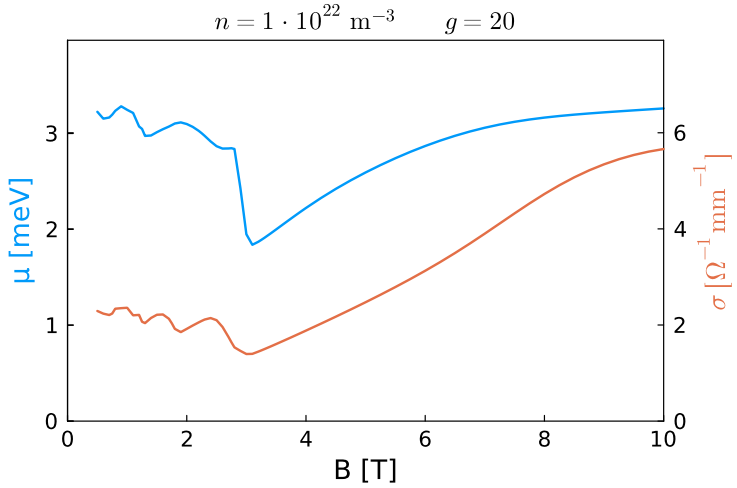

Figure 5.8: Chemical potential and linear conductivity for large Zeeman coupling. The chemical potential drops when reaching the quantum limit but not by an order of magnitude as for smaller g-factors. The conductivity also shows a different behavior as the LL is much more dispersive.

the third power of the scattering time enters Eq. (5.26). As previously mentioned, the relaxation rate should have a strong dependence on magnetic field and density which would drastically affect the nonlinear conductivity. This means that $\sigma_3(B)$ for a fixed τ is not suited for predicting the correct field dependence. One important feature indicating the system entering the flat-band regime can be seen in Fig. 5.9 at $B = 3.5$ T. Here, all electrons sit in the lowest LL and σ_3 changes sign. Besides the band velocity also the change of curvature of the bands enters the expression for σ_3. This higher derivative of the band structure is responsible for the sign change of the nonlinear conductivity as the flat-band regime is reached.

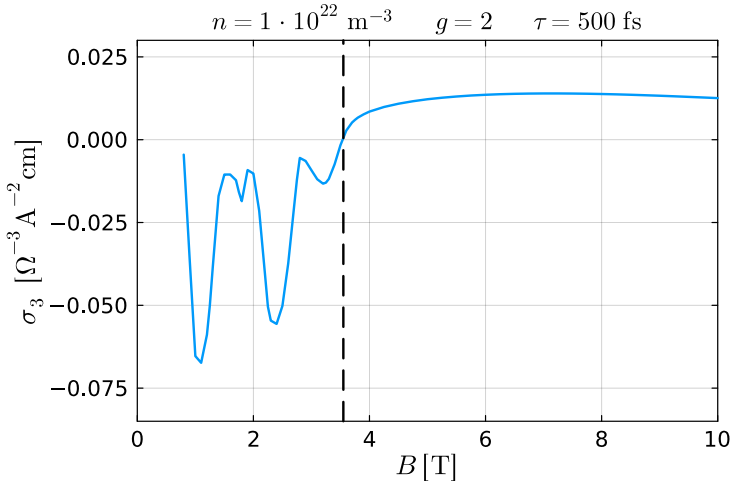

Figure 5.9: Third order conductivity as a function of magnetic field for constant relaxation time. The dashed line indicates the onset of the flat band regime where σ_3 changes sign. As the scattering rate is highly field dependent and $\sigma_3 \sim \tau^3$ the correct field dependence of the nonohmic response is only captured by the coefficent γ_3.

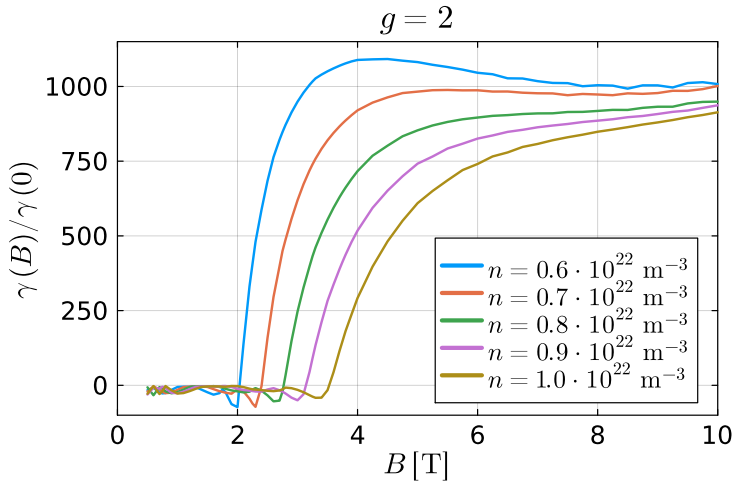

Figure 5.10: Nonohmic coefficient for different carrier densities as a function of magnetic field. A large enhancement of γ_3 is observed when the flat band regime is reached. The nonohmic coefficent saturates deep in the quantum limit.

To circumvent this problem of scattering rates changing in a magnetic field, we consider the nonohmic coefficient γ_3 from Eq. (5.27). As we tune into the flat band regime, the linear conductivity becomes small and will dominate the ratio γ_3. Thus, as the magnetic field is increased the nonohmic coefficient grows by up to 3 orders of magnitude, see Fig. 5.10. This very sharp rise levels off when the field is further increased leading to a saturation of the nonohmic coefficient. For larger electron densities, higher fields are needed to reach the flat band regime and the enhancement is less pronounced.

5.6 Experiments

This section closely follows the introduction of publication 2 [59]. In the group of Prof. Ando, Yongjian Wang performed transport experiments with dc-currents along the a-direction for different orientations of magnetic field. Fig. 5.11 a) shows the current-voltage relation for fields in the ab-plane. At $\theta = 90°$, $\mathbf{B}$ is parallel to the current and the data shows the largest nonlinearity. Turning the magnetic field away from this configuration by about 6-10 degrees leads to much more linear curves. The solid lines in Fig. 5.11 a) are fits to the data with which the conductivities are extracted. As a fit function we use

$$I = \sigma_1 \frac{A}{d} V + \sigma_3 \frac{A}{d^3} V^3 + \sigma_5 \frac{A}{d^5} V^5, \tag{5.28}$$

where A is the cross-section of the sample and d is the distance of contacts which measure the voltage drop. It turns out that σ_5 follows a similar behavior as σ_3 and therefore we can characterize the nonlinear properties by focussing on σ_3. This allows us to get the nonohmic coefficient γ_3 for different magnetic field orientations which can be seen in Fig. 5.11 b). It can be seen that γ_3 shows a sharp peak for the longitudinal transport

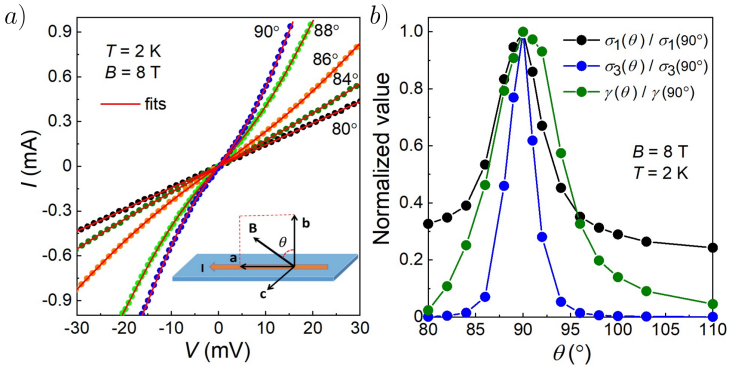

Figure 5.11: **Current-voltage profile for samples with $T_p = 0$:** a) I-V curves for different magnetic field angles in the ab-plane. The solid lines show fits up to fifth order in electric field. From these curves σ_1, σ_3 and γ_3 can be extracted. b) The nonohmic coefficent shows a sharp peak around 90°. All curves are normalized by their maximal value with $\gamma_3^{\max} = 35.9 \cdot 10^{-12}$ m^{4}A^{-2}. Figures taken from publication 2 [59].

configuration at $\theta = 90°$. Here, the nonohmic coefficent has a maximal value of $\gamma_3^{\max} = 35.9 \cdot 10^{-12}$ m^{4}A^{-2}. For completion, additional measurements with field orientations in the ac-plane result in the same maximal value for $\mathbf{B} \parallel \hat{a}$ and a sharp peak when rotating the magnetic field. As $ZrTe_5$ is an anisotropic material the g-factor also depends on the direction of the applied field. Experimentally, the Zeeman coupling was determined to be about one order smaller than in the b-direction with $g_a \approx 2$ [36, 56]. The nonohmic behavior is only seen in samples where the resistivity $\rho_{xx}(T)$ has a peak at $T_p = 0$. Here, the carrier density is small and the system is in the nodal line phase. On the other hand, a sample with finite $T_p = 133$ K shows a linear I-V curve with $\gamma_3 = 0$ within the error bars of the fit for any value of magnetic field. Such a sample has larger density and a chemical potential $\mu > \Delta$, which results in an ellipsoid Fermi surface. Thus, just like the MCA we associate the existence of a sizable nonohmic transport with the nodal line semimetal phase of $ZrTe_5$.

5.6.1 Enhancement of γ_3 in a magnetic field

The previous measurements are all taken at a fixed magnetic field $B = 8$ T. We can learn a lot about the nonohmic transport by considering the field-dependence of γ_3 which can be seen in Fig. 5.12 a) for different samples. All samples show a similar behavior where the nonohmic coefficient grows by about a factor of 10 as the magnetic field is increased to 8 T. A rapid increase is seen at a few Tesla where the system enters the quantum limit. Afterwards the nonohmic coefficent saturates and shows an almost constant plateau for large fields. As the enhancement by one order of magnitude is universal for all samples we can attribute it to an intrinsic mechanism. In accordance with our theory the nonohmic coefficient increases as we reach the quantum limit and the charge carriers go into the lowest LL. In contrast to the experimental data, the

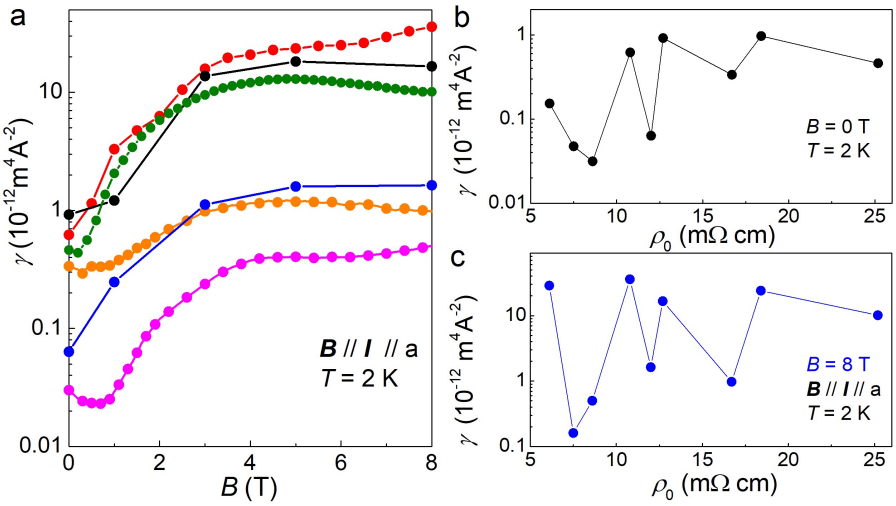

Figure 5.12: **Magnetic field dependence of γ_3 for various samples:** a) All samples show an enhancement of about one order of magnitude when increasing the magnetic field to 8 T. The absolute size of γ_3 both at $B = 0$ and at large fields is very sample dependent. b),c) Nonohmic coefficent as a function of residual resistivity ρ_0. One obtains the largest values of γ_3 at $B = 8$ T for samples with large γ_3 values in the absence of a magnetic field. In both plots there is no clear correlation between γ_3 and ρ_0. Figures taken from publication 2 [59].

theoretical result (Fig. 5.10) predicts a substantially larger enhancement of $\gamma_3(B)/\gamma_3(0) \sim 10^3$. As previously stated, the main reason for the enhancement is the rapid decrease of linear conductivity. However, the Boltzmann theory is only valid as long as the scattering rates are smaller than the distances between Landau levels and the corresponding bandwidths. In the flat-band regime interband scattering due to impurities becomes the main mechanism for transport as the dispersive contribution becomes very small. Thus, our theory which just sums up single-band contributions fails to fully describe the flat-band regime and overestimates the enhancement of the nonohmic coefficient.

5.6.2 Puddle-induced nonlinearity at small fields

While we see a similar magnetic field-induced enhancement in all samples, the absolute value of γ_3 is very sample dependent and varies by more than an order of magnitude. Characterizing each sample by their density would require a lot of quantum oscillation measurements. As previously mentioned, $ZrTe_5$ samples which have a resistivity peak at $T_p = 0$ have a small carrier density. Therefore these samples posses tiny Fermi surfaces which are complicated to measure via SdH oscillations. Instead, we distinguish the samples via the residual resistivity ρ_0. Fig. 5.12 b), c) show ρ_0 versus the nonohmic coefficient at zero field and for 8 T for all measured samples. Both plots show no clear correlation of the two quantities. It should be mentioned that samples with larger γ_3 at $B = 0$ also

have larger nonohmic coefficients at high fields. In the absence of a magnetic field, our theory predicts $\gamma_3(B=0) = 2.1 \cdot 10^{-18}$ m^4/A^2 for a realistic density $n = 10^{22}$ m^{-3}, which is several orders of magnitude smaller than the experimental observed coefficient. As for the MCA, this discrepancy can be attributed to an inhomogeneous distribution of charge carriers which is a natural consequence of the low carrier density. As electric fields are screened in metallic parts of the sample, one can obtain large electric fields in low density (almost insulating) regions. If the origin of the nonohmic transport at small fields is due to disorder, a large sample dependence is expected for the size of the nonlinearity.

To investigate the enhancement mechanism by inhomogeneous density distribution, we use again the resistor network model from section 4.3 as the experimental setup of parallel current and magnetic field does not produce a conventional Hall effect [1]. We now consider nonlinear resistors in x-direction while the conductivity perpendicular to the magnetic field will still be linear, thus the currents are given by

$$\begin{aligned} I_x(i,j) &= \sigma_{xx}^{(1)}(i,j)\Delta V(i,j) + \sigma_{xx}^{(3)}(i,j)\Delta V(i,j)^3, \\ I_y(i,j) &= \sigma_{yy}^{(1)}(i,j)\Delta V(i,j), \end{aligned} \tag{5.29}$$

with the linear conductivities being related by the resistivity anisotropy α through $\sigma_{yy}^{(1)}(i,j) = \alpha\ \sigma_{xx}^{(1)}(i,j)$. As we now deal with a set of nonlinear equations obtaining a solution for the voltages from a simple matrix inversion is no longer possible. Instead, we use an iterative solution where we start from an initial guess $V(i,j) = V^{(0)}(i,j)$ for the voltage profile. In each iteration step we change the potential on every node according to

$$V^{(n+1)}(i) = V^{(n)}(i) + \delta V^{(n)}(i). \tag{5.30}$$

The current conservation at node i after an iteration step can be written as

$$\sum_{k=1}^{4} I_i^{(k)}\left(\mathbf{V}^{(n+1)}\right) = \sum_{k=1}^{4} I_i^{(k)}\left(\mathbf{V}^{(n)} + \delta\mathbf{V}^{(\mathbf{n})}\right) \approx \sum_{k=1}^{4} I_i^{(k)}\left(\mathbf{V}^{(n)}\right) + \sum_{k=1}^{4}\sum_{j=1}^{L_x \cdot L_y} \frac{\partial I_i^{(k)}}{\partial V_j}\left(\mathbf{V}^{(n)}\right)\delta V_j^{(n)} = 0, \tag{5.31}$$

where the derivatives $\partial I_i^{(k)}/\partial V_j$ are only non-zero for the same site $j = i$ and the four neighboring sites. Therefore, the sum over index j which would run over all lattice points just contains five finite terms. Collecting these equations we can write a matrix equation for the change $\delta V^{(n)}$

$$\mathbf{I}^{(n)} + M^{(n)} \cdot \delta\mathbf{V}^{(n)} = 0 \quad \Rightarrow \quad \delta\mathbf{V}^{(n)} = -(M^{(n)})^{-1} \cdot \mathbf{I}^{(n)}, \tag{5.32}$$

where the matrix $M^{(n)}$ contains the above mentioned derivatives. Using this relation, we

[1] As we discuss in chapter 6 there is an unconventional parallel-field Hall effect $E_c \sim I_a B_a$. As this effect is small compared to the longitudinal conductivities we neglect it here.

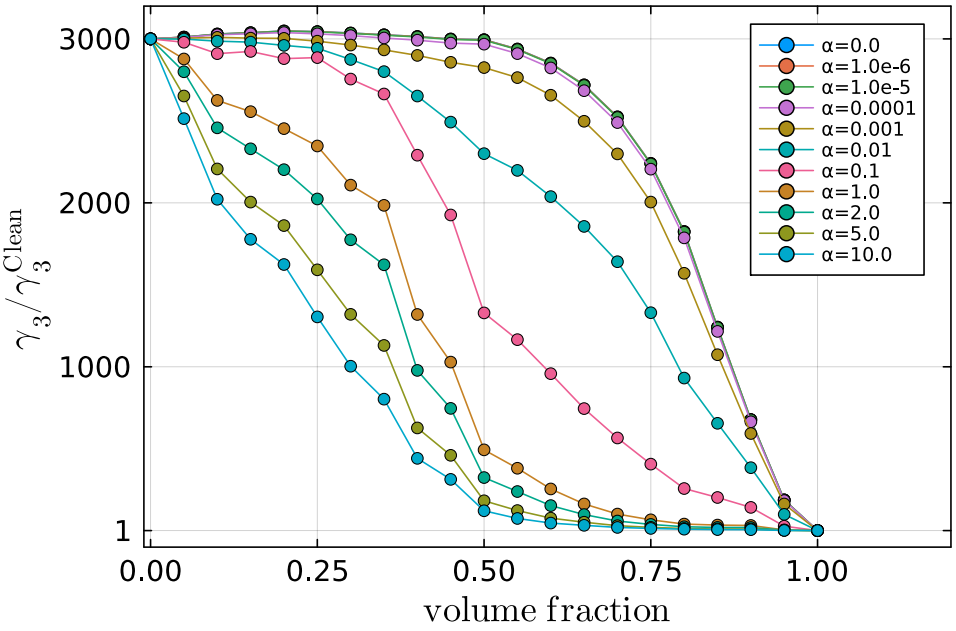

Figure 5.13: Ratio of nonohmic coefficients for a disordered system compared to the clean case as a function of volume fraction for different resistivity anisotropies. $p = 1$ corresponds to the fully homogeneous case where $\gamma_3 = \gamma_3^{\text{Clean}}$ and the ratio is 1. For reasonable anisotropies $\alpha \sim 10^{-2}$ already 20% disorder can lead to an enhancement of the nonohmic properties by 3 orders of magnitude. For $\alpha > 1$ the nonlinear coefficient only increases once percolation of the low-density region takes place. Each data point was averaged over 200 random disorder realizations.

iterate Eq. (5.30) until $\frac{1}{L_x L_y}\sum_i |\delta V^{(n+1)}(i) - \delta V^{(n)}(i)| \leq \epsilon$, where ϵ indicates the desired convergence accuracy.

To determine a nonohmic coefficient for this network we set up random disorder configurations in the same way as in section 4.3. As a boundary condition we fix the externally applied voltage to be V_0 and have $V = 0$ for sites with $x = 0$ and $V = V_0$ at all sites with $x = L_x$. After iteratively solving for the voltage profile we take a cut along the y-direction for a fixed value of x and sum up the local current density along this cut to obtain the total current I. We have checked that the result is independent of the position of the cut and thus the total current is conserved. Varying the external voltage V_0 allows us to extract macroscopic values for the first- and third-order conductance by fitting $I = G^{(1)}_{\text{macro}} V_0 + G^{(3)}_{\text{macro}} V_0^3$. The nonohmic coefficient for the resistor network is then given by $\gamma_3 = G^{(3)}_{\text{macro}} / \left(G^{(1)}_{\text{macro}}\right)^3$. The volume fraction $(1 - p)$ of badly conducting regions will serve as a measure of how much disorder is in the network. Again, we can study networks for different anisotropies where small α will force the current through badly conducting regions with high nonlinear properties. Fig. 5.13 shows the nonohmic coefficient as a function of volume fraction compared to the clean case without disorder. For $p = 1$ we have no disorder in the system and the coefficients are the same giving us a ratio $\gamma_3/\gamma_3^{\text{Clean}} = 1$. Going to $p < 1$ we distinguish two regimes depending on the

anisotropy. For $\alpha \ll 1$ the transport is almost one-dimensional and the current is forced through low density regions. Here, the nonohmic coefficient increases rapidly when going away from the fully homogeneous system. At a reasonable anisotropy $\alpha \approx 10^{-2}$ 20% disorder is sufficient to obtain an enhancement by 3 orders of magnitude. On the other hand, for $\alpha > 1$ a small amount of disorder does not change the nonlinear properties of the system much as currents can just flow around badly conducting parts of the system. In the limit $\alpha \gg 1$ an increase is only seen once the low density region percolates through the network.

In these simulations we have only used two-dimensional networks so far to keep the size of the relevant matrices manageable. In reality, $ZrTe_5$ is a 3d material with different velocities in all three directions. Thus, comparing to a three-dimensional network would be preferable. As the current conservation at each node only needs the local voltage and the voltages at the 4 neighboring nodes (or 6 in three dimensions) most matrix entries are zero. Therefore, sparse matrices can be used to store these finite entries more efficiently. Even though the inverse of a sparse matrix in general is dense, solving a linear equation like Eq. (5.32) numerically can be done much easier for sparse matrices. Hence, three-dimensional networks are also possible to solve where we now have two separate anisotropies α_1, α_2 for the two directions perpendicular to the external electric field. In the experimentally relevant regime of both anisotropies < 1 the results are similar to those of the 2d network shown in Fig. 5.13.

In conclusion, we have demonstrated that a small amount of disorder in an anisotropic system can lead to a large increase of the nonlinear transport properties. Such a mechanism can explain the discrepancy between the homogeneous theory and the experimental results at small magnetic fields. The sample dependence of the size of the nonohmic coefficient can also be attributed to the puddle scenario as the details of the enhancement depend on the disorder realization.

5.7 Kubo formula for linear conductivity

As stated before, the Boltzmann theory underestimates the linear conductivity in the flat-band regime and thus leads to a larger enhancement of the nonohmic coefficient than seen in the experiment. To show this, we employ the full quantum calculation using the Kubo formula. The impurity averaged Greens function $G(\epsilon, \boldsymbol{k}) = (G_0(\epsilon, \boldsymbol{k})^{-1} - \Sigma(\epsilon))$ will contain all information about the disorder through the self-energy Σ which we treat in self-consistent Born approximation. Similar to how we proceeded for the Boltzmann equation we have to adjust our formulas from sections 2.3.1 and 2.4 to apply them for our 1d Landau levels. The only momentum integration remaining will be $k_{||}$ which points in the direction of the magnetic field. Perpendicular to the field the electrons are confined to their Landau orbits and we replace the momentum integrals by a sum over the Landau

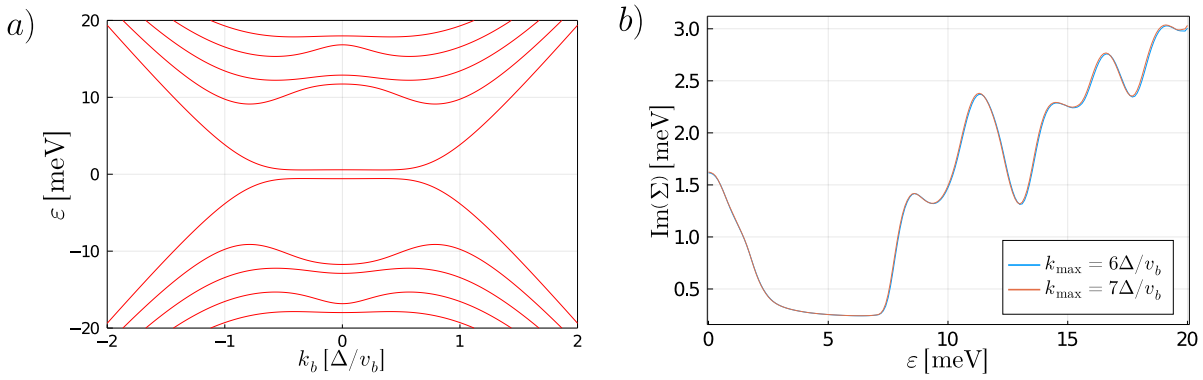

Figure 5.14: a) Band structure for the LLs of a nodal line semimetal in a magnetic field $\boldsymbol{B} \parallel \hat{b}$ at $B = 1$ T. b) Corresponding density of states given by the imaginary part of the self-energy in SCBA. The peak close to zero energy is due to the flat band. After a region with low DoS the higher Landau levels are reached. The results are independent of the momentum cutoff for $k_{\max} > \Delta/v_b$.

level index n [62]. The self-energy in SCBA than can be computed via

$$\Sigma(\epsilon) = \frac{\gamma}{2\pi l_B^2} \sum_n \int \frac{\mathrm{d}k_\parallel}{2\pi} G(\epsilon, k_\parallel, n), \tag{5.33}$$

with the impurity strength $\gamma = n_{\mathrm{imp}} u_0^2$ and the magnetic length $l_B = 1/\sqrt{eB}$. For our numerics we estimate $\gamma = 2 \cdot 10^{-29}$ m^{3}eV^2 from quantum oscillation data. Just like the Hamiltonian, the self-energy will be a 4×4 matrix in the combined space of spin and orbitals. The density of states (DoS) in SCBA is given by tracing over its imaginary part

$$\nu(\epsilon) = -\frac{1}{\pi\gamma} \sum_{\sigma=1}^{4} \mathrm{Im}\Sigma_{\sigma\sigma}(\epsilon). \tag{5.34}$$

Fig. 5.14 shows the DoS at $B = 1$ T for a magnetic field along the b-direction for the LL bandstructure. As the flat band hosts many states there is a large peak close to zero energy. At higher energies there is first a region with a low number of states as we only have two 1d dispersive channels. Once the higher LLs are reached the density of states increases again. When calculating Eq. (5.33) numerically we need to choose a momentum cutoff $k_{\max}$ as well as a maximum Landau level index N up to which our sum goes. For $k_{\max} > \Delta/v_b$ the results are independent of the momentum cutoff as seen in the DoS. The maximum number of Landau levels necessary for convergence depends on the magnetic field as discussed in section 5.3. From the density of states we can compute the carrier density by integrating over all occupied states up to the chemical potential

$$n(\mu) = \int_0^\mu \nu(\epsilon)\mathrm{d}\epsilon, \tag{5.35}$$

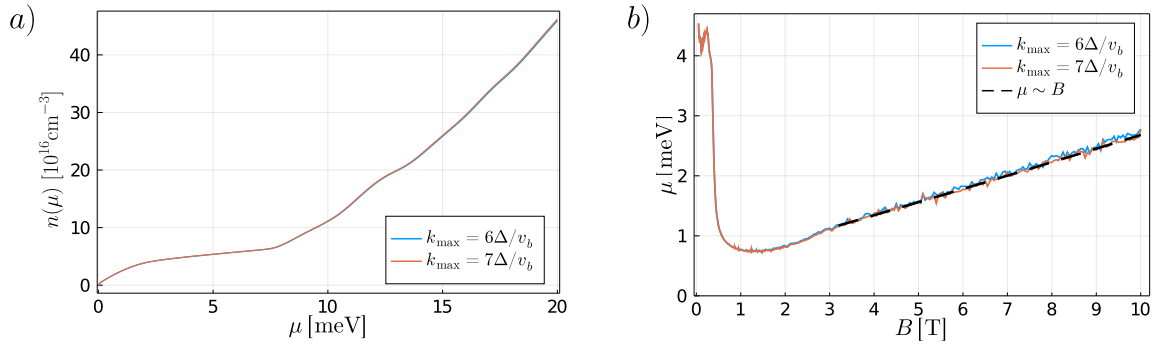

Figure 5.15: a) Carrier density obtained from integrating the DoS up to the Fermi energy for $B = 1$ T with $\boldsymbol{B} \parallel \hat{b}$. b) Chemical potential at fixed density $n_0 = 2 \cdot 10^{22}$ m^3 as a function of magnetic field. In the b-direction the quantum limit is reached at very low fields $B_{\mathrm{cr}} \approx 0.5$ T where μ drops rapidly to the bottom of the flat band. Due to the Zeeman coupling the chemical potential increases linear in B once the lowest LL is reached.

An example is shown in Fig. 5.15 a). At fixed density n_0 we therefore determine the correct chemical potential as a function of magnetic field from $n_0 = n(\mu, B)$. The result for $n_0 = 2 \cdot 10^{22}$ m^3 can be seen in Fig. 5.15 b). For the field along the b-direction the quantum limit is reached at smaller fields than for $\boldsymbol{B} \parallel \hat{a}$ due to the velocity anisotropies. Therefore all electrons already sit in the lowest LL at $B_{\mathrm{cr}} \approx 0.5$ T. At large fields the chemical potential grows linearly with magnetic field due to the Zeeman gap increasing. As in the previous sections the g-factor is chosen such that the lowest LL is still very distinct from the higher bands at the largest field values.
After determining the correct chemical potential we use the Kubo formula without vertex corrections to calculate the longitudinal conductivities. For the 1d LL bandstructure we modify Eq. (2.43)

$$\sigma_{\alpha\alpha}(\mu) = \frac{1}{(2\pi l_B)^2} \sum_n \int \frac{\mathrm{d}k_\parallel}{2\pi} \mathrm{Re}\left(\mathrm{Tr}\left[\boldsymbol{G}^R(\mu, k_\parallel, n) j_\alpha \left(\boldsymbol{G}^R(\mu, k_\parallel, n) - \boldsymbol{G}^A(\mu, k_\parallel, n)\right) j_\alpha\right]\right), \tag{5.36}$$

where the current operators $j_\alpha = e\frac{\partial H}{\partial k_\alpha}$ are constant 4×4 matrices. In contrast to the Boltzmann equation, this calculation allows us to also compute the current response perpendicular to the magnetic field. Fig. 5.16 shows the longitudinal conductivity parallel ($\boldsymbol{I} \parallel \hat{b}$) and perpendicular ($\boldsymbol{I} \parallel \hat{b}$) to $\boldsymbol{B}$. Additionally, for both curves the density of states at the chemical potential is shown. It takes on its minimal value at $B \approx 0.4$ T and then increases in the flat-band regime. At small fields we see quantum oscillations in both conductivities. Along the magnetic field a large scattering rate (high density of states) leads to a reduced current. Peaks in $\nu(\mu)$ therefore correspond to valleys of the conductivity (and vice versa) and $\sigma_{bb} \to 0$ for large fields. Perpendicular to the magnetic field we would not expect any current in the absence of scattering. Due to impurity effects we get a finite conductivity which has local maxima whenever the DoS has a peak as well. σ_{aa} also shows a large increase at smallest fields. For $B \to 0$ more and more LLs have to be

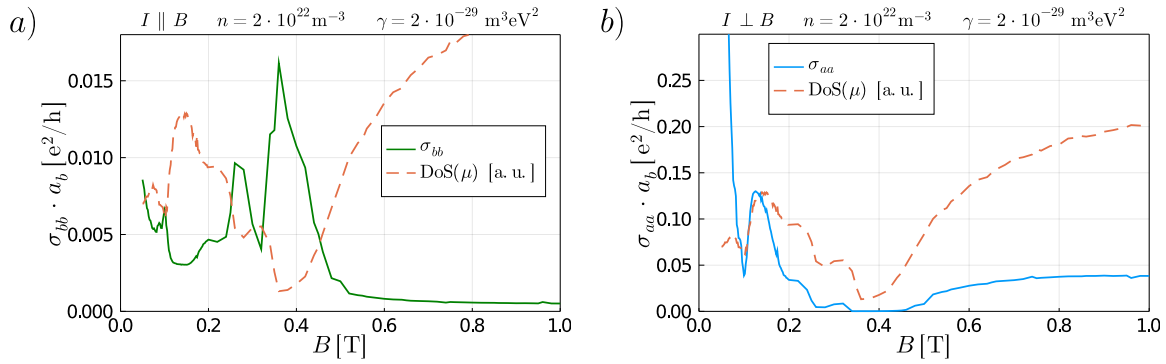

Figure 5.16: **Longitudinal conductivity parallel and perpendicular to the magnetic field:** The orange dashed line indicates the DoS at the Fermi energy. At small fields quantum oscillations are seen in both conductivities and the quantum limit is reached at $B_{\mathrm{cr}} \approx 0.5$ T. a) Along the magnetic field conductivity is enhanced as scattering is suppressed. b) Perpendicular to the field impurities enables finite transport and peaks in σ_{aa} coincide with peaks in $\nu(\mu)$.

taken into account which increases the numerical complexity. As we are more interested in the flat-band regime we therefore did not further investigate this low-field phenomenon.

By treating disorder effects in SCBA we obtained energy-dependent scattering rates which become highly enhanced in the flat-band regime. Therefore, the Boltzmann equation breaks down in this case as the broadening of states is no longer smaller than the band width and gaps between bands. As a consequence, the Boltzmann equation overestimates the enhancement of γ_3 in a magnetic field. The linear conductivity obtained from the Kubo formula better captures the physics in the flat-band regime which is dominated by interband scatterings due to impurities [63].

5.8 Joule heating by coupling to phonons

So far we have neglected the fact that an electric current running through a resistive medium produces heat. The power density generated from Joule heating is given by the product of current density and electric field

$$p = \boldsymbol{j} \cdot \boldsymbol{E}. \tag{5.37}$$

Therefore, the conversion of electrical energy into thermal energy is a nonlinear effect which scales quadratically in the applied electric field as we have $\boldsymbol{j} \sim \boldsymbol{E} + \mathcal{O}(\boldsymbol{E}^2)$. Previously, we have considered impurity scattering described by the collision integral (2.4). The scattering matrix elements $W_{kk'} = \tilde{W}_{kk'}\delta(\epsilon_k - \epsilon_{k'})$ conserve the total energy and only change the momenta of particles and thus their distribution. To include the effect of heating we need to consider the coupling to the ionic lattice of our solid through

electron-phonon scattering. The total collision integral for the electrons will be given by

$$\left.\frac{\partial f}{\partial t}\right|_{\text{coll}} = \sum_{\boldsymbol{k}'} W_{kk'}(f(\boldsymbol{k}') - f(\boldsymbol{k})) - \frac{\delta f(\boldsymbol{k})}{\tau_{\text{el-ph}}}, \tag{5.38}$$

where we treat the electron-phonon coupling in relaxation-time approximation with scattering time $\tau_{\text{el-ph}}$. In the presence of an electric field, energy will be transferred from the electrons to the phonon bath with the temperature change being

$$\delta T \sim E^2 \tau_{\text{el-ph}}. \tag{5.39}$$

Additionally, the linear conductivity will now depend on the bath temperature. We can assume this temperature to be fixed as the experimental setup is placed inside a cryostat. This allows us to write down another term for the nonohmic current j_3 by considering the temperature dependence of the linear current $j_1 \sim E$ due to the temperature change $\delta T \sim E^2$. The total current $\sim E^3$ is therefore given by

$$j_3 \sim \frac{\partial j_1}{\partial T}\delta T + e\int v_k f^{(3)} \mathrm{d}k, \tag{5.40}$$

where the second term is the nonohmic current coming from the band structure which we considered previously. Depending on the size of the electron-phonon coupling and its temperature dependence this new term could lead to a sizable increase of the nonohmic coefficient γ_3 and possibly explain the large discrepancy at zero magnetic field.

5.9 Comparison to Dirac system

To finish this chapter on nonohmic transport, we want to turn away from the experimental system and instead compare the nonlinear transport properties of our nodal line model to a simple Dirac system. For that, we set the symmetry breaking $\Delta = 0$, resulting in a model with 4 bands crossing at $\mathbf{k} = \mathbf{0}$. The corresponding nonohmic coefficient will be labeled as $\gamma_3(\Delta = 0)$. In the absence of a magnetic field, the nonlinear coefficients were already calculated in Eqs. (5.6) and (5.7) from chapter 5.1. In the limit of small densities both coefficients scale with $\gamma_3 \sim 1/n^2$ and have the same dependence on velocity anisotropies. Therefore, without a magnetic field the nonlinear transport properties of the two systems behave very similar and can not be used as a distinguishing feature.

This changes upon turning on the magnetic field and repeating the Boltzmann transport calculation in the Landau level picture for $\Delta = 0$. In Fig. 5.17 a) the band structure of the Dirac system with $\Delta = 0$ is shown. Here, we do not obtain a flat-band region in the lowest LL but instead have linear bands for large momenta which become parabolic at small k and are gapped out by the Zeeman term. The parameters in this plot are chosen such that

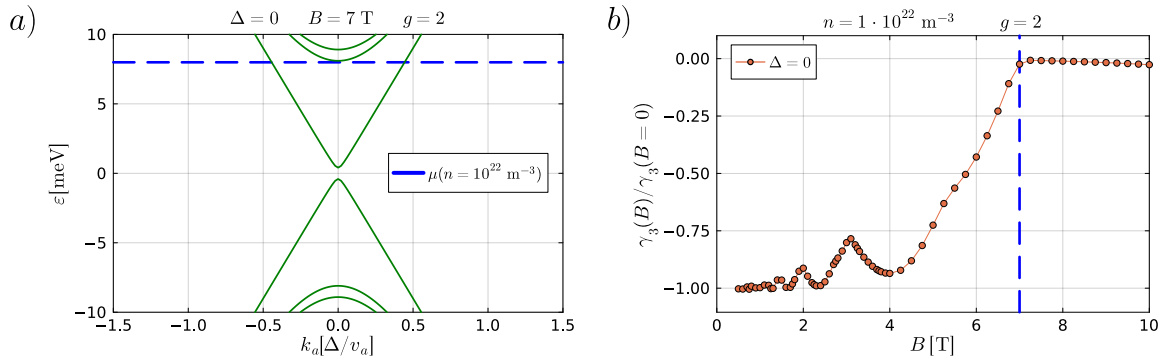

Figure 5.17: a) Band structure for $\Delta = 0$ where the quantum limit is reached at $B = 7$ T for fixed density $n = 10^{22}$ m^{-3}. The dashed blue line indicates the corresponding chemical potential. b) The nonohmic coefficient for $\Delta = 0$ takes on its largest absolute value for small fields and becomes smaller when we go to the quantum limit. The blue dashed line shows the field where the lowest LL is reached.

all particles sit in the lowest LL for a density $n = 10^{22}$ m^{-3}. The corresponding chemical potential is indicated by the dashed blue line. Furthermore, the nonlinear coefficient for $\Delta = 0$ has a very different behavior from the nodal line system. Fig. 5.17 b) shows that $\gamma_3(\Delta = 0)$ has negative sign for all fields and takes on its largest absolute value at small fields. When we increase the field, the magnitude of the nonlinear coefficient decreases and almost becomes zero as we reach the quantum limit. At this point, the chemical potential crosses the lowest LL at large momenta. Here, the dispersion of the lowest LL is almost linear and higher order derivatives and conductivities become small. Upon increasing the field further, the chemical potential moves closer to the bottom of the band where the dispersion deviates more from a linear slope. This leads to an increase in γ_3 but the effect is orders of magnitudes smaller than at low fields where multiple parabolic bands contribute to the conductivity. When working at fixed density, the quantum limit is reached at lower fields for a nodal line system with finite Δ compared to a Dirac system with $\Delta = 0$ as the flat band region of the lowest LL in the nodal line system can host a lot of states. This can be seen by the two dashed lines in Fig. 5.18 which shows the ratio of nonohmic coefficients $\gamma_3(B)/\gamma_3(B, \Delta = 0)$ for different Zeeman couplings. Starting with the experimentally relevant case of $g = 2$ we see that the nonlinear response is completely dominated by the flat band of the nodal line system. Combining the flat band-induced enhancement with the reduction of nonlinearities in the Dirac system leads to a sharp rise of their respective ratio. Even when both systems are deep in the quantum limit, γ_3 is four orders of magnitude larger for the nodal line system. For small g-factors, the nonohmic coefficient can therefore be used to distinguish a nodal line from a Dirac material by looking at their transport properties.

We have seen previously that the flat band is quite sensitive to the strength of the Zeeman coupling. In the Dirac system, a larger g-factor increases the gap at $k = 0$ and makes the lowest LL more parabolic. Looking at the ratio of nonlinear coefficients for $g = 10$ we

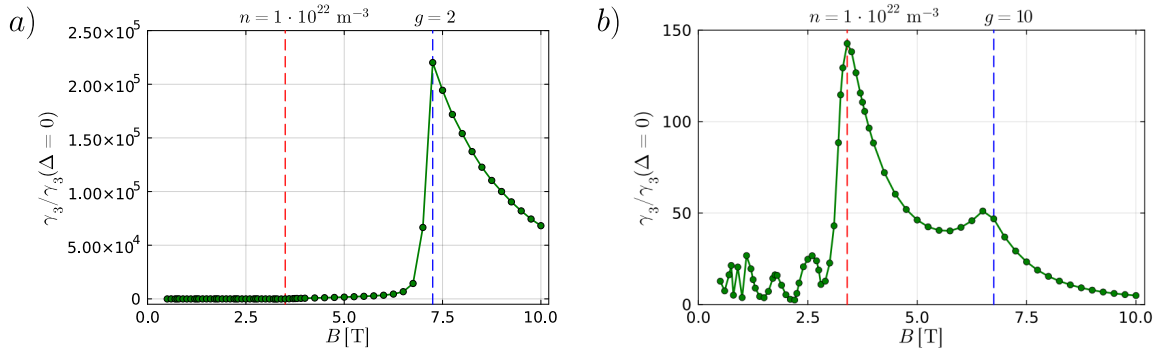

Figure 5.18: **Ratio of nonohmic coefficients for nodal line and Dirac:** The red dashed line indicates the field at which the nodal line system reaches the quantum limit while the lowest LL for the Dirac system is reached at the blue line. a) For small Zeeman coupling, the nonlinear response is completely dominated by the flat band of the nodal line system. b) Increasing the Zeeman coupling reduces the impact of the flat band region. We see two peaks when the systems reach their lowest LL and at high fields there is no enhancement due to the symmetry breaking term.

see a much smaller enhancement due to the flat-band region. After the lowest LL for the nodal line is reached, both numerator and denominator decrease as a function of field, leading to a second peak once the Dirac system reaches the quantum limit. When both systems are deep in the quantum limit, the ratio of nonohmic coefficients is of $\mathcal{O}(1)$.

6 Parallel-field Hall effect

In a conventional Hall effect setting, the electric current $\boldsymbol{I}$ and magnetic field $\boldsymbol{B}$ are applied perpendicular to each other and the resulting Hall voltage drop $\boldsymbol{E}_H$ is measured in perpendicular direction to both, meaning $\boldsymbol{I} \perp \boldsymbol{B} \perp \boldsymbol{E}_H$. For a single band, the conventional Hall resistivity due to Lorentz force is linear in the magnetic field and inversely proportional to the charge density $\rho_{xy} = B/(ne)$. Besides that, one can also consider an in-plane configuration where the Hall voltage is measured in the plane spanned by current and magnetic field. Such an effect can not be understood simply from a Lorentz force acting on the electrons as such a force is always perpendicular to the applied fields. Therefore, a finite response in this setup is referred to as an **unconventional** Hall effect. One possible mechanism can be due to a finite out-of-plane Berry curvature. In this case, the electrons aquire an anomalous velocity and the corresponding Hall conductivity is given by

$$\sigma_{xy}^{\text{anom}} = e^2 \int \frac{\mathrm{d}^3 k}{(2\pi)^3} \Omega_z(\boldsymbol{k}) f_0(\boldsymbol{k}), \tag{6.1}$$

where $\Omega_z(\boldsymbol{k})$ is the out-of-plane component of the Berry curvature and $f_0(\boldsymbol{k})$ is the equilibrium distribution function of electrons. For this integral to give a finite contribution some symmetry breaking is required. Otherwise, the averaged Berry curvature over the Fermi volume will be zero. For example, in a magnetic field time-reversal symmetry is absent and the integral in Eq. (6.1) can give a finite result. This anomalous Hall conductivity is independent of the transport scattering time τ_{tr} in contrast to the ordinary Hall effect from orbital contributions which follows $\sigma_{xy} \sim \tau_{\text{tr}}^2$.
For the in-plane configuration one should distinguish two cases depending on how the Hall resistivity $\rho_{xy}(B)$ behaves when reversing the magnetic field. If the response is symmetric with respect to B, meaning $\rho_{xy}^{\text{sym}}(-B) = \rho_{xy}^{\text{sym}}(B)$, one speaks of a planar Hall effect. It can be understood due to resistivity anisotropies and was seen e.g. in topological insulators [64–66]. On the other hand, there is the "true" unconventional Hall resistivity which is anti-symmetric in the magnetic field with $\rho_{xy}^{\text{antisym}}(-B) = -\rho_{xy}^{\text{antisym}}(B)$. Such a response can be a useful probe of the topology and symmetries of a material.
In the following, we will consider the unconventional Hall effect in $ZrTe_5$ for a magnetic field in the plane spanned by $\boldsymbol{I}, \boldsymbol{E}_H$ with $\boldsymbol{I} \perp \boldsymbol{E}_H$. We will present an alternative explanation for the Hall response besides the anomalous Hall effect generated by Berry curvature outlined above. The existence of such a Hall resistivity will give us insight into additional broken symmetries of the system.
This chapter is based on the preprint: "Parallel-Field Hall effect in $ZrTe_5$" [52].

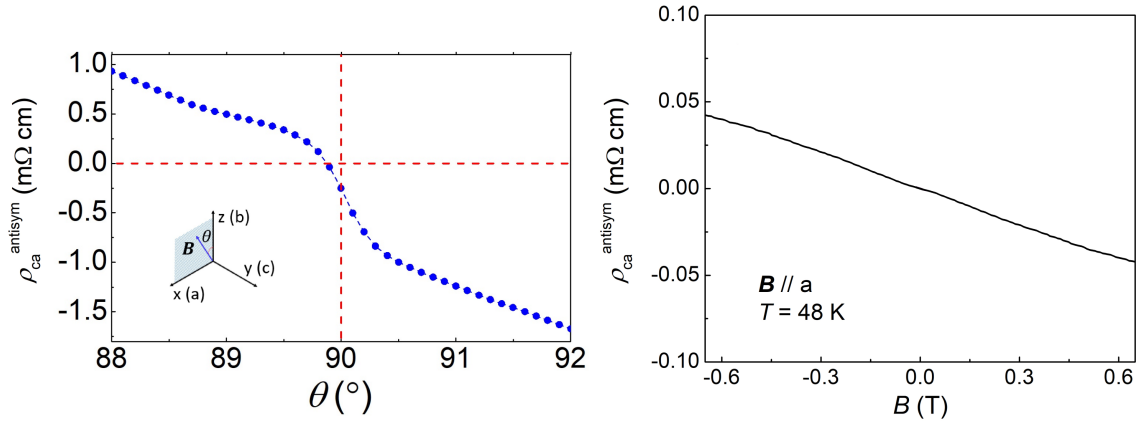

Figure 6.1: **Parallel-field Hall effect in** $ZrTe_5$**:** a) Antisymmetric Hall resistivity $\rho_{xy}^{\text{antisym}}$ as a function of field rotation angle in the ab-plane. At 90°, which corresponds to $\boldsymbol{B} \parallel \hat{a}$, there is a clear finite signal. b) The parallel-field Hall effect is linear in B for small magnetic fields. Figures taken from the preprint [52].

6.1 Experiments and additional symmetry breaking

The extreme case of a **parallel-field** configuration with current and magnetic field pointing in the same direction is of high interest as in this setting a Hall response $\boldsymbol{E}_H$ with $\boldsymbol{I} \parallel \boldsymbol{B} \perp \boldsymbol{E}_H$ is forbidden for most symmetry classes. Fig. 6.1 shows experimental data of the Hall resistivity $\rho_{ca}^{\text{antisym}}$ for a magnetic field rotated in the ab-plane. At $\theta = 90°$ the magnetic field is parallel to the injected current and a clear finite Hall signal is observed. For $\boldsymbol{I}, \boldsymbol{B}$ along the a-direction the parallel-field Hall effect induces an electric field along the c-direction which is linear in current and magnetic field $E_c \sim I_a B_a$, see Fig. 6.1 b). This response requires the mirror symmetry m_{ac} to be broken as this transformation maps $B_a \to -B_a$, while leaving the electric field and current invariant. Additionally, these transport measurements require m_{bc} to be broken. For this mirror-plane the current gets reversed $I_a \to -I_a$ but electric and magnetic field remain unchanged. Combining these arguments with the symmetry analysis of the magnetochiral anisotropy from chapter 3.2 we conclude that all three mirror symmetries are broken in $ZrTe_5$ samples which show a peak in the longitudinal resistivity at $T = 0$. In the next chapter we will include additional terms in our Hamiltonian to describe the fully symmetry broken system.

The measured resistivity has both a symmetric as well as an antisymmetric component which are shown in Fig. 6.2. At the largest fields of $B = 8$ T the symmetric component is about one order of magnitude smaller than the antisymmetric contribution. Upon rotating the magnetic field in the ac-plane, as shown in the inset of Fig. 6.2 c), ρ_{ca}^{sym} takes on its smallest value at $\varphi = 0°$ where $\boldsymbol{I} \parallel \boldsymbol{B}$. Additionally, the symmetric part of the resistivity follows a $\sin(2\varphi)$ behavior as expected for the planar Hall effect [64]. On the other hand, the antisymmetric part $\rho_{ca}^{\text{antisym}}$ is largest in the parallel-field configuration and changes sign upon rotating the field. Performing these measurements requires careful magnetic

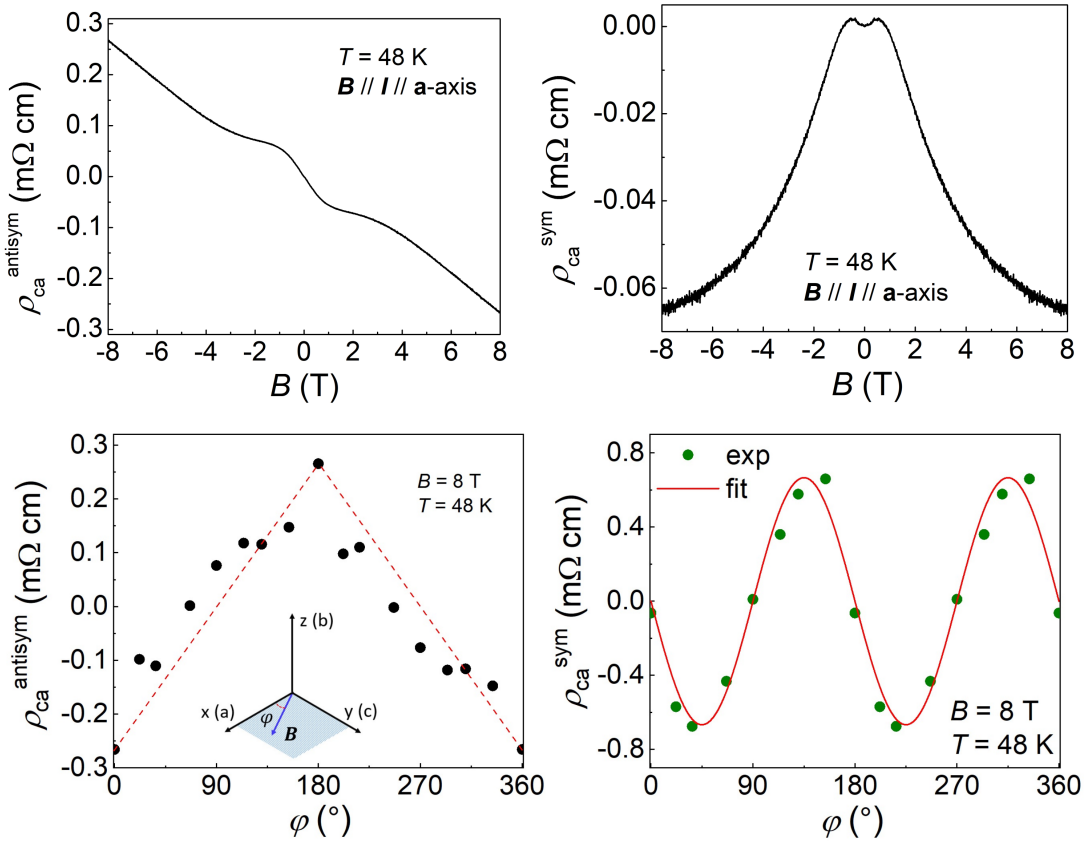

Figure 6.2: **Symmetric and antisymmetric Hall resistivity in** $ZrTe_5$**:** a) For the parallel-field configuration the antisymmetric Hall component is about one order of magnitude larger than the symmetric part of the resistivity. b) Resistivity for magnetic field rotated in the ac-plane with fixed magnitude of 8 T. The antisymmetric part is maximal for $\boldsymbol{B} \parallel \hat{a}$ while the symmetric component takes on its minimal value in this direction. The red line indicates a $\sin(2\varphi)$ behavior which is expected for the planar Hall effect. Data is taken between 0° and 154° and reused for angles $> 180°$ as B at $\varphi + 180°$ is the same as $-B$ at φ. Figures taken from the preprint [52].

field alignment as a small out-of-plane field can induce a large Hall response.

In the following, we will include the additional symmetry breaking into our model describing $ZrTe_5$ and use it to calculate a quantitative estimate of the parallel-field Hall resistivity.

6.2 Nodal lines in fully symmetry broken systems

In chapter 3.3 we derived the Hamiltonian for $ZrTe_5$ with broken inversion symmetry as well as the absence of mirror planes m_{ab} and m_{ac}. For the additional experiments on the parallel-field Hall effect, the required symmetry is reduced even further. Taking all experimental findings into account, one finds four possible symmetry-breaking terms that can be added to the fully-symmetric Hamiltonian H_0 from Eq. (3.2). These are

$$\Delta H = \Delta \mathbb{1} \otimes \tau_x + \xi \sigma_x \otimes \tau_y + \eta \sigma_z \otimes \tau_y + \lambda \sigma_y \otimes \tau_y, \tag{6.2}$$

where the first three terms break m_{ab}, m_{ac}, m_{bc}, respectively, and the last term breaks all three mirror symmetries. Here, we have only considered constant terms, each with its own energy scale. After rescaling the momenta $k_i \to k_i/(\hbar v_i)$, the energy eigenvalues of $H = H_0 + \Delta H$ are

$$\epsilon_{\boldsymbol{k}} = \pm\sqrt{\epsilon_{\text{sym}} \pm 2\epsilon_{\text{mixed}}}, \tag{6.3}$$

with

$$\epsilon_{\text{sym}} = k_a^2 + k_b^2 + k_c^2 + m^2 + \Delta^2 + \xi^2 + \eta^2 + \lambda^2 \tag{6.4}$$

$$\epsilon_{\text{mixed}} = \sqrt{k_a^2\,(\Delta^2 + \lambda^2 + \xi^2) + 2\eta k_a(k_b\xi - \Delta k_c) + k_b^2\,(\Delta^2 + \eta^2 + \lambda^2) + 2\Delta k_b k_c \xi + k_c^2\,(\eta^2 + \lambda^2 + \xi^2)}.$$

The spectrum of $H = H_0 + \Delta H$ contains a rotation-symmetric part $\epsilon_{\text{sym}} \sim (k_a^2 + k_b^2 + k_c^2)$ and mixed terms ϵ_{mixed}. To simplify these lengthy expressions we transform to the principal axes. This transformation can be written as

$$\begin{pmatrix} k_a \\ k_c \\ k_b \end{pmatrix} = U^T \begin{pmatrix} q_x \\ q_y \\ q_z \end{pmatrix}, \tag{6.5}$$

where the columns of the transformation matrix U are the normalized eigenvectors of the Hessian matrix $\frac{\partial^2 \epsilon_{\text{mixed}}^2}{\partial k_i \partial k_j}$. Two eigenvalues of this Hessian are degenerate and therefore we need to choose linear combinations of the corresponding eigenvectors such that the columns of U form an ONB. After this transformation, the energies in the new principal coordinates read

$$\epsilon_{\boldsymbol{q}} = \pm\sqrt{q_x^2 + q_y^2 + q_z^2 + m^2 + \Delta^2 + \xi^2 + \eta^2 + \lambda^2 \pm 2\sqrt{q_y^2\lambda^2 + (q_x^2 + q_z^2)\cdot(\Delta^2 + \xi^2 + \eta^2 + \lambda^2)}},$$

where in the symmetric part ϵ_{sym} we only replace $k_i \to q_i$ as expected. In the mixed term we see that even in the principal coordinates a remaining symmetry between $q_x \leftrightarrow q_z$ emerges. To show that we still have a nodal line we remark that $\epsilon_{\text{sym}}(\boldsymbol{q}) > 0$ for all momenta. A crossing of two bands is therefore only possible if $q_y = 0$, which defines the nodal line plane. In this plane we can define polar coordinates $q_x = q\,\cos(\theta)$, $q_z = q\,\sin(\theta)$ and combine the four symmetry-breaking energy scales into a single quantity $\tilde{\Delta}^2 = \Delta^2 + \xi^2 + \eta^2 + \lambda^2$ which results in 1d energy bands independent of the polar angle θ

$$\epsilon_q(q_a = 0) = \pm\sqrt{m^2 + q^2 + \tilde{\Delta}^2 \pm 2q\tilde{\Delta}} = \pm\sqrt{m^2 + (q \pm \tilde{\Delta})^2}. \tag{6.6}$$

Therefore, we can obtain for $m = 0$ a touching of two bands at $q = \tilde{\Delta}$ for all angles θ and thus again have a nodal line in the plane defined by $q_y = 0$. The orientation of this plane as well as the radius of the nodal line will depend on the four symmetry-breaking energy scales $\Delta, \xi, \eta, \lambda$. In conclusion, even when all three mirror symmetries are broken the band structure will still contain a nodal line which still has the same transport properties as our original model (3.3) but now in a rotated coordinate system compared to the original crystallographic momenta.

6.3 Conductivity tensor in different coordinate systems

As established in the previous chapter, the Fermi surface does not align perfectly with the crystallographic axes. Therefore, we are dealing with two different coordinate systems which are shown in Fig. 6.3 a). On the one hand, experiments are performed with respect to the *acb*-coordinates of the $ZrTe_5$ crystal. Additionally, we have the eigenbasis of the toroidal Fermi surface which will be labeled with xyz. These two reference frames are related by a rotation matrix, where we make the ansatz

$$R(\alpha, \beta) = R_x(\alpha)R_y(\beta) = \begin{pmatrix} \cos(\beta) & 0 & \sin(\beta) \\ \sin(\alpha)\,\sin(\beta) & \cos(\alpha) & -\sin(\alpha)\,\cos(\beta) \\ -\cos(\alpha)\,\sin(\beta) & \sin(\beta) & \cos(\alpha)\,\cos(\beta) \end{pmatrix} \tag{6.7}$$

with R_x, R_y being the rotation matrices around the x- and y-axes, respectively. An illustration of the angles α, β as projections in the *bc*- and *ab*-plane is shown in Fig. 6.3 b).

In the absence of a magnetic field the conductivity tensor in the eigenbasis of the Fermi surface is diagonal while in the crystallographic coordinates every entry of the tensor can be finite

$$\sigma^E(B=0) = \begin{pmatrix} \sigma_{xx} & 0 & 0 \\ 0 & \sigma_{yy} & 0 \\ 0 & 0 & \sigma_{zz} \end{pmatrix}, \qquad \sigma^C(B=0) = \begin{pmatrix} \sigma_{aa} & \sigma_{ac} & \sigma_{ab} \\ \sigma_{ca} & \sigma_{cc} & \sigma_{cb} \\ \sigma_{ba} & \sigma_{bc} & \sigma_{bb} \end{pmatrix}. \tag{6.8}$$

The Shubnikov-de Haas oscillations discussed in section 3.4 indicate that the misalignment between the principal axes of the toroidal Fermi surface and the crystallographic axes does not surpass 1° giving us an upper bound for the two rotation angles $\alpha, \beta \leq 1°$. In three dimensions rotation matrices do not commute and usually the order in which rotations around different axes are performed matters. In our case, where both rotation angles are small the deviation between the resulting matrices is negligible and we can assume $R_x(\alpha)R_y(\beta) \approx R_y(\beta)R_x(\alpha)$ for $\alpha, \beta \leq 1°$. Furthermore, an additional rotation around the z-axis could also be performed, expanding the zoo of possible rotation matrices. In the

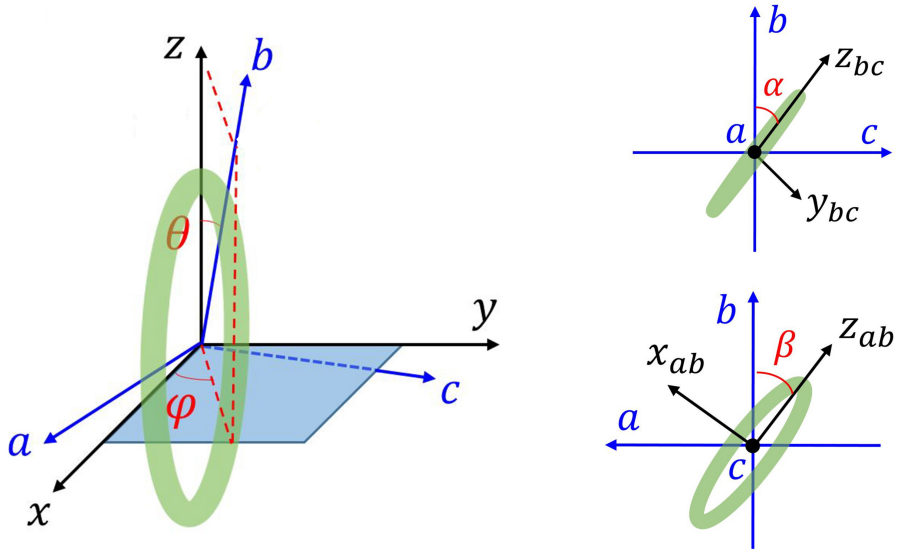

Figure 6.3: **Two different coordinate systems to explain the parallel-field Hall effect:** a) The crystallographic axes acb are shown in blue and the eigenbasis of the toroidal Fermi surface is a rotated coordinate system xyz. b) The angles α, β of the rotation matrix $R(\alpha, \beta)$ in Eq. (6.7) are shown as projections onto the bc- and ab-plane, respectively.

following, we will show that the ansatz (6.7) is sufficient to explain the experimental data but there might be other matrices which give the same result.

To calculate the Hall response in the experimental frame of reference we start from the eigenbasis of the Fermi surface where we just assume a conventional Hall response coming from orbital effects. As the difference between the two coordinate systems is small, the conductivity tensor for a magnetic field in a-direction can be written as

$$\sigma^E(B) \approx \begin{pmatrix} \sigma_{xx} & 0 & 0 \\ 0 & \sigma_{yy} & \sigma_{yz} \\ 0 & -\sigma_{yz} & \sigma_{zz} \end{pmatrix}. \tag{6.9}$$

By applying the rotation matrix to this tensor we obtain the conductivity in the crystallographic coordinates as $\sigma^C(B) = R(\alpha, \beta)\sigma^E(B)R^T(\alpha, \beta)$. To compare to the experimental data we need to invert the conductivity tensor and obtain the relevant Hall resistivity as

$$\rho^C_{ca} = \left[(\sigma^C)^{-1}\right]_{ca} \approx \frac{-\sigma_{yz}\,\sin(\beta) - \sigma_{yy}\,\sin(\alpha)\,\sin(\beta)}{\sigma_{yy}\sigma_{zz} + \sigma^2_{yz}} + \frac{\sin(\alpha)\,\sin(\beta)}{\sigma_{xx}}, \tag{6.10}$$

where we have neglected subleading terms $\sin^2(\alpha)$, $\sin^2(\beta)$ and used $\cos(\alpha) \approx \cos(\beta) \approx 1$. The diagonal components σ_{ii} are symmetric in B while σ_{yz} changes sign upon reversing the magnetic field. Hence, ρ^C_{ca} has both symmetric and antisymmetric components

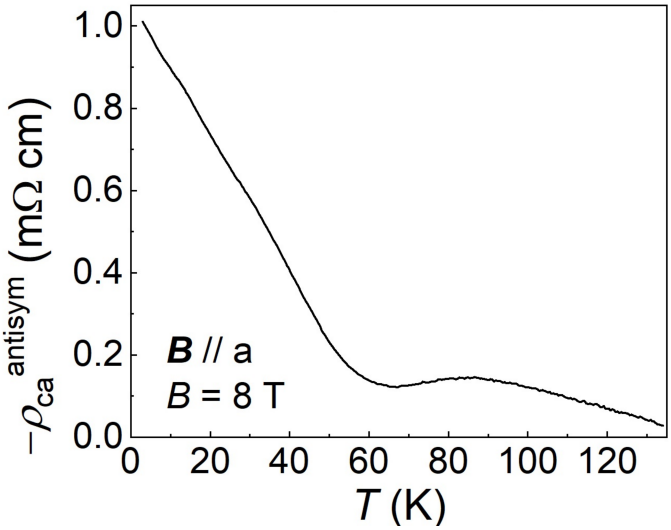

Figure 6.4: **Parallel-field Hall resistivity as a function of temperature:** For a small rotation angle $\beta = 0.3°$ the data at the smallest temperature $T = 2$ K can be explained from the ordinary Hall resistivity σ_{yz} in a rotated coordinate system. The decrease of the resistivity as a function of temperature is due to the shift in chemical potential. Figures taken from the preprint [52].

$$\rho_{ca}^{\text{antisym}}(B) \approx \frac{-\sigma_{yz}\,\sin(\beta)}{\sigma_{yy}\sigma_{zz}+\sigma_{yz}^2} = \rho_{yz}(B)\,\sin(\beta), \tag{6.11}$$

$$\rho_{ca}^{\text{sym}}(B) \approx \left(\frac{-\sigma_{yy}}{\sigma_{yy}\sigma_{zz}+\sigma_{yz}^2}+\frac{1}{\sigma_{xx}}\right)\sin(\alpha)\,\sin(\beta). \tag{6.12}$$

Therefore, the ordinary Hall conductivity σ_{yz} in combination with the rotated Fermi surface is the origin of the parallel-field Hall effect (6.11). Here, only the angle β for the rotation around the y-axis enters. The symmetric part of the resistivity contains both small angles α, β and therefore is about one order of magnitude smaller than $\rho_{ca}^{\text{antisym}}$, which is consistent with the experimental results from Fig. 6.2. To quantify the size of the antisymmetric resistivity we make an ansatz for the resisitivity in the eigencoordinates by just using the conventional Hall effect coming from Lorentz forces

$$\rho_{zy}(B) = \frac{B}{ne} \quad \Rightarrow \quad \rho_{yz}(B = 8\text{ T}) \approx -217\ \text{m}\Omega\text{cm} \tag{6.13}$$

where we used the density $n \approx 2.3 \cdot 10^{16}$ cm^{-3} obtained from quantum oscillations via Eq. (3.7). With this estimate of the resistivity in the eigencoordinates we can fit the experimental data shown in Fig. 6.4 at the lowest temperature $T = 2$ K where the quantum oscillations and thus the density were measured. For an angle $\beta = 0.3°$ which sits nicely below the upper bound established earlier we match the experimental result $\rho_{ca}^{\text{antisym}}(B = 8\text{ T}, \beta = 0.3°) \approx -1.1$ mΩcm. With increasing temperature the chemical

potential changes which results in a decrease of the Hall resistivity.
In conclusion, we have seen that the existence of an antisymmetric parallel-field Hall effect is a strong indicator of symmetry breaking in a condensed matter system. In $ZrTe_5$ a sizable response can be obtained from just a small rotation of the toroidal Fermi surface. The quantitative estimate for such a rotation combined with the ordinary Hall effect fits the experimental data very well. Our calculation was performed without considering Berry curvatures. Therefore, the origin of an unconventional Hall effect must not always be due to topology but instead there can be a lot of possible mechanisms generating Hall responses in topological materials if the symmetry is sufficiently low.

7 Nonlocal transport

In usual two-point transport measurements current is injected through one contact and extracted via a second one. The resulting voltage drop between the two contacts is measured and used to calculate the resistance of the sample. A more sophisticated technique of a four-point measurement uses two additional voltage tips between the current contacts. This method gets rid of contact resistances and is mostly used to measure the resistivity of thin sheets. If there is a finite voltage drop (and thus a current flowing) outside of the area bound by the current contacts one speaks of *nonlocal transport*. This can have multiple origins, e.g. due to the contact geometry resulting in curved equipotential lines. Such a mechanism can be easily understood by solving the Poisson equation with the contacts included. Additionally, the charge degree of freedom of the electrons can couple to other quantities, like for example spin, which are long lived, to enable nonlocal currents. Such effects can not be explained by a traditional semi-classical Boltzmann equation as interband coherence needs to be taken into account [67]. Possible mechanisms are either of intrinsic origin due to anomalous velocities from Berry curvatures or due to disorder effects like side-jump or skew scattering. Depending on the contact positions, surface states can also enable voltage drops away from the local region. To rule out any geometric effects from the contacts the clearest setup is one where the current is injected and extracted along line contacts spanning along the full width of the sample as seen in Fig. 7.1 a). In this case the equipotential lines are all parallel, straight lines and there is no voltage drop expected beyond the second contact. Even though a nonlocal response in this setup is unexpected, it was measured in $ZrTe_5$. Fig. 7.1 b) shows the nonlocal resistance as a function of distance from the contact where the current is extracted. The four data points are computed using the voltage drops in the nonlocal region via $R_{NL} = \frac{U_x - U_7}{I}$ with $x = (3, 4, 5, 6)$. Even for the furthest away contacts there is still a sizeable effect and the decay length of the nonlocal signal in the order of micrometers is much larger than expected for this geometry. Additionally, the nonlocal resistance is temperature- and magnetic field dependent but we will mainly focus on the zero-field response in the following. These experiments were also repeated at different locations on a very large sample with varying width. Thus, it was possible to extract the decay length λ for different sample width w and the two quantities follow a linear relation $\lambda(w) \sim w$. This needs to be an essential feature of any theory trying to describe the origin of nonlocal response in $ZrTe_5$.

In the following sections we will develop a model of coupled charge and spin transport and use a resistor network model to compute the nonlocal response due to the spin Hall

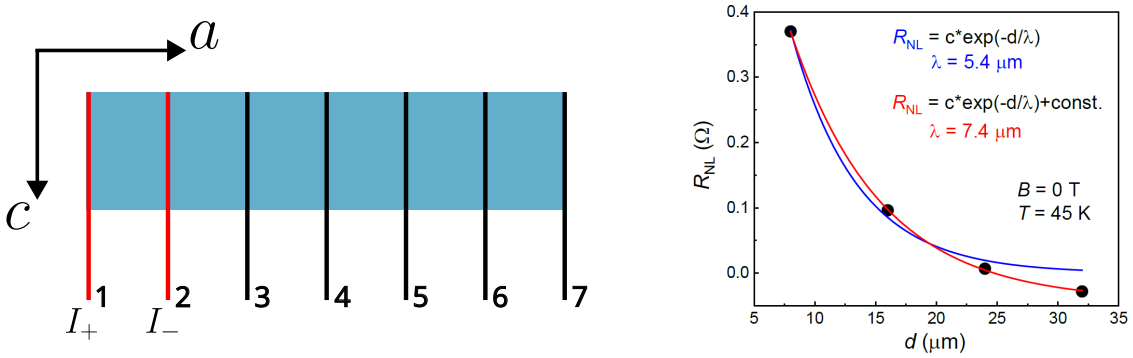

Figure 7.1: **Nonlocal transport in** $ZrTe_5$**:** a) Contact geometry for the measurement. The current is injected between contacts 1 and 2 while the nonlocal response is measured via contacts 3-7. b) Nonlocal resistance as a function of distance from contact 2 calculated by the voltage drops $\Delta U = U_x - U_7$ with $x = (3, 4, 5, 6)$. The decay length is of the order of micrometers and much larger than expected for this geometry.

effect. Additionally, it has to be checked that spin decays on a different time scale than the charge excitations of the systems to explain the sizable decay lengths in $ZrTe_5$.

7.1 Spin Hall effects

The goal of this section is to derive the phenomenological equations governing the coupling of charge and spin degrees of freedom and their currents [68]. For the electrical current we have

$$\boldsymbol{j}^{(0)} = \mu n e \boldsymbol{E} + eD\boldsymbol{\nabla} n, \tag{7.1}$$

which is the usual drift-diffusion equation of electrons with mobility μ, density n, and diffusion constant D. While the charge current is given by a 3d vector, the spin current instead has 2 indices as spin itself has three components which all can flow in each space direction. The j-component of the spin flowing in direction i is given by

$$q_{ij}^{(0)} = -\mu E_i P_j - D\frac{\partial P_j}{\partial x_i}, \tag{7.2}$$

where $\boldsymbol{P}$ is the spin polarization vector. In the presence of spin-orbit coupling both currents become modified and we have

$$j_i = j_i^{(0)} - \gamma e \epsilon_{ijk} q_{jk}^{(0)}, \qquad q_{ij} = q_{ij}^{(0)} + \gamma \epsilon_{ijk} j_k^{(0)}/e, \tag{7.3}$$

where γ indicates the size of the interaction. The sign difference between the two coupling terms is due to the different transformation behavior of spin and charge currents under

time-reversal. By inserting the uncoupled currents (7.1) and (7.2) we obtain

$$\boldsymbol{j}/e = \mu n \boldsymbol{E} + D\boldsymbol{\nabla} n + \gamma\mu \boldsymbol{E} \times \boldsymbol{P} + \gamma D \boldsymbol{\nabla} \times \boldsymbol{P}, \tag{7.4}$$

$$q_{ij} = -\mu E_i P_j - D\frac{\partial P_j}{\partial x_i} + \gamma \epsilon_{ijk} \left(\mu n E_k + D\frac{\partial n}{\partial x_k} \right). \tag{7.5}$$

These phenomenological equations describe multiple consequences of spin-charge coupling. The term $j_{AH} = \gamma\mu \boldsymbol{E} \times \boldsymbol{P}$ is the anomalous Hall effect where a Hall voltage is generated due to a magnetization. Here, the spin polarization can be either intrinsic (e.g. ferromagnetic order) or induced by an external field. For our theory of nonlocal transport the spin Hall effect term $q_{ij}^{SH} = \gamma\mu n \epsilon_{ijk} E_k$ will be of central importance. Here, an electric current induces a transverse spin current. This leads to spin accumulation at the sample boundaries. The textbook example for this effect are platinum wires [69] with coupling strength $\gamma_{Pt} \approx 10^{-3}$. The opposite effect is governed by the term $j_{SH} = \gamma D \boldsymbol{\nabla} \times \boldsymbol{P}$ where an transverse electric current is generated by a spatially inhomogeneous spin density. This is known as the inverse spin Hall effect. To solve these equations we additionally need the continuity equations for charge and the spin polarization

$$\frac{\partial \rho}{\partial t} + \boldsymbol{\nabla} \cdot \boldsymbol{j} = 0, \tag{7.6}$$

$$\frac{\partial P_j}{\partial t} + \frac{\partial q_{ij}}{\partial x_i} + \frac{P_j}{\tau_s} = 0, \tag{7.7}$$

with the charge density $\rho = ne$ and the spin relaxation time τ_s. The additional term for the spin polarization is needed as spin is not conserved and can decay. On the other hand, the total charge is, of course, still conserved in the presence of spin-orbit interactions.

In the presence of a magnetic field or if symmetries of the system are broken, additional couplings are allowed. In those cases, the charge current and the spin polarization are related by a general second-rank tensor $j_i = Q_{ik} P_k$. It should be noted that $\boldsymbol{j}$ is a polar vector while $\boldsymbol{P}$ is an axial vector (or pseudo-vector). One possible consequence is that, outside of equilibrium, a uniform spin polarization can create both charge and spin currents.

These equations allows us to formulate a possible mechanism for the origin of nonlocal transport. As the injected current induces a spin polarization via the spin Hall effect, there will be an accumulation of spin up/down at the two sides of the sample as seen in Fig. 7.2. This spin polarization diffuses along the sample and leads to a spin texture far away from the initial contacts. In this region the inverse spin Hall effect generates a nonlocal current which flows in the same direction as the original external current. The sample width sets a natural length scale for the breakdown of the nonlocal response as the two spin polarizations mix once they meet in the middle of the sample bulk. Therefore,

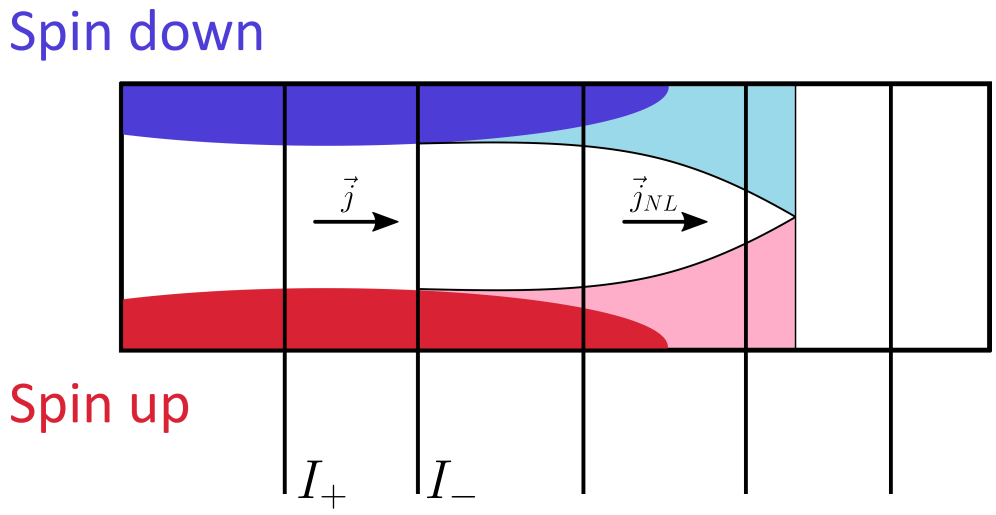

Figure 7.2: **Nonlocal transport due to spin Hall effect:** The injected current induces a spin polarization due to the spin Hall effect. The spin diffuses which leads to a spin texture far away from the initial contacts. The inverse Hall effect causes a nonlocal current to flow. The width of the sample sets a length scale for the breakdown of this mechanism as here the two spin polarizations mix again.

no current is expected once this length scale is reached. All steps in this explanation are governed by the same parameter γ. As the low-energy Hamiltonian of $ZrTe_5$ is a four-band model with two degrees of freedom for both spin and orbital we expect a large spin-orbit coupling constant. To validate this mechanism we set up a network model similar to the resistor network in section 4.3. Now, each node carries a voltage $\phi(\boldsymbol{r})$ as well as a spin polarization vector $\boldsymbol{P}(\boldsymbol{r})$. The local electric fields, which enter our phenomenological equations, is the gradient of the potential $\boldsymbol{E}(\boldsymbol{r}) = -\boldsymbol{\nabla}\phi(\boldsymbol{r})$. Because the symmetries of our system are strongly violated, we first need to rescale space to obtain an approximate rotational symmetry. This allows us to use the previously derived equations of spin-charge coupling in the rescaled coordinates.

We now list a few assumptions to simplify the equations 7.4 and 7.5 as well as conservation laws 7.6 and 7.7 which we discretize onto the network

1. Constant charge density $\rho = ne = \text{const.} \implies$ drop $\boldsymbol{\nabla} n$ terms.

2. System is in steady state $\implies$ no time derivatives in continuity equations.

3. Spin polarization is generated by the electric field $\implies$ ignore $E_i P_j$ terms as they are 2nd order.

4. 2d network with the spin polarization perpendicular to the plane (due to symmetry) $\implies$ spatial directions are $\hat{x}, \hat{y}$ and only spin component P_z is finite.

Under these assumptions, the linear equations for spin and charge conservation become

$$\frac{\partial j_x}{\partial x} + \frac{\partial j_y}{\partial y} = 0, \qquad \frac{\partial q_{iz}}{\partial x_i} + \frac{P_z}{\tau_s} = 0, \tag{7.8}$$

where the currents are given by

$$j_i = -\sigma \frac{\partial \phi}{\partial x_i} + \gamma D \epsilon_{ijz} \frac{\partial P_z}{\partial x_j}, \tag{7.9}$$

$$q_{iz} = -D \frac{\partial P_z}{\partial x_i} - \gamma \epsilon_{izk} \sigma \frac{\partial \phi}{\partial x_k} / e. \tag{7.10}$$

Additionally, we assume that the spin decay length $l_s \sim \sqrt{\frac{D}{\tau_s}}$ is much larger than the system size. In units of the discretization steps of the network we thus choose a large spin relaxation time $\tau_s \approx 100$. In the next section we will investigate if this is true for our nodal line Hamiltonian of $ZrTe_5$ by calculating the spin decay rates due to impurities. Obtaining the voltage and spin profiles of the network is done by combining all continuity equations into a single matrix-vector equation and performing matrix inversion. As a boundary condition the voltages at the contacts are kept fixed. As we are working with open boundary conditions spin up/down polarization accumulate on the two sides of the sample as seen in Fig. 7.3 due to the spin Hall effect. A cut along the x-direction at the bottom edge of the network nicely shows the spin profile which takes on its maximum value in the middle between the contacts. Due to the open boundary conditions there is a finite spin polarization even at $x = 0$. This edge of the sample is very close to the contacts and thus the spin can not relax much before the system terminates. In the other direction spin can defuse deeply into the system while decaying slowly. Even at the sample edge far away from the contacts at $x = L_x$ there is still some spin polarization left. Because of the inverse spin Hall effect, this spin polarization also generates a transversal current. We compare the voltage profiles with and without spin-charge coupling in Fig. 7.4. In both cases, the voltages at the initial contacts was fixed such that a total current I_{tot} flows between them. For $\gamma = 0$ there is no inverse spin Hall effect and the potential is constant in the region outside the contacts. Therefore, no nonlocal current flows in this scenario. For a finite spin-orbit interaction the voltage in the nonlocal region is no longer constant and acquires a space dependence $\phi(x)$ which leads to finite currents. Note that additional contacts used to measure the nonlocal voltage result in small dips of the potential as can be seen at $x = 20$ and $x = 25$ in Fig. 7.4. In between the contacts the voltage drops linearly as a function of x as expected. The difference in the height of the potentials at the first contact is due to fixing the applied current I_{tot} and the inverse Hall effect also contributing in between the contacts. To extract the decay length of the nonlocal voltage we set up a larger network with the same geometry as the experiment shown in Fig. 7.1. After subtracting the potential ϕ_7 at the last contact we can compute the length scale by

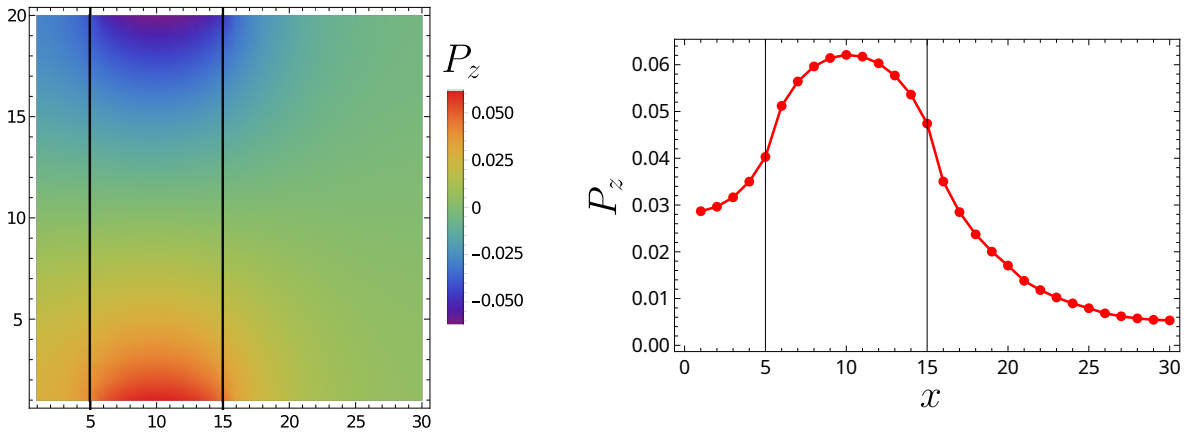

Figure 7.3: **Spin polarization in a spin Hall network:** a) Density plot of the spin z-component where the voltage contacts are indicated by the black lines. The spin accumulates at the two sample edges. b) Cut along the bottom edge of the sample. The largest spin polarization is reached in the middle between the two contacts. Away from the contacts the spin decays but there is still a finite spin component at the sample edge far away from the contacts at $x = 30$. Results are obtained for coupling strength $\gamma = 0.5$.

fitting

$$\phi_{\mathrm{NL}}(x) = \phi_0 \mathrm{e}^{-x/\lambda} \tag{7.11}$$

in the nonlocal region. The potential ϕ_0 is the voltage applied to get the local current I_{tot}. The result for a spin-orbit coupling strength $\gamma = 0.5$ can be seen in Fig. 7.5 a) where we used the same parameters as the experiment, which shows a decay length $\lambda_{\mathrm{exp}} \approx 120\ \mu$m. Our fit gives $\lambda_{\mathrm{sim}} = 4.65$ in simulation units which corresponds to $\lambda_{\mathrm{sim}} = 97.5\ \mu$m after restoring physical units. Therefore, it seems plausible that the spin Hall effect (and its inverse effect) can lead to nonlocal voltages which decay on long length scales comparable with experimental findings. Additionally, the width of the sample sets a natural length scale for the breakdown of this effect as here the spin species mix. Hence, the decay length scales linear with the sample width $\lambda \sim w$. We have also investigated the amplitude of the nonlocal response $\phi_{\mathrm{NL}}/\phi_0$ for a second network with twice the width where ϕ_0 is the constant fitting parameter from Eq. (7.11). Both curves are shown in Fig. 7.5 b) and scale linear with width $\phi_{\mathrm{NL}}/\phi_0 \sim w$ close to the contacts. The voltage size at the second contact is given by the total current per width and thus $\phi_0 \sim I/w$. As a result, we expect the nonlocal resistance to not depend on the sample width $R_{\mathrm{NL}} = \phi_{\mathrm{NL}}/I \sim \mathcal{O}(w^0)$. In the experiments the amplitude of the nonlocal resistance does depend on the width and seems to be roughly $\sim 1/w^2$. Here, our theory clearly predicts a behavior that is not consistent with experiments. Another possible mechanism could be that the spin is carried by the surface states of $ZrTe_5$ and leaks into the bulk with a length scale $l_{\mathrm{leak}} \ll w$. Therefore, a nonlocal voltage drop would only be induced in a small part of the sample and we have $U_{\mathrm{NL}} \sim \frac{l_{\mathrm{leak}}}{w}\frac{I}{w}$. The corresponding nonlocal voltage $R_{\mathrm{NL}} \sim \frac{1}{w^2}$ would have the same width dependence as seen in the experiments. However, for this scenario the decay length

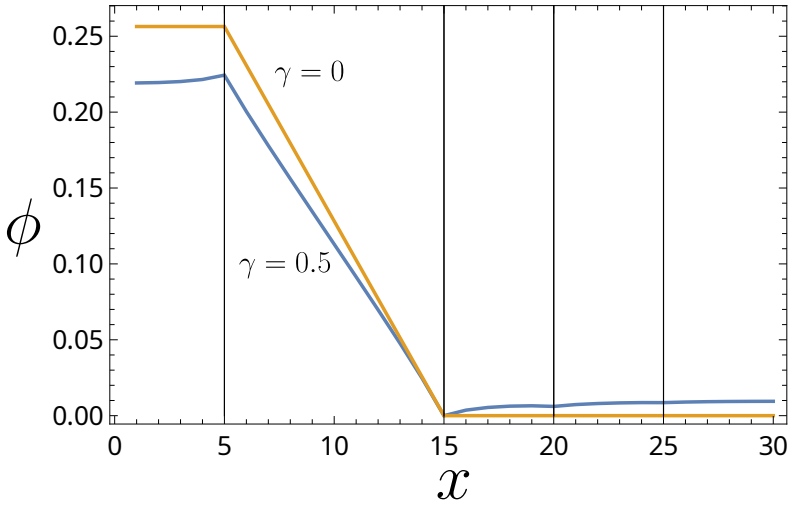

Figure 7.4: **Voltage profile with and without spin-orbit interactions (orange and blue line):** Voltages are fixed on the contacts at $x = 5$ and $x = 15$. Without spin-charge coupling ($\gamma = 0$) the potential outside of these contacts is constant. Between the two contacts the slope is constant as expected. Including the spin Hall effect (here with $\gamma = 0.5$) leads to a finite voltage drop and thus a current in the nonlocal region. The lines at $x = 20$ and $x = 25$ mark additional contacts used to measure the nonlocal voltage.

λ would be independent of the sample width as the spins only leak a little bit into the bulk and never mix like for the previous mechanism. As the experiments are performed using three-dimensional crystals and the contacts are just placed on the top side of the samples the current patterns in the bulk can be much more complicated due to the various Hall effects taking place in $ZrTe_5$. In this case the equipotential planes would be curved surfaces and a nonlocal voltage due to the contact geometry can build up. But such ohmic effects would result in much smaller nonlocal responses than what is actually measured. Additionally, the sample height would be a relevant length scale in this scenario but there has been no experimental evidence for this.

As mentioned before, spin is not a conserved quantity and our model is based around the assumption that spin decays on much larger length scales than the charge current. In the next sections we want to compute the spin decay rate due to impurities for our model of $ZrTe_5$ and look for other degrees of freedom with a long lifetime that couple to charge.

7.2 Spin decay rates

In the following, we will use the Hamiltonian (3.3) describing the low-energy physics of $ZrTe_5$. For $\xi = 0$ this describes a torus in the ab-plane with Hamiltonian

$$H = m\mathbb{1} \otimes \tau_z + \hbar\left(v_a k_a \sigma_z \otimes \tau_x + v_b k_b \sigma_x \otimes \tau_x + v_c k_c \mathbb{1} \otimes \tau_y\right) + \Delta\mathbb{1} \otimes \tau_x + \mu\mathbb{1}_4, \qquad (7.12)$$

where we include a small mass term $m < \mu < \Delta$. The dispersion is given by

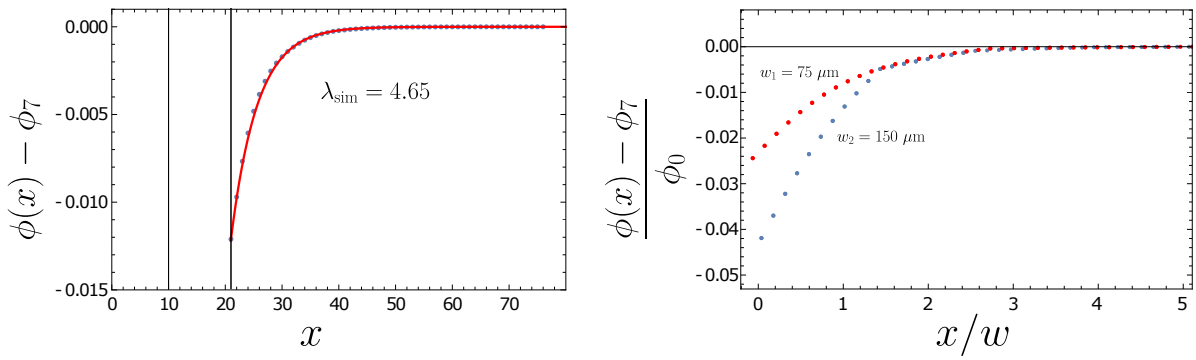

Figure 7.5: **Decay of the nonlocal voltage:** a) After subtracting the potential ϕ_7 at the last contact the nonlocal voltage can be fitted with an exponential decay. b) Nonlocal voltage for two samples with different widths.

$$\epsilon^{\pm}_{1,2} = \pm\sqrt{m^2 + (\hbar v_c k_c)^2 + \left(\sqrt{(\hbar v_a k_a)^2 + (\hbar v_b k_b)^2} \pm \Delta\right)^2}, \tag{7.13}$$

with a small mass gap around $\epsilon_k = 0$. In this regime we have one band at the Fermi energy with $H(\boldsymbol{k})\Psi_{\boldsymbol{k}} = \epsilon(\boldsymbol{k})\Psi_{\boldsymbol{k}}$ as shown in Fig. 7.6 a). In this section, we will parametrize the toroidal Fermi surface by two angles $\phi, \theta \in [0, 2\pi]$ as defined in Fig. 7.6 b). This allows us to write down a simple parametrization of the Fermi surface even in the presence of a mass term

$$f(\phi, \theta) = \begin{pmatrix} \Delta\,\cos(\phi) + \sqrt{\mu^2 - m^2}\,\cos(\theta)\cos(\phi) \\ \Delta\,\sin(\phi) + \sqrt{\mu^2 - m^2}\,\cos(\theta)\sin(\phi) \\ \sqrt{\mu^2 - m^2}\,\sin(\theta) \end{pmatrix}, \tag{7.14}$$

where Δ is the radius of the large circle and $\sqrt{\mu^2 - m^2}$ gives the smaller circle radius. Integrating over the volume of this torus gives us the charge density $n(\mu) = \frac{\Delta(\mu^2 - m^2)}{4\pi\hbar^3 v_a v_b v_c}$.

If a quantity Q is conserved, it commutes with the Hamiltonian $[H, Q] = 0$. The corresponding conductivity has a singular contribution at zero frequency showing a Drude peak $\mathrm{Re}[\sigma(\omega)] \sim \delta(\omega)$ [70]. Such an infinite conductivity is, of course, unphysical because in a real system the responses to external fields decay and become finite, e.g. due to impurity scattering. Therefore, the conservation law is broken and we have $i\hbar\partial_t Q = [gH_{\mathrm{imp}}, Q]$ where g is a small parameter quantifying impurity strength and therefore the size of the symmetry breaking. This broadens the Drude peak resulting in a finite conductivity at zero frequency. The scattering rate $\Gamma(\omega)$ gives us the width of the peak and is defined by

$$\sigma(\omega) = \beta\frac{\chi}{\Gamma(\omega)/\chi - i\omega} \tag{7.15}$$

with the inverse temperature β and the static susceptibility $\chi = \beta\langle Q, Q\rangle_{\omega=0}$. We can

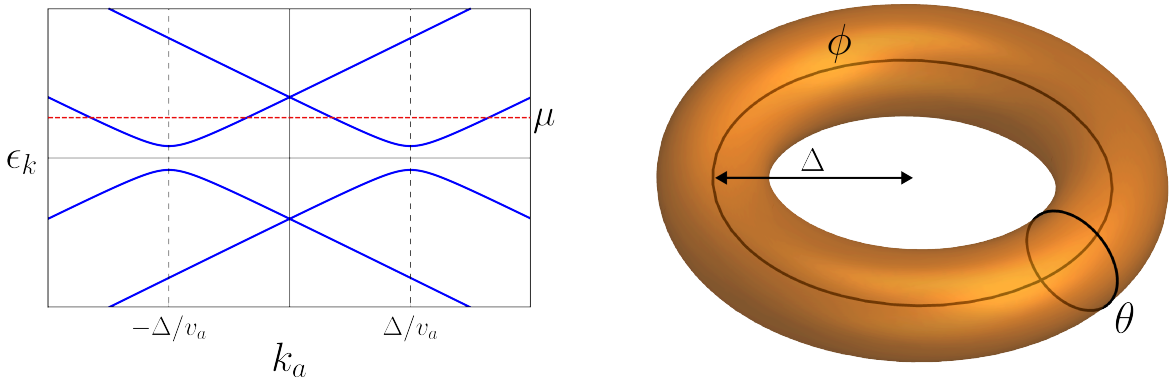

Figure 7.6: **Bandstructure and Fermi surface of the nodal line system:** a) 1d cut through the dispersion. The nodal line points at $\pm\Delta/v_a$ are gapped due to the mass term. For $m < \mu < \Delta$ we have one band crossing the Fermi energy (indicated in red). b) Torus Fermi surface for $m < \mu < \Delta$ parametrized by the two angles ϕ, θ.

compute the scattering rate in 2nd-order perturbation theory in g

$$\Gamma(\omega) = \frac{1}{\omega}\mathrm{Re}\int_0^\infty \mathrm{d}t\ \mathrm{e}^{i(\omega+i\epsilon)t}\langle[\partial_t Q(t), \partial_t Q(0)]\rangle_0 + \mathcal{O}(g^3). \tag{7.16}$$

As $\dot{Q}$ is linear in g it is sufficient to evaluate the expectation value $\langle ...\rangle_0$ only w.r.t. the conserved Hamiltonian H. This gives us the scattering rate from a simple correlation function. The physical decay rate of the quantity Q is then given by

$$\tilde{\Gamma} = \lim_{\omega\to 0}\Gamma(\omega)/\chi. \tag{7.17}$$

Now we want to apply this to our nodal line Hamiltonian (7.12). As we are interested in the decay rate of the spin we choose

$$Q_z = \sum_{\boldsymbol{k}}\langle\Psi_{\boldsymbol{k}}|\sigma_z\otimes\mathbb{1}|\Psi_{\boldsymbol{k}}\rangle c^\dagger_{\boldsymbol{k}}c_{\boldsymbol{k}} = \sum_{\boldsymbol{k}} A_{\boldsymbol{k}}c^\dagger_{\boldsymbol{k}}c_{\boldsymbol{k}}, \tag{7.18}$$

where $c_{\boldsymbol{k}}, c^\dagger_{\boldsymbol{k}}$ are annihilation and creation operators at momentum $\boldsymbol{k}$ for the band which defines the Fermi surface. The Hamiltonian for the impurities in real space is given by

$$H_{\mathrm{imp}} = \int V(\boldsymbol{r})\Psi^\dagger(\boldsymbol{r})\Psi(\boldsymbol{r})\mathrm{d}\boldsymbol{r}, \tag{7.19}$$

with delta-correlated impurity potential $\langle V(\boldsymbol{r})V(\boldsymbol{r}')\rangle = V_0^2\delta^3(\boldsymbol{r}-\boldsymbol{r}')$. Going to momentum space we write the creation operators as $\Psi^\dagger(\boldsymbol{r}) = \sum_{\boldsymbol{k}}\mathrm{e}^{i\boldsymbol{k}\cdot\boldsymbol{r}}\Psi_{\boldsymbol{k}}c^\dagger_{\boldsymbol{k}}$ and the potential becomes constant $\langle V(\boldsymbol{q})V(-\boldsymbol{q})\rangle = V_0^2$. Inserting this into Eq. (7.19) gives us the corresponding

Hamiltonian in momentum space

$$H_{\text{imp}} = \sum_{\boldsymbol{k},\boldsymbol{k}'} V_{\boldsymbol{k}-\boldsymbol{k}'} \Psi^*_{\boldsymbol{k}'} \Psi_{\boldsymbol{k}} c^\dagger_{\boldsymbol{k}} c_{\boldsymbol{k}'} = \sum_{\boldsymbol{k},\boldsymbol{k}'} B_{\boldsymbol{k},\boldsymbol{k}'} c^\dagger_{\boldsymbol{k}} c_{\boldsymbol{k}'}. \tag{7.20}$$

We first compute the susceptibility $\chi = \beta \langle Q, Q \rangle_{\omega=0}$ which is given by the integral

$$\chi = \int \frac{\mathrm{d}^3 k}{(2\pi)^3} \frac{n_F(\epsilon_{\boldsymbol{k}}) - n_F(\epsilon_{\boldsymbol{k}+\boldsymbol{q}})}{\epsilon_{\boldsymbol{k}} - \epsilon_{\boldsymbol{k}+\boldsymbol{q}}} A_{\boldsymbol{k}} A_{\boldsymbol{k}+\boldsymbol{q}}. \tag{7.21}$$

Performing a Taylor expansion around $\boldsymbol{q} = 0$ and working at $T = 0$ leads us to

$$\chi = \int \frac{\mathrm{d}^3 k}{(2\pi)^3} |A_{\boldsymbol{k}}|^2 \delta(\epsilon_{\boldsymbol{k}} - \mu) = \int\limits_{\mathcal{FS}} |A_{\boldsymbol{k}}|^2 \Omega(\phi, \theta) \frac{\mathrm{d}\phi \mathrm{d}\theta}{(2\pi)^3}. \tag{7.22}$$

For the second equal sign we have restricted the momentum integration to the Fermi surface because of the delta function and inserted our torus parametrization (7.14) with Jacobi determinant $\Omega(\phi, \theta) = \frac{(\mu^2 - m^2)\ \cos(\theta) + \Delta\sqrt{\mu^2 - m^2}}{v_a v_b v_c}$. The spin expectation value only depends on the angle ϕ around the big circle of the torus and can be easily computed as $A_{\boldsymbol{k}} = \langle \Psi_{\boldsymbol{k}} | \sigma_z \otimes \mathbb{1} | \Psi_{\boldsymbol{k}} \rangle = -\cos(\phi)$. Performing the integral (7.22) using these formulas we obtain

$$\chi\left(\hat{S}_z\right) = \frac{\Delta\sqrt{\mu^2 - m^2}}{4\pi v_a v_b v_c}. \tag{7.23}$$

To compute the scattering rate we need the time derivative $\dot{Q}_z$ and therefore compute the commutator

$$[H, Q] = \left[\sum_{\boldsymbol{k}} A_{\boldsymbol{k}} c^\dagger_{\boldsymbol{k}} c_{\boldsymbol{k}}, \sum_{\boldsymbol{k}',\boldsymbol{k}''} B_{\boldsymbol{k}'',\boldsymbol{k}'} c^\dagger_{\boldsymbol{k}''} c_{\boldsymbol{k}'} \right], \tag{7.24}$$

where it should be noted that $c_{\boldsymbol{k}}$ are fermionic operators that obey anti-commutation relations $\{c^\dagger_{\boldsymbol{k}}, c_{\boldsymbol{k}'}\} = \delta_{\boldsymbol{k},\boldsymbol{k}'}$. After a bit of algebra one obtains

$$i\hbar \partial_t Q_z = \sum_{\boldsymbol{k},\boldsymbol{k}'} M_{\boldsymbol{k},\boldsymbol{k}'} c^\dagger_{\boldsymbol{k}} c_{\boldsymbol{k}'}, \tag{7.25}$$

with $M_{\boldsymbol{k},\boldsymbol{k}'} = B_{\boldsymbol{k},\boldsymbol{k}'}(A_{\boldsymbol{k}} - A_{\boldsymbol{k}'})$. As we are interested in the DC limit $\omega \to 0$ we need to compute

$$\lim_{\omega\to 0} \Gamma(\omega) = \lim_{\omega\to 0} \frac{1}{\omega} \int \left(n_F(\epsilon_{\boldsymbol{k}}) - n_F(\epsilon_{\boldsymbol{k}'})\right) \delta(\omega - \epsilon_{\boldsymbol{k}} + \epsilon_{\boldsymbol{k}'}) |M_{\boldsymbol{k},\boldsymbol{k}'}|^2 \frac{\mathrm{d}^3 k}{(2\pi)^3} \frac{\mathrm{d}^3 k'}{(2\pi)^3}. \tag{7.26}$$

Due to the delta function one can replace $n_F(\epsilon_{\boldsymbol{k}'})$ by $n_F(\epsilon_{\boldsymbol{k}} - \omega)$. Therefore the difference in the two occupation functions is just $n_F(\epsilon_{\boldsymbol{k}}) - n_F(\epsilon_{\boldsymbol{k}'}) = \omega\ n'_F(\epsilon_{\boldsymbol{k}}) + \mathcal{O}(\omega^2)$. Taking the

limit $\omega \to 0$ all higher order terms vanish and for $T = 0$ we can write

$$\lim_{\omega\to 0}\Gamma(\omega) = \int \delta(\epsilon_{\boldsymbol{k}}-\mu)\delta(\epsilon_{\boldsymbol{k}'}-\mu)|M_{\boldsymbol{k},\boldsymbol{k}'}|^2\frac{\mathrm{d}^3k\mathrm{d}^3k'}{(2\pi)^6} = \int\limits_{\mathcal{FS}} |M_{\boldsymbol{k},\boldsymbol{k}'}|^2\Omega(\phi,\theta)\Omega(\phi',\theta')\frac{\mathrm{d}\phi\mathrm{d}\theta\mathrm{d}\phi'\mathrm{d}\theta'}{(2\pi)^6}, \tag{7.27}$$

where again we restrict the integration to the toroidal Fermi surface by evaluating the delta fucntions at the Fermi energy. The scattering matrix elements on the torus after impurity averaging are given by

$$|B_{\boldsymbol{k},\boldsymbol{k}'}|^2 = V_0^2|\Psi^*_{\boldsymbol{k}'}\Psi_{\boldsymbol{k}}|^2 = V_0^2\,\cos^2\left(\frac{\phi-\phi'}{2}\right)\left[\cos^2\left(\frac{\theta-\theta'}{2}\right)+\frac{m^2}{\mu^2}\sin^2\left(\frac{\theta-\theta'}{2}\right)\right], \tag{7.28}$$

where the second term only gives a small contribution as $m < \mu$. As expected, the matrix elements do only depend on the differences $\phi - \phi'$ and $\theta - \theta'$ between two momentum points on the torus. Using these in the formula for the decay rate (7.27) and dividing by the spin susceptibility (7.23) we end up with

$$\tilde{\Gamma}\left(\hat{S}_z\right) = V_0^2\frac{\left(\mu^2-m^2\right)^3+4\Delta\left(\mu^2-m^2\right)}{32\pi v_a v_b v_c\Delta\sqrt{\mu^2-m^2}}. \tag{7.29}$$

As a small sanity check one can inspect the physical dimension of $\tilde{\Gamma}$ and confirm that it is $\frac{1}{\text{time}}$ as needed for a decay rate. This spin decay rate needs to be compared to the decay rate of the velocity operator $\hat{v}_a = \frac{\partial H}{\partial k_a}$. Here, the relevant matrix elements are

$$\langle\Psi_{\boldsymbol{k}}|\sigma_z\otimes\tau_x|\Psi_{\boldsymbol{k}}\rangle = \frac{\sqrt{\mu^2-m^2}}{\mu}\,\cos(\phi)\,\cos(\theta). \tag{7.30}$$

Repeating the calculation from above gives us the decay rate of the current

$$\tilde{\Gamma}\left(\hat{v}_a\right) = V_0^2\frac{\sqrt{\mu^2-m^2}\left(\mu^4+6\mu^2(\Delta^2-m^2)+5(2m^2\Delta^2+m^4)\right)}{32\pi v_a v_b v_c\Delta\mu^2}. \tag{7.31}$$

The ratio of these rates in the experimentally relevant limit $m \to 0$ is just

$$\frac{\tilde{\Gamma}\left(\hat{S}_z\right)}{\tilde{\Gamma}\left(\hat{v}_a\right)} = \frac{(\mu^2-m^2)^2+4\Delta^2(\mu^2-m^2)}{\mu^4+6\mu^2(\Delta^2-m^2)+5(2m^2\Delta^2+m^4)} \overset{m\to 0}{=} \frac{\mu^2+4\Delta^2}{\mu^2+6\Delta^2} \approx 1. \tag{7.32}$$

This is quite a disappointing result as it means that the spin does not decay slow compared to other modes in the system. Therefore, our previous considerations of the spin Hall effect as the origin of nonlocal transport should be invalid as spin can not propagate to the nonlocal regions before decaying. Such a result is not too surprising as we are working with a Hamiltonian of four highly spin-orbit coupled bands. Thus, there is per se no reason for the two degrees of freedom to relax on different time scales. For sake of completeness

we also compute the decay rates for spin and velocity in the other two directions

1. Velocity in b-direction: $\langle\Psi_{\boldsymbol{k}}|\hat{v}_b|\Psi_{\boldsymbol{k}}\rangle \sim \langle\Psi_{\boldsymbol{k}}|\sigma_z \otimes \tau_x|\Psi_{\boldsymbol{k}}\rangle = \frac{\sqrt{\mu^2-m^2}}{\mu}\sin(\phi)\cos(\theta)$
   $\Rightarrow \tilde{\Gamma}(\hat{v}_b) = \tilde{\Gamma}(\hat{v}_a)$.
   Velocity anisotropies cancel out and the current in the torus plane decays the same independent of the direction.

2. Velocity in c-direction: $\langle\Psi_{\boldsymbol{k}}|\hat{v}_c|\Psi_{\boldsymbol{k}}\rangle \sim \langle\Psi_{\boldsymbol{k}}|\mathbb{1} \otimes \tau_y|\Psi_{\boldsymbol{k}}\rangle = -\frac{\sqrt{\mu^2-m^2}}{\mu}\sin(\theta)$
   $\Rightarrow \tilde{\Gamma}(\hat{v}_c) = V_0^2 \frac{\sqrt{\mu^2-m^2}\left(\mu^4+2\mu^2(2\Delta^2-m^2)+12m^2\Delta^2+m^4\right)}{32\pi v_a v_b v_c \Delta\mu^2}$.
   Decay rates parallel and perpendicular to the torus plane are only slightly different.

3. a-component of spin: $\langle\Psi_{\boldsymbol{k}}|\sigma_x \otimes \mathbb{1}|\Psi_{\boldsymbol{k}}\rangle = \sin(\phi) \Rightarrow \tilde{\Gamma}\left(\hat{S}_x\right) = \tilde{\Gamma}\left(\hat{S}_z\right)$.
   Only $|A_{\boldsymbol{k}}|^2$ enters the formulas and therefore both spin components have the same decay rate.

4. c-component of spin: $\langle\Psi_{\boldsymbol{k}}|\sigma_y \otimes \mathbb{1}|\Psi_{\boldsymbol{k}}\rangle = 0$.
   The expectation value of this spin component is zero at all momentum points due to the remaining symmetries.

Summarizing these calculations there is no spin component that decays slower than any of the current operators. In the next section we want to derive a formula for the decay rates in another way that allows us to find the slowest modes of our system.

7.3 Searching for slow modes

Our goal in this section is to use a variational approach to obtain the smallest decay rates and the corresponding modes as configurations in momentum space. Again, we restrict ourselves to only consider decay due to impurity scattering. We start from a Boltzmann-style equation for the change of a (conserved) quantity, which takes on values $A_{\boldsymbol{k}}$

$$\partial_t \left(\sum_{\boldsymbol{k}} A_{\boldsymbol{k}} f_{\boldsymbol{k}} \right) = - \sum_{\boldsymbol{k},\boldsymbol{k}'} A_{\boldsymbol{k}} W_{\boldsymbol{k}\boldsymbol{k}'} \left(f_{\boldsymbol{k}} - f_{\boldsymbol{k}'} \right), \tag{7.33}$$

with energy-conserving impurity scattering $W_{\boldsymbol{k}\boldsymbol{k}'} = \frac{2\pi}{\hbar}|\langle\Psi_{\boldsymbol{k}'}|V_{\text{imp}}|\Psi_{\boldsymbol{k}}\rangle|^2\delta(\epsilon_{\boldsymbol{k}} - \epsilon_{\boldsymbol{k}'})$. The matrix elements of the scattering matrix are the same as $B_{\boldsymbol{k},\boldsymbol{k}'}$ in the previous section. The Hamiltonian $H = H_0 + H_A$ consists of the dispersive part $H_0 = \sum_{\boldsymbol{k}} \epsilon_{\boldsymbol{k}} c_{\boldsymbol{k}}^\dagger c_{\boldsymbol{k}}$ and the term generating a finite expectation value of $A_{\boldsymbol{k}}$ via $H_A = \epsilon \sum_{\boldsymbol{k}} A_{\boldsymbol{k}} c_{\boldsymbol{k}}^\dagger c_{\boldsymbol{k}}$. The distribution function can therefore be written as

$$f_{\boldsymbol{k}} = f_0(\epsilon_{\boldsymbol{k}} + \epsilon A_{\boldsymbol{k}}) \approx f_0(\epsilon_{\boldsymbol{k}}) + \epsilon A_{\boldsymbol{k}} \frac{\partial f_0}{\partial \epsilon_{\boldsymbol{k}}}. \tag{7.34}$$

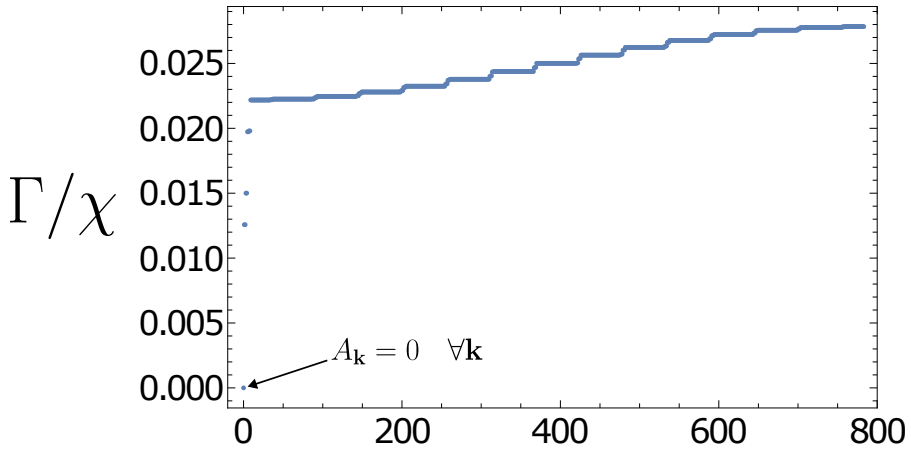

Figure 7.7: **Decay rates for the torus Fermi surface obtained by diagonalizing Eq.** (7.40)**:** The x-axis labels each eigenvalue. A vanishing decay rate is only seen for the mode with $A_{\boldsymbol{k}} = 0$ for all momenta. The smallest finite decay rates are only reduced by about a factor of 2 compared to the largest eigenvalues. Discretization of the torus was done with 800 momentum points.

Plugging this ansatz in Eq. (7.33) leads us again to a formula for the decay rate

$$\frac{\Gamma}{\chi} = \frac{\langle \partial_t A_{\boldsymbol{k}} \rangle}{\langle A_{\boldsymbol{k}}(0) \rangle} = \frac{\sum_{\boldsymbol{k},\boldsymbol{k}'} (A_{\boldsymbol{k}} - A_{\boldsymbol{k}'}) |B_{\boldsymbol{k},\boldsymbol{k}'}|^2 \delta(\epsilon_{\boldsymbol{k}} - \mu) \delta(\epsilon_{\boldsymbol{k}'} - \mu)}{\sum_{\boldsymbol{k}} |A_{\boldsymbol{k}}|^2 \delta(\epsilon_{\boldsymbol{k}} - \mu)}. \tag{7.35}$$

Here, we have used that $\sum_{\boldsymbol{k}} A_{\boldsymbol{k}} f_0(\epsilon_{\boldsymbol{k}}) = 0$ by definition as only the Hamiltonian H_A generates a finite $\langle A_{\boldsymbol{k}} \rangle$. Instead of making a choice for $A_{\boldsymbol{k}}$ we now want to minimize this expression w.r.t. $A_{\boldsymbol{k}}$ to find the slowest modes in the presence of impurity scattering. Thus, we look for zeros of the functional derivative

$$\frac{\delta}{\delta A_{\boldsymbol{k}}} \left(\frac{\Gamma}{\chi} \right) = 0 \quad \Longrightarrow \quad \frac{\delta \Gamma}{\delta A_{\boldsymbol{k}}} = \frac{\Gamma}{\chi} \frac{\delta \chi}{\delta A_{\boldsymbol{k}}}. \tag{7.36}$$

If we apply this to our nodal line Hamiltonian (7.12), where each point on the Fermi surface is labeled by the angles $\boldsymbol{\varphi} = (\phi, \theta)$, the functional derivatives are

$$\begin{aligned} \frac{\delta \Gamma}{\delta A(\boldsymbol{\varphi})} &= 4 \int \frac{\mathrm{d}\boldsymbol{\varphi}'}{(2\pi)^3} \left(A(\boldsymbol{\varphi}) - A(\boldsymbol{\varphi}') \right) |B(\boldsymbol{\varphi} - \boldsymbol{\varphi}')|^2 \Omega(\boldsymbol{\varphi}) \Omega(\boldsymbol{\varphi}'), \\ \frac{\delta \chi}{\delta A(\boldsymbol{\varphi})} &= 2 A(\boldsymbol{\varphi}) \Omega(\boldsymbol{\varphi}). \end{aligned} \tag{7.37}$$

Next, we discretize the torus by a finite number of momentum points and collect the values of $A_{\boldsymbol{k}}$ at all momentum points in a vector $\vec{A}$. Therefore, we can write Eq. (7.36) as an eigenvalue equation with

$$\frac{\delta\Gamma}{\delta A(\boldsymbol{\varphi})} = \sum_{\boldsymbol{\varphi}'} M_{\boldsymbol{\varphi}\boldsymbol{\varphi}'} A(\boldsymbol{\varphi}') \quad \Rightarrow \quad \frac{\delta\Gamma}{\delta \vec{A}} = \underline{\underline{M}}\vec{A}, \tag{7.38}$$

$$\frac{\delta\chi}{\delta A(\boldsymbol{\varphi})} = 2\Omega(\boldsymbol{\varphi})\delta_{\boldsymbol{\varphi},\boldsymbol{\varphi}'} A(\boldsymbol{\varphi}') \quad \Rightarrow \quad \frac{\delta\chi}{\delta \vec{A}} = \underline{\underline{G}}\vec{A}, \tag{7.39}$$

$$\Longrightarrow \left(\underline{\underline{G}}^{-1} \cdot \underline{\underline{M}}\right) \vec{A} = \frac{\Gamma}{\chi}\vec{A}, \tag{7.40}$$

where $\underline{\underline{G}}$ is a diagonal matrix only containing the Jacobi determinant of our parametrization. Thus, we can calculate the decay rates as the eigenvalues of a matrix and the eigenvectors will give us the corresponding modes. The resulting spectrum of eigenvalues for a discretization with 800 momentum points can be seen in Fig. 7.7. There is one vanishing eigenvalue which just corresponds to the trivial configuration $A_{\boldsymbol{k}} = 0$ for all values of $\boldsymbol{k}$. The smallest finite decay rates are only reduced by about a factor of 2 compared to the largest eigenvalues. Therefore, we can conclude that our low-energy model for $ZrTe_5$ does not posses any slowly decaying modes that can help mediate currents via some kind of pseudo-spin Hall effects.

In conclusion, the origin and width dependence of the nonlocal transport in $ZrTe_5$ remain a puzzling issue because the surface state mechanism as well as the results for the spin Hall effect contradict some parts of the experiments. The absence of a slow mode that can couple to the charge degree of freedom means that the current model for $ZrTe_5$ can not explain the nonlocal response. As there is also an interesting magnetic field behavior this research direction will remain important to fully understand the transport phenomena of nodal line semimetals.

8 Summary

In this thesis the transport properties of $ZrTe_5$ were studied with a focus on the nonlinear responses. We have seen that close to the topological phase transition this material is a nodal line semimetal which hosts many interesting transport phenomena. For small carrier density the Fermi surface is an elongated torus which has been confirmed by quantum oscillation measurements. The spin texture on the Fermi surface gives rise to a magnetochiral anisotropy due to the imbalance of spins parallel and anti-parallel to the magnetic field. This results in a nonreciprocal response where the resistance of the material changes if the current direction is reversed. We have seen that large-scale electron density modulations can enhance the nonlinear response of the homogeneous system. This is enabled by the anisotropic velocities of $ZrTe_5$. Additionally, one can also achieve very large Hall angles depending on the transport geometry because of these anisotropies.
Next, we turned to the enhancement of nonohmic transport where the Landau quantization of electrons played a prominent role. We derived that the lowest Landau level of a nodal line semimetal consists largely of a flat band which can host a plethora of states. Using the Boltzmann equation we have shown that tuning the system to the quantum limit leads to the amplification of nonlinear transport. Because of the discrepancy between experiment and theoretical prediction for the nonohmic coefficients without a magnetic field we used a nonlinear resistor network to explore the impact of charge density inhomogeneities. We have shown that a reasonable amount of disorder can lead to a sizable increase of the clean result. The behavior of the nonohmic coefficient can also be used to distinguish between a Dirac and a nodal line system.
The existence of an anti-symmetric Hall response in the parallel-field configuration implies a significant symmetry breaking. Including the necessary terms in our model we have shown that the nodal line plane will be tilted in momentum space. A small rotation of the Fermi surface enables a sizable unconventional Hall effect by just considering ordinary Lorentz forces. Therefore, there can be a lot of possible origins of Hall responses in topological materials which requires a careful symmetry analysis.
Finally, we studied a model of charge currents coupling to other degrees of freedom to find an explanation for nonlocal voltages with large decay length scales. As spin is not a conserved quantity and we are dealing with a highly spin-orbit coupled material the usual spin Hall effect was ruled out as a possible mechanism. Using a variational method we determined that our low-energy model does not possess any slow modes which can drive nonlocal currents. A possible origin from surface states has also been ruled out due to the width dependence of the decay length.

Outlook:

An inhomogeneous electron density distribution seems to be responsible for the gigantic nonlinear effects in $ZrTe_5$. Therefore, a theory of screening and puddle formation would provide further insight into this mechanism. Including the effects of local p-n junctions would enable the computation of a quantitative estimate for the nonlinear effects in inhomogeneous materials.
As the flat band hosts a huge number of states, correlation effects become increasingly important. It would be interesting to consider the interplay of topology and interactions in nodal line semimetals. At small magnetic fields the negative magnetoresistance is still not fully understood. Including vertex corrections as well as the anomalous Hall term in the Kubo formula could be necessary steps in calculating the full resistivity tensor.
The most puzzling issue would be the existence of the slowly decaying nonlocal transport. The absence of any slow mode rules out an origin from (pseudo-)spin Hall effects. So far there seems to be no realistic mechanism describing the nonlocal response in the presence of a magnetic field although thermoelectric effects could provide an explanation at zero field.

In conclusion, $ZrTe_5$ will continue to be a promising platform to study exotic transport phenomena of topological quantum materials.

Bibliography

[1] Felix Bloch. Über die Quantenmechanik der Elektronen in Kristallgittern. *Zeitschrift für Physik*, 52(7):555–600, Jul 1929.

[2] K. S. Novoselov, A. K. Geim, S. V. Morozov, D. Jiang, M. I. Katsnelson, I. V. Grigorieva, S. V. Dubonos, and A. A. Firsov. Two-dimensional gas of massless Dirac fermions in graphene. *Nature*, 438(7065):197–200, Nov 2005.

[3] X. Huang, L. Zhao, Y. Long, P. Wang, D. Chen, Z. Yang, H. Liang, M. Xue, H. Weng, Z. Fang, X. Dai, and G. Chen. Observation of the Chiral-Anomaly-Induced Negative Magnetoresistance in 3D Weyl Semimetal TaAs. *Phys. Rev. X*, 5:031023, Aug 2015.

[4] A. A. Burkov, M. D. Hook, and Leon Balents. Topological nodal semimetals. *Phys. Rev. B*, 84:235126, Dec 2011.

[5] P. A. M. Dirac. The quantum theory of the electron. *Proc. Roy. Soc. Lond. A*, 117:610–624, 1928.

[6] P. A. M. Dirac. A Theory of Electrons and Protons. *Proc. Roy. Soc. Lond. A*, 126(801):360–365, 1930.

[7] S. Das Sarma, Sh. Adam, E. H. Hwang, and E. Rossi. Electronic transport in two-dimensional graphene. *Rev. Mod. Phys.*, 83:407–470, May 2011.

[8] J. Zhao, H. Liu, Z. Yu, R. Quhe, S. Zhou, Y. Wang, C. C. Liu, H. Zhong, N. Han, J. Lu, Y. Yao, and K. Wu. Rise of silicene: A competitive 2D material. *Progress in Materials Science*, 83:24–151, 2016.

[9] A. Acun, L. Zhang, P. Bampoulis, M. Farmanbar, A. van Houselt, A. N. Rudenko, M. Lingenfelder, G. Brocks, B. Poelsema, M. I. Katsnelson, and H. J. W. Zandvliet. Germanene: the germanium analogue of graphene. *Journal of Physics: Condensed Matter*, 27(44):443002, Oct 2015.

[10] N. P. Armitage, E. J. Mele, and A. Vishwanath. Weyl and Dirac semimetals in three-dimensional solids. *Rev. Mod. Phys.*, 90:015001, Jan 2018.

[11] J. von Neumann and E. P. Wigner. *Über merkwürdige diskrete Eigenwerte*, page 291–293. Springer Berlin Heidelberg, Berlin, Heidelberg, 1993.

[12] Conyers Herring. Accidental Degeneracy in the Energy bands of Crystals. *Phys. Rev.*, 52:365–373, Aug 1937.

[13] A. Turner and A. Vishwanath. Beyond Band Insulators: Topology of Semimetals and Interacting Phases. *Contemporary Concepts of Condensed Matter Science*, 6:293–324, Dec 2013.

[14] H.B. Nielsen and M. Ninomiya. Absence of neutrinos on a lattice: (i). Proof by homotopy theory. *Nuclear Physics B*, 185(1):20–40, 1981.

[15] H.B. Nielsen and M. Ninomiya. Absence of neutrinos on a lattice: (ii). Intuitive topological proof. *Nuclear Physics B*, 193(1):173–194, 1981.

[16] S.-M. Huang, S.-Y. Xu, I. Belopolski, C.-C. Lee, G. Chang, B. Wang, N. Alidoust, G. Bian, M. Neupane, C. Zhang, S. Jia, A. Bansil, H. Lin, and M. Z. Hasan. A Weyl Fermion semimetal with surface Fermi arcs in the transition metal monopnictide TaAs class. *Nature Communications*, 6:7373, 2015.

[17] S.-Y. Xu, I. Belopolski, N. Alidoust, M. Neupane, G. Bian, C. Zhang, R. Sankar, G. Chang, Z. Yuan, C.-C. Lee, S.-M. Huang, H. Zheng, J. Ma, D. S. Sanchez, B. Wang, F. Bansil, A.and Chou, P. P. Shibayev, H. Lin, S. Jia, and M. Z. Hasan. Discovery of a Weyl fermion semimetal and topological Fermi arcs. *Science*, 349(6248):613–617, 2015.

[18] A. P. Sakhya, C.-Y. Huang, G. Dhakal, X.-J. Gao, S. Regmi, B. Wang, W. Wen, R.-H. He, X. Yao, R. Smith, M. Sprague, S. Gao, B. Singh, H. Lin, S.-Y. Xu, F. Tafti, A. Bansil, and M. Neupane. Observation of Fermi arcs and Weyl nodes in a noncentrosymmetric magnetic Weyl semimetal. *Phys. Rev. Mater.*, 7:L051202, May 2023.

[19] T.O. Wehling, A.M. Black-Schaffer, and A.V. Balatsky. Dirac materials. *Advances in Physics*, 63(1):1–76, 2014.

[20] Z. Wang, H. Weng, Q. Wu, X. Dai, and Z. Fang. Three-dimensional Dirac semimetal and quantum transport in Cd_3As_2. *Phys. Rev. B*, 88:125427, Sep 2013.

[21] Z. K. Liu, B. Zhou, Y. Zhang, Z. J. Wang, H. M. Weng, D. Prabhakaran, S.-K. Mo, Z. X. Shen, Z. Fang, X. Dai, Z. Hussain, and Y. L. Chen. Discovery of a Three-Dimensional Topological Dirac Semimetal, Na_3Bi. *Science*, 343(6173):864–867, 2014.

[22] Y. L. Chen, J.-H. Chu, J. G. Analytis, Z. K. Liu, K. Igarashi, H.-H. Kuo, X. L. Qi, S. K. Mo, R. G. Moore, D. H. Lu, M. Hashimoto, T. Sasagawa, S. C. Zhang, I. R. Fisher, Z. Hussain, and Z. X. Shen. Massive Dirac Fermion on the Surface of a Magnetically Doped Topological Insulator. *Science*, 329(5992):659–662, 2010.

[23] S. Kim, S. Yoshizawa, Y. Ishida, K. Eto, K. Segawa, Y. Ando, S. Shin, and F. Komori. Robust protection from Backscattering in the Topological Insulator $Bi_{1.5}Sb_{0.5}Te_{1.7}Se_{1.3}$. *Phys. Rev. Lett.*, 112:136802, Apr 2014.

[24] P. Drude. Zur Elektronentheorie der Metalle. *Annalen der Physik*, 306(3):566–613, 1900.

[25] P. Drude. Zur Elektronentheorie der Metalle; II. Teil. Galvanomagnetische und thermomagnetische Effecte. *Annalen der Physik*, 308(11):369–402, 1900.

[26] P. W. Anderson. Absence of Diffusion in Certain Random Lattices. *Phys. Rev.*, 109:1492–1505, Mar 1958.

[27] N. Borgwardt, J. Lux, I. Vergara, Zhiwei Wang, A. A. Taskin, Kouji Segawa, P. H. M. van Loosdrecht, Yoichi Ando, A. Rosch, and M. Grüninger. Self-organized charge puddles in a three-dimensional topological material. *Phys. Rev. B*, 93:245149, Jun 2016.

[28] O. Breunig, Z. Wang, A. A. Taskin, J. Lux, A. Rosch, and Y. Ando. Gigantic negative magnetoresistance in the bulk of a disordered topological insulator. *Nature Communications*, 8(1):15545, May 2017.

[29] D. Tong. Lectures on the Quantum Hall Effect. *arXiv*, 1606.06687, 2016.

[30] P. Coleman. *Introduction to Many-Body Physics*. Cambridge University Press, 2015.

[31] Y. Ando. Topological Insulator Materials. *Journal of the Physical Society of Japan*, 82(10):102001, 2013.

[32] W.J. De Haas and P.M. Van Alfphen. The Dependence of the Susceptibility of Diamagnetic Metals Upon the Field. *Proceedings of the Amsterdam Academy of Sciences*, 33(1106), 1930.

[33] D. Shoenberg. *Magnetic Oscillations in Metals*. Cambridge Monographs on Physics. Cambridge University Press, 1984.

[34] Y. Wang, H. F. Legg, T. Bömerich, J. Park, S. Biesenkamp, A. A. Taskin, M. Braden, A. Rosch, and Y. Ando. Gigantic Magnetochiral Anisotropy in the Topological Semimetal $ZrTe_5$. *Phys. Rev. Lett.*, 128:176602, Apr 2022.

[35] H. Weng, X. Dai, and Z. Fang. Transition-Metal Pentatelluride $ZrTe_5$ and $HfTe_5$: A Paradigm for Large-Gap Quantum Spin Hall Insulators. *Phys. Rev. X*, 4:011002, Jan 2014.

[36] R. Y. Chen, Z. G. Chen, X.-Y. Song, J. A. Schneeloch, G. D. Gu, F. Wang, and N. L. Wang. Magnetoinfrared Spectroscopy of Landau Levels and Zeeman Splitting of Three-dimensional Massless Dirac Fermions in $ZrTe_5$. *Phys. Rev. Lett.*, 115:176404, Oct 2015.

[37] Q. Li, D.E. Kharzeev, C. Zhang, Y. Huang, I. Pletikosić, A. V. Fedorov, R. D. Zhong, J. A. Schneeloch, G. D. Gu, and T. Valla. Chiral magnetic effect in $ZrTe_5$. *Nature Physics*, 12(6):550–554, February 2016.

[38] Y. Zhang *et. al.*. Electronic evidence of temperature-induced Lifshitz transition and topological nature in $ZrTe_5$. *Nature Communications*, 8(1):15512, May 2017.

[39] T. Liang, J. Lin, Q. Gibson, S. Kushwaha, M. Liu, W. Wang, H. Xiong, J. A. Sobota, M. Hashimoto, P. S. Kirchmann, Z.-X. Shen, R. J. Cava, and N. P. Ong. Anomalous Hall effect in $ZrTe_5$. *Nature Physics*, 14(5):451–455, May 2018.

[40] H. Wang, H. Liu, Y. Li, Y. Liu, J. Wang, J. Liu, J.-Y. Dai, Y. Wang, L. Li, J.Yan, D. Mandrus, X. C. Xie, and J. Wang. Discovery of log-periodic oscillations in ultraquantum topological materials. *Science Advances*, 4(11):eaau5096, 2018.

[41] P. Shahi, D. J. Singh, J. P. Sun, L. X. Zhao, G. F. Chen, Y. Y. Lv, J. Li, J.-Q. Yan, D. G. Mandrus, and J.-G. Cheng. Bipolar Conduction as the Possible Origin of the Electronic Transition in Pentatellurides: Metallic vs Semiconducting Behavior. *Phys. Rev. X*, 8:021055, May 2018.

[42] F. Tang, Y. Ren, P. Wang, R. Zhong, J. Schneeloch, S. A. Yang, K. Yang, P. A. Lee, G. Gu, Z. Qiao, and L. Zhang. Three-dimensional quantum Hall effect and metal–insulator transition in $ZrTe_5$. *Nature*, 569(7757):537–541, May 2019.

[43] Z. Sun, Z. Cao, J. Cui, C. Zhu, D. Ma, H. Wang, W. Zhuo, Z. Cheng, Z. Wang, X. Wan, and X. Chen. Large Zeeman splitting induced anomalous Hall effect in $ZrTe_5$. *npj Quantum Materials*, 5(1):36, Jun 2020.

[44] P. Zhang, R. Noguchi, K. Kuroda, C. Lin, K. Kawaguchi, K. Yaji, A. Harasawa, M. Lippmaa, S. Nie, H. Weng, V. Kandyba, A. Giampietri, A. Barinov, Q. Li, G. D. Gu, S. Shin, and T. Kondo. Observation and control of the weak topological insulator state in $ZrTe_5$. *Nature Communications*, 12(1):406, Jan 2021.

[45] Y. Jiang, J. Wang, T. Zhao, Z. L. Dun, Q. Huang, X. S. Wu, M. Mourigal, H. D. Zhou, W. Pan, M. Ozerov, D. Smirnov, and Z. Jiang. Unraveling the Topological Phase of $ZrTe_5$ via Magnetoinfrared Spectroscopy. *Phys. Rev. Lett.*, 125:046403, Jul 2020.

[46] B. Xu, L. X. Zhao, P. Marsik, E. Sheveleva, F. Lyzwa, Y. M. Dai, G. F. Chen, X. G. Qiu, and C. Bernhard. Temperature-Driven Topological Phase Transition and Intermediate Dirac Semimetal Phase in $ZrTe_5$. *Phys. Rev. Lett.*, 121:187401, Oct 2018.

[47] E. Wang, H. Zeng, W. Duan, and H. Huang. Spontaneous Inversion Symmetry Breaking and Emergence of Berry Curvature and Orbital Magnetization in Topological $ZrTe_5$ Films. *Phys. Rev. Lett.*, 132:266802, Jun 2024.

[48] Y. Tokura and N. Nagaosa. Nonreciprocal responses from non-centrosymmetric quantum materials. *Nature Communications*, 9(1):3740, Sep 2018.

[49] G. L. J. A. Rikken, J. Fölling, and P. Wyder. Electrical Magnetochiral Anisotropy. *Phys. Rev. Lett.*, 87:236602, Nov 2001.

[50] G. L. J. A. Rikken and P. Wyder. Magnetoelectric Anisotropy in Diffusive Transport. *Phys. Rev. Lett.*, 94:016601, Jan 2005.

[51] G. L. J. A. Rikken and N. Avarvari. Strong electrical magnetochiral anisotropy in tellurium. *Phys. Rev. B*, 99:245153, Jun 2019.

[52] Y. Wang, T. Bömerich, A. A. Taskin, A. Rosch, and Y. Ando. Parallel-Field Hall effect in $ZrTe_5$. *arXiv*, 2408.11113, 2024.

[53] Y. H. Kwan, P. Reiss, Y. Han, M. Bristow, D. Prabhakaran, D. Graf, A. McCollam, S. A. Parameswaran, and A. I. Coldea. Quantum oscillations probe the Fermi surface topology of the nodal-line semimetal CaAgAs. *Phys. Rev. Res.*, 2:012055, Mar 2020.

[54] L. Fu. Hexagonal Warping Effects in the Surface States of the Topological Insulator Bi_2Te_3. *Phys. Rev. Lett.*, 103:266801, Dec 2009.

[55] Z. Alpichshev, J.G. Analytis, J.-H. Chu, I.R. Fisher, Y.L. Chen, Z.X. Shen, A. Fang, and A. Kapitulnik. STM Imaging of Electronic Waves on the Surface of Bi_2Te_3: Topologically Protected Surface States and Hexagonal Warping Effects. *Phys. Rev. Lett.*, 104:016401, Jan 2010.

[56] J. Wang, J. Niu, B. Yan, X. Li, R. Bi, Y. Yao, D. Yu, and X. Wu. Vanishing quantum oscillations in Dirac semimetal $ZrTe_5$. *Proc Natl Acad Sci USA*, 115(37):9145–9150, August 2018.

[57] T. Ideue, K. Hamamoto, S. Koshikawa, M. Ezawa, S. Shimizu, Y. Kaneko, Y. Tokura, N. Nagaosa, and Y. Iwasa. Bulk rectification effect in a polar semiconductor. *Nature Physics*, 13(6):578–583, Jun 2017.

[58] C. Wang, A. Hickey, X. Ying, and A.A. Burkov. Emergent anomalies and generalized Luttinger theorems in metals and semimetals. *Phys. Rev. B*, 104:235113, Dec 2021.

[59] Y. Wang, T. Bömerich, J. Park, H. F. Legg, A. A. Taskin, A. Rosch, and Y. Ando. Nonlinear Transport due to Magnetic-Field-Induced Flat Bands in the Nodal-Line Semimetal $ZrTe_5$. *Phys. Rev. Lett.*, 131:146602, Oct 2023.

[60] A. A. Abrikosov. Quantum linear magnetoresistance. *Europhysics Letters*, 49(6):789, Mar 2000.

[61] J.-W. Rhim and Y. B. Kim. Landau level quantization and almost flat modes in three-dimensional semimetals with nodal ring spectra. *Phys. Rev. B*, 92:045126, Jul 2015.

[62] J. Klier, I. V. Gornyi, and A. D. Mirlin. Transversal magnetoresistance and Shubnikov–de Haas oscillations in Weyl semimetals. *Phys. Rev. B*, 96:214209, Dec 2017.

[63] A. A. Abrikosov. Quantum magnetoresistance. *Phys. Rev. B*, 58:2788–2794, Aug 1998.

[64] A. A. Taskin, H. F. Legg, F. Yang, S. Sasaki, Y. Kanai, K. Matsumoto, A. Rosch, and Y. Ando. Planar Hall effect from the surface of topological insulators. *Nature Communications*, 8(1):1340, Nov 2017.

[65] A. A. Burkov. Giant planar Hall effect in topological metals. *Phys. Rev. B*, 96:041110, Jul 2017.

[66] S. Nandy, Gargee Sharma, A. Taraphder, and Sumanta Tewari. Chiral Anomaly as the Origin of the Planar Hall effect in Weyl Semimetals. *Phys. Rev. Lett.*, 119:176804, Oct 2017.

[67] J. Sinova, S. O. Valenzuela, J. Wunderlich, C. H. Back, and T. Jungwirth. Spin Hall effects. *Rev. Mod. Phys.*, 87:1213–1260, Oct 2015.

[68] M. Dyakonov. *Spin Physics in Semiconductors*, volume 1. 07 2008.

[69] T. Kimura, Y. Otani, T. Sato, S. Takahashi, and S. Maekawa. Room-Temperature Reversible Spin Hall Effect. *Phys. Rev. Lett.*, 98:156601, Apr 2007.

[70] P. Jung and A. Rosch. Lower bounds for the conductivities of correlated quantum systems. *Phys. Rev. B*, 75:245104, Jun 2007.